Optimization of ice-class ship propellers

Teunis J. Huisman
30 October 2015

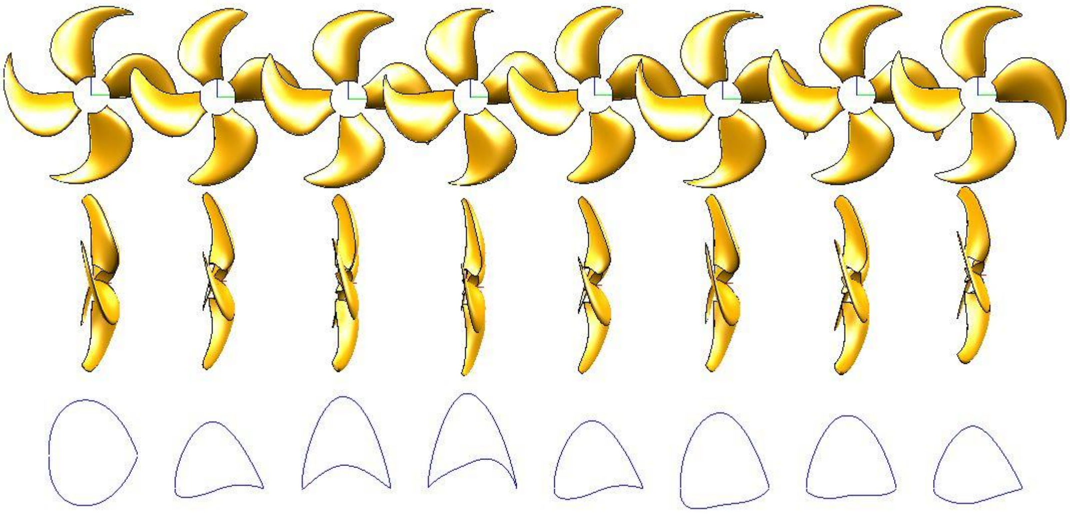

A Delft University of Technology Master's Thesis Definition Study performed at MARIN

Marine Technology – Science – Resistance and Propulsion

Optimization of ice-class ship propellers

Author	:	Teunis J. Huisman
Student number	:	4080777
Contact Details	:	tj.huisman@hotmail.com
		nl.linkedin.com/in/huismanjohn/
		0031 642 823 814

Project Duration	:	January – November 2015
Date	:	30 October 2015

Committee Members	:	Prof. Dr. Ir. T.J.C. van Terwisga	(MARIN/TUDelft)
		Ing. G. Hagesteijn	(MARIN)
		Dr. Ir. E.J. Foeth	(MARIN)
		Ir. E.A.J. Vroegrijk	(Lloyd's Register)
		Dr. Ir. H.J. de Koning Gans	(TUDelft)
		Prof. Dr. Ir. B.J. Boersma	(TUDelft)
		Dr. Ir. A. Vrijdag	(TUDelft)

A Delft University of Technology Master's Thesis performed at MARIN
Marine Technology – Science – Resistance and Propulsion

A report submitted to the faculty of Marine Engineering at Delft University of Technology in partial fulfillment of the requirements of a Master's of Science thesis at the chair of Propulsion and Resistance of Ships.

ABSTRACT

The main objective of this Master's thesis is to develop an optimization routine to improve ice-class propeller design methodology using the design space within the ice-class rules.

Ice impacts on a ship propeller give additional design demands to ensure reliability and safety. Consequently, ice class propellers feature thicker blades, therewith compromising fuel efficiency. However, ships trading the Baltic states and Scandinavia only sail two to five percent of their time in ice-infested waters. Propulsive efficiency should hence be optimized for ice-free conditions only, while still having sufficient ice performance and strength. The Finnish Swedish Ice Class Rules prescribe loads on the propeller blade as five load cases of uniform pressure that should be applied on the propeller blade.

The Non-Dominated Sorting Genetic Algorithm II (NSGAII) is coupled to MARIN's in-house propeller geometry generator, hydrodynamic boundary element analysis method PROCAL and a finite element analysis to evaluate the propeller blade strength. Both the radial and chordwise propeller distributions are parameterized by means of Bézier curves into optimization design variables. With these expansions, the computational framework is capable to automatically satisfy the ice-class stress constraints while converging to the best possible objective values. Each propeller within the optimization is iterated on mean pitch towards a design thrust.

The four optimization objectives that are considered in this Master's thesis are propeller efficiency, thrust variation throughout the ship's wake field, propeller mass and ice-induced loading. Efficiency is considered as main objective while thrust variation is intended to provide interaction with the wake field. Besides the practical importance of the mass objective, it also guides the optimization towards high efficiency and maximum allowable material stresses. Based on a steady simulation of ice milling by means of an idealized ice-load pressure distribution, the ice-induced loading can be estimated as quantification of ice-performance.

Best practice guidelines on the usage of PROCAL within the optimization are developed based on grid refinement and numerical uncertainty studies. Four different implementations of the finite element method are compared to the solution from a dense tetrahedral solid element mesh. Linear shell elements appear to perform best, both in terms of computational time and accuracy.

A case study shows that ice-induced loading can be reduced as function of particularly the pitch distribution and blade profile geometry. It is also observed that the optimization searches for the weaknesses within the computational methods. For instance, it appears that the current ice-class rules allow highly skewed propellers, despite damage cases in practise. The optimization results are encouraging for future work concerning the optimization of blade profiles, although further work is required. It appears that the thrust variation objective steers towards flat chordwise pressure distributions. Cavitation computations are not yet included in the optimization, nonetheless, the optimized propellers show only little cavitation in the tip region. In conclusion, the optimization seems to provide a well-balanced starting point towards the design of high efficiency ice-class propellers.

SAMENVATTING

Het hoofddoel van deze afstudeerscriptie is het ontwikkelen van een optimalisatie routine voor ijsklasse schroeven om hun ontwerpmethodiek te verbeteren aan de hand van de ontwerpruimte binnen de huidige ijsklasse regels.

De botsingen tussen ijs en een scheepsschroef geven aanleiding to extra ontwerpeisen om betrouwbaarheid en veiligheid te waarborgen. Als gevolg van de ijsbelasting hebben ijsklasse schroeven dikkere schroefbladen waarmee het rendement aangetast wordt. Echter, handelsschepen naar de Baltische staten en Scandinavië varen maar twee tot vijf procent van hun tijd door ijs. Het rendement van de voortstuwingsinstallatie moet daarom alleen geoptimaliseerd worden voor ijsvrij water. Tegelijkertijd moeten de schroeven sterk genoeg zijn en voldoende prestaties leveren in ijs. De Fins-Zweedse ijsklasse regels schrijven de belastingen voor in de vorm van vijf belastingssituaties van uniforme druk die aangebracht moeten worden op het schroefblad.

Het Niet-Gedomineerde Sortering Genetische optimalisatie Algoritme (NSGAII) is gekoppeld aan een schroefblad geometrie generator van MARIN, de hydrodynamische grenselementen analyse methode PROCAL en een eindige elementen analyse methode om de sterkte van het blad te bepalen. Zowel de radiale- als koorde verdelingen zijn geparametriseerd met behulp van Bézier krommes in ontwerpvariabelen voor de optimalisatie. Met deze aanvullingen is het berekeningsprogramma in staat de randvoorwaarden van de ijsklasse op materiaal spanningen automatisch te voldoen terwijl de optimalisatie convergeert naar de best mogelijke doelen. Elke propeller in de optimalisatie is onderworpen aan een iteratieve aanpassing van de gemiddelde spoed zodat de stuwkracht voldoet aan het ontwerppunt.

De vier optimalisatie doelen in deze afstudeerscriptie zijn schroefrendement, stuwkracht variatie in het scheepszog, schroefmassa en de belasting als gevolg van ijs. Rendement is het hoofddoel terwijl de stuwkracht variatie moet zorgen voor een wisselwerking met het scheepszog. Behalve het praktische nut van schroefmassa, leidt dit doel de optimalisatie ook richting hoog rendement and maximaal toelaatbare materiaal spanningen. Gebaseerd op een statische simulatie van ijsvermaling door middel van een versimpelde ijsbelastingdruk kan een schatting gemaakt worden van de schroefprestatie in ijs.

Richtlijnen voor het gebruik van PROCAL in een optimalisatie zijn ontwikkeld door middel van een roosterverfijningsstudie en numerieke onzekerheidsstudies. Vier verschillende implementaties van de eindige elementen methode zijn vergeleken met de oplossing op een fijn rooster van viervlakken. Lineaire schaal elementen blijken het beste te presteren op het gebied van berekeningstijd en nauwkeurigheid.

Een casus laat zien dat de belasting als gevolg van ijs beperkt kan worden als functie van de geometrie van de schroef. Vooral het bladprofiel en de spoed hebben invloed. Het kan ook opgemerkt worden dat de optimalisatie naar de zwaktes in de berekeningsmethoden zoekt. Het lijkt er bijvoorbeeld op dat de huidige ijsklasse regels hoge *skew* toelaten ondanks de schadegevallen in de praktijk. De resultaten van de optimalisatie moedigen toekomstig onderzoek aan met betrekking tot de blad profielen. Het lijkt erop dat het stuwkracht variatie doel de optimalisatie naar vlakke drukverdelingen over de koorde toe stuurt. Cavitatie berekeningen zijn nog niet aanwezig in de optimalisatie, desondanks laten de geoptimaliseerde propellers alleen op de schroeftip een beetje cavitatie zien. Als conclusie kan gesteld worden dat de optimalisatie een goed gebalanceerd startpunt lijkt te geven voor het ontwerp van hoog rendement ijsklasse schroeven.

PREFACE

I already had quite some background in ice engineering due to the ‘Arctic’ minor and my bachelor project. The OMAE2014 in San Francisco was the starting point of the problem formulation. I liked to take the problem of propeller-ice interaction again, and focus on it which much more dedication and time. For that reason a good practical problem was needed. Eventually, this resulted in the problem of cargo ships instead of the heavy ice breakers.

During a discussion with my professor, Tom van Terwisga, it was agreed that my project could be performed at MARIN. I would like to thank Tom for his confidence, critical remarks and support.

I wish to thank my daily supervisor, Gerco Hagesteijn, for his support and discussions during this first stage of the graduation process. Evert-Jan Foeth, my daily supervisor during the computational stage of the project, guided me through the numerous MATLAB scripts and gave me insight in the beautiful world of propeller design, thank you Evert-Jan! I especially liked the talks which often elaborated into numerous propeller design related topics. In this light also Arjan Lampe provided me with his practical view and experience on strength analyses. Thank you for all the discussions, Arjan.

A lot of people supported me during this project. My thoughts go to my committee members and the propeller knowledge group at MARIN for giving advice and listening to early versions of the presentation. I hope all MARIN employees will forgive me as I almost permanently claimed the only ANSYS license.

I want to thank my roommates for allowing me in the office and colleague student Reinier Bos for the daily discussions and his review of my report.

Finally, I'm very grateful to my fiancée Jantine for her patience and understanding, especially when she heard that graduation had to be delayed for almost a month. Probably, the preparations for our wedding and the refurbishing of our future home did no good in this respect. Above all, I thank the almighty God for giving me the power, critical mind and talents to study this topic.

John

CONTENTS

NOMENCLATURE

BEM	Boundary Element Method
BPG	Best Practise Guidelines
CPP	Controllable Pitch Propeller
CRS	Cooperative Research Ships consortium
DNV	Det Norske Veritas
DWT	DeadWeight Tonnage
FEM	Finite Element Method
FPP	Fixed Pitch Propeller
FSICR	Finnish-Swedish Ice Class Rules
GA	Genetic Algorithm
ITTC	International Towing Tank Conference
LC	Load Case
LE	Leading Edge
MARIN	MAritime Research Institute Netherlands
MCR	Maximum Continuous Rating
NACA	National Advisory Committee for Aeronautics
NNF	Negative Null Form
NURBS	Non-Uniform Rational Basis Spline
NSGAII	Non-dominated Sorting Genetic Algorithm version II.
SBX	Simulated Binary Crossover
TE	Trailing Edge
TraFi	Finnish Transport Safety Agency
2D	Two-Dimensional
3D	Three-Dimensional

A	Swept area by the propeller	m^2
A_T	Amplitude of thrust	N
$\boldsymbol{A}$	Location of $25°$ angle between α and blade profile	m
B	Ship breadth	m
BAR	Expanded blade area ratio	-
$\boldsymbol{B}$	Location of loss of ice contact	m
$\boldsymbol{B}^*$	Length of blade profile from $\boldsymbol{O}$ to $\boldsymbol{B}$	m
c	Dimensionless chord length	-
c_{cf}	Safety factor in a numerical uncertainty study	
c_{tip}	Bézier control point at tip	
c_{hub}	Bézier control point at hub	
c_{max}	Bézier control point at maximum position	
$\boldsymbol{c}$	Vector of optimization objectives	
C	Boundary contour	m
C_p	Pressure coefficient	-
C_T	Thrust loading coefficient	-
d	Propeller hub diameter	m
D	Propeller diameter	m
$\boldsymbol{D}$	Location of $3°$ angle between α and blade profile	m
$\boldsymbol{e}$	Strain tensor	-
E	Young's elastic modulus	
$\boldsymbol{E}$	Elastic moduli tensor	
$\boldsymbol{E}$	Location of $0°$ angle between α and blade profile	m
$\boldsymbol{f}$	Force vector in FEM	N
f	Optimization objective	
F_b	Backward ice milling force	kN
F_f	Forward hydrodynamic ice induced force	kN
$\boldsymbol{F}^b$	Body force vector	N
$\boldsymbol{F}^{ice}$	Ice-class load force vector	N
$\boldsymbol{F}^s$	Surface force vector	N
g	Gravitational constant	m/s^2
$\boldsymbol{g}$	Optimization inequality constraints	
$\boldsymbol{g}$	Gravity vector	N/m^3
G_i	Optimization generation	

h_{hub}	Bézier handle point at hub	
h_i	Grid spacing	m
h_{LE}	Bézier handle point at leading edge	
h_s	Shaft immersion at design draft	m
h_{tip}	Bézier handle point at tip	
h_{TE}	Bézier handle point at trailing edge	
$\boldsymbol{h}$	Optimization equality constraints	
H_i	Ice thickness	m
J	Advance coefficient	-
$\boldsymbol{K}$	Stiffness matrix in FEM	
K_T	Thrust coefficient	-
K_Q	Torque coefficient	-
L	Ship length	m
m	Source strength	
m_i	Points masses of Bézier curve	
M	Propeller mass	kg
n	Propeller rotational speed	rev/s
n	Order of Bézier curve	
n_i	Number of grid cells in one direction	
N	Interpolation functions in FEM	
N_i	Total number of grid cells	
$\boldsymbol{O}$	Optimization algorithm structure	
$\boldsymbol{O}$	Position of leading edge	m
p	Pressure	Pa
p	Order of convergence	
p_a	Atmospheric pressure	Pa
p_L	Ice confinement zone pressure	MPa
p_{LE}	Leading edge ice induced pressure	MPa
p_{MA}	Maximum ice induced pressure	MPa
p_{WA}	Time averaged maximum ice induced pressure	MPa
p_{ref}	Characteristic pressure at certain location	Pa
p_v	Vapour pressure of sea water	Pa
P	Singular point in BEM	
P	Pitch angle at certain propeller radius	°
$\boldsymbol{P}$	Center of mass of Bézier curve	m
$\boldsymbol{P}$	Optimization propeller structure	
$\boldsymbol{P_n}$	Position of Bézier curve control points	m
P_D	Delivered power to propeller	W
P_t	Parent population	
P_T	Thrust power	W
Q	Torque	Nm
r	Radial coordinate	m
s	Displacement	m
S	Boundary surface	m^2
S_B	Propeller body surface	m^2
S_C	Cavitation surface	m^2
S_{hub}	Hub boundary	m^2
S_w	Propeller wake surface	m^2
S_∞	Far field boundary	m^2
t	Sweep parameter for Bézier curve	
t	Time	s
T	Thrust	N
$\boldsymbol{u}$	Velocity vector	m/s
u_i	Velocity in direction i	m/s
u_x	Axial velocity	m/s
u_r	Radial velocity	m/s
u_ϕ	Tangential velocity	m/s
U_0	Undisturbed velocity	m/s
U_{ref}	Characteristic velocity at certain location	m/s
U_{φ_i}	Numerical uncertainty for numerical solution φ_i	
U_{η^*}	Numerical prediction for uncertainty in η	

V	Material volume / domain	m^3
V_A	Advance velocity	m/s
V_s	Ship speed	m/s
V_Ω	Rotational speed at certain propeller radius	m/s
w	Ice cutting width	m
w	Wake fraction	-
x	x-coordinate	m
x_{soi}	x-coordinate in Soininen's ice model	m
$\boldsymbol{x}$	Position	m
$\boldsymbol{x}$	Optimization design variable vector	
$\underline{\boldsymbol{x}}$	Vector with lower bounds of design variables	
$\overline{\boldsymbol{x}}$	Vector with upper bounds of design variables	
X	Optimization design space	
y	y-coordinate	m
y_{soi}	y-coordinate in Soininen's ice model	m
Z	Number of propeller blades	
α	Angle of attack	°
α	Multiplication factor in numerical uncertainty analysis	
γ	Source strength in BEM	
γ	Advance angle at certain propeller radius	°
Γ	Circulation	m^2/s
δ_{RE}	Estimate of discretisation error	
δT	Dimensionless thrust variation	-
$\delta\boldsymbol{v}$	Virtual displacement vector	m
Δ	Laplacian	
ϵ	Imaginary radius of singular point	m
ϵ_ϕ	Discretisation error	
$\boldsymbol{\zeta}$	Vorticity vector	1/s
η	Efficiency	-
θ	Tangential coordinate	rad
λ	Doublet strength	
μ_B	Dipole strength on propeller body	
μ_W	Dipole strength on wake surface	
ν	Poisson's ratio	-
ρ	Density of water	kg/m^3
σ	Mass production	kg/s
σ	Cavitation number	-
σ_{ice}	Ice strength	Pa
σ_{ref}	Stress reference value	Pa
σ_u	Stress at ultimate tensile strength	Pa
$\sigma_{0.2}$	Stress at 0.2% plastic strain	Pa
$\boldsymbol{\sigma}$	Cauchy stress tensor	Pa
φ	Disturbance potential	-
φ_{exact}	Numerical value of the exact solution	
φ_f	Least squares fit value in grid refinement study	
φ_i	Numerical value of a certain solution	
φ_0	Estimate of exact solution	
ϕ	Velocity potential	-
ϕ_d	Velocity potential of a doublet	-
ϕ_P	Velocity potential at the pressure side	-
ϕ_r	Test function	-
ϕ_s	Velocity potential of a source	-
ϕ_S	Velocity potential at the suction side	-
ϕ_{TE}	Velocity potential at the trailing edge	-
ϕ_u	Velocity potential of uniform flow	-
∇	Gradient operator	

1 INTRODUCTION

The main purpose of this Master's thesis is to develop an analysis routine to improve ice-class propeller design methodology. This includes further study on the validity of the hypothesis from the literature research.

Prior to this report, a literature research and definition study were carried out by the author (Huisman, 2015). The research question was formulated as follows: *"How can propeller efficiency of ice-class cargo ships in operational conditions be improved by means of an automated propeller design optimization routine taking design constraints into account?"* It was hypothesized that an optimization procedure gives valuable insight in the trade-off between efficiency, ice strengthening, ice performance and cavitation nuisance.

Sailing through ice infested waters gives additional propeller design demands because impacting ice blocks exert significant loads on a propeller blade. Under these circumstances, reliability and safety should be ensured. The Finnish Swedish Ice Class Rules[1] (TraFi, 2010) prescribe maximum loads that the propeller blade should withstand. Typically, these loads are an order of magnitude higher than hydrodynamic loads. Consequently, ice-class propellers feature thicker blades and larger hubs than non-ice-class propellers, thereby compromising fuel efficiency.

Ships trading the Baltic states and Scandinavia, however, only sail 2 to 5 percent of their time in ice infested waters (Huisman, 2015). For these ships, propulsive efficiency should therefore be optimized for ice-free conditions only, whilst having sufficient ice performance and strength.

1.1 Background

The definition study by Huisman (2015) starts with an analysis of the practical problem. Ship propulsion in ice was reviewed and the background of the ice class rules was identified. The conventional iterative propeller design cycle was studied together with the impact of ice class requirements on propeller geometry and efficiency. The definition study closed with a research proposal which is taken in this Master's thesis.

An investigation of the background of the ice-class rules showed that the ice failure model of Soininen (1998) and the time simulation model of Koskinen et al. (1996) served as a basis. Regression analyses of parametric studies with the simulation model resulted in the current ice-class load formulations. A limited number of propellers was considered for which diameter, thickness, blade area ratio, rotational speed and apparent angle of attack were varied together with ice block properties. This simulation model depends on initial ice block sizes and properties, velocities and hull geometry besides propeller geometry. Since it was concluded in Huisman (2015) that a full milling condition gives the highest ice loads, a steady milling simulation could be coupled to the optimization framework to predict the ice induced loading.

Practically, the design space in the current ice-class rules is important. Five load cases have to be applied on the propeller blade for which its material should not yield. Although the ice-class rules have limited geometry dependency on the loads, the geometry dependency is abundantly present in the final material failure constraints. Propeller designers are confronted with the choice of the 'best' propeller for the vessel under development. Knowledge on the aforementioned trade-offs in propeller performance would guide the designer to the optimal propeller.

[1] In the remainder of this Master's thesis referred to as 'ice-class rules'

1.2 Thesis Outline

Based on the research question and the purpose of this Master's thesis the following sub-questions will be considered:

1. How can stress constraints from the ice-class rules be satisfied for the propeller material within an optimization?
2. How can the design space within the ice-class rules be utilized with respect to obtainable efficiency and hydrodynamic behavior?
3. What are best practice guidelines for ice-class propeller design?

Following the hypothesis that an optimization could provide answers to these questions, this Master's thesis addresses an automatic computational framework with the following three main components:

I. **Objectives $\boldsymbol{f}$ and Constraints $\boldsymbol{g}, \boldsymbol{h}$** define the core of the framework. Objectives should be optimized while constraints should be satisfied. Besides efficiency and stress, also thrust variation will be considered to guide the pressure distribution over the propeller. To avoid heavy propellers, a mass objective could be used to steer the algorithm towards maximum allowable stresses and high efficiency. Ice-induced loading as function of propeller geometry is studied as well with an simplified simulation with Soininen's (1998) model.

II. **Geometry Generation** is a key in any design problem. Propeller geometry should be fully parameterized, while the number of design parameters should be limited.

III. **Computational Analysis** is required to assess the fitness of a propeller based on the objectives and constraints. Hydrodynamic and structural analysis are required and will be addressed. In addition, ice milling loads should be estimated. These analysis tools are coupled to an optimization structure $\boldsymbol{O}$ in which all design parameters, objectives and constraint violations will be stored. Hence, an optimization algorithm can indirectly be coupled to the analysis tools to obtain generality of the computational framework.

1.3 Scope

Within this Master's thesis the scope is limited to fixed pitch propeller blades. Hence, in the following it will be assumed that the:

- Operational propeller design point is prescribed.
- Effective wake field of the ship is known and constant for axial and tangential velocities.
- Ice-class rules solely govern propeller strength.
- Propeller hub can be used for all propeller blade geometries.

Furthermore, only focusing on the subsystem of propeller blades, this Master's thesis does not address the matching of ship hull, main engine and propeller. Propeller-hull interaction, which should ideally be taken into account during propeller geometry optimization, is not considered in this Master's thesis and left for further research.

1.4 Optimization Objectives and Constraints

Objectives and constraints form the core in any optimization problem. A propeller should satisfy the constraints whilst having the best objectives. Referring to Table 1-1, four objectives are considered in this Master's thesis. Their further explanation is given in subsections 1.4.1 to 1.4.4.

Table 1-1: Objectives, constraints on the propeller results, constraints on the design parameters & constraints due to failures within geometry generation or analysis tools.

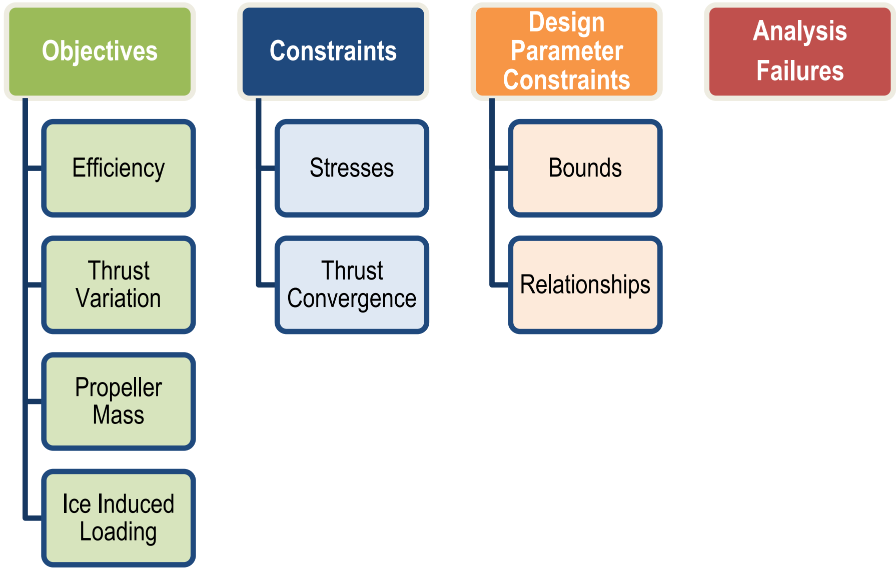

Constraints come in different forms as indicated by Table 1-1. The user-adjusted primary constraints on stresses and thrust convergence relate to propeller performance. These are considered in subsections 1.4.5 and 1.4.6 respectively. Design parameter constraints serve to generate new propeller geometries without fatal errors due to infeasible geometries and will be addressed in section 2.1 on propeller geometry. Avoiding fatal errors, analysis failures are dealt with as constraints as explained further in section 3.4.

1.4.1 Objective 1: Efficiency

Efficiency is the most important objective which should naturally be maximized for any propeller design. It relates the required engine power, or delivered power P_D, to delivered thrust power P_T to propel the ship. Efficiency gives an indication of the effectiveness of the delivered main engine power. Together with machinery efficiency and propulsor-hull interaction, propeller efficiency is directly related to the operational costs of a ship by means of fuel consumption.

A formal definition for propeller efficiency η can be written as:

$$\eta = \frac{P_T}{P_D} = \frac{TV_A}{2\pi Q n} = \frac{K_T}{K_Q}\frac{J}{2\pi} \tag{1}$$

where T propeller thrust in [N], Q propeller torque in [Nm] and n propeller rotational speed in [Hz]. Furthermore, in the last equality the following standard non-dimensional definitions are used:

$$K_T = \frac{T}{\rho n^2 D^4}, K_Q = \frac{Q}{\rho n^2 D^5} \quad \text{and} \quad J = \frac{V_A}{nD} \tag{2}$$

Thrust coefficient K_T, torque coefficient K_Q and advance coefficient J are made non-dimensional by a combination of density ρ [kg/m^3], rotational speed n [Hz] and diameter D [m]. It should be noted that the incoming velocity V_A in [m/s] is a circumferentially averaged quantity in behind hull conditions to present the average efficiency of the propeller in the wake field.

1.4.2 Objective 2: Thrust Variation

It is assumed that cavitation hindrance can be limited by minimizing the first harmonic of thrust variation in a non-cavitating calculation. This can be regarded as an estimator of pressure pulses. The pressure profile over the propeller blade will be smoothed out over a range of angles of attack, while the propeller will tend towards a high skew design.

In unsteady computations, the thrust on a single key blade varies through the wake field due to the change in angle of attack. A Fourier series can be used to describe the force as visualized in Figure 1-1.

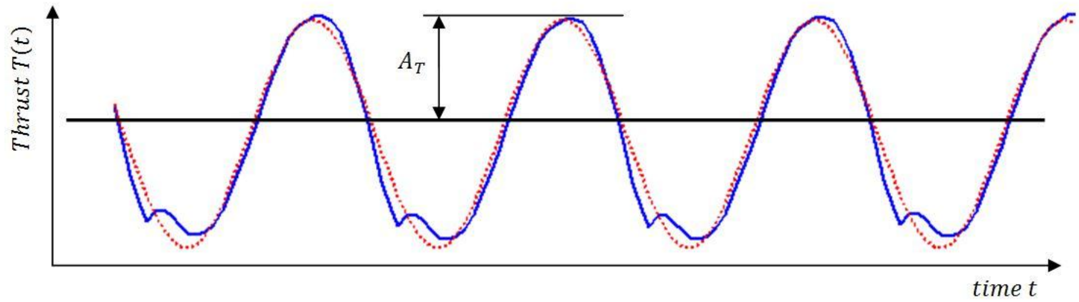

Figure 1-1: Thrust (solid blue line) and its first harmonic (dotted red line) as function of time. The frequency is determined by the number of blades and rotation rate. The black horizontal line indicates mean thrust, while the amplitude represents the first harmonic of thrust variation over time.

The first harmonic within this series is representative for the amplitude of the thrust variation. Thrust variation is presented in this Master's thesis as the ratio between the magnitude of the first harmonic the time dependent thrust A_T and the total average thrust of the propeller T:

$$\delta T = \frac{A_T}{T} \tag{3}$$

Note that all blades feature the same thrust variation[2] with a phase difference. Hence, the magnitude of thrust variation of the key blade only suffices. Within the optimization it should be minimized.

1.4.3 Objective 3: Propeller Mass

Especially for FPPs, mass is strongly correlated with investment costs. Additionally, propeller mass can be added as objective to help the algorithm converge to high efficiency propellers with low thrust variation while material stresses approach their limit.

Mass is indirectly linked with efficiency via the expanded blade area ratio and the chord and camber ratios with respect to thickness. For both mass and material stresses, the thickness of the profile is important. Most propeller blade material stresses orginate from bending loads. Stresses are inverse proportional with the area moment of inertia which incorporates thickness to the third power. Hence, propeller mass could be used as auxiliary objective.

1.4.4 Objective 4: Ice-Induced Loading

As the ice-class rules cover the extreme loading conditions, average conditions should be considered as well. Ship propellers should be able to withstand the ice-loading whilst delivering sufficient thrust to propel the ship through ice. Hence, both the ice-induced bending moments as well as the ice-induced torque should be limited such that the main engine can drive the propeller.

While the ice class rules are based on time consuming dynamic time simulations, in this work the prediction will be based on steady state ice milling of the propeller through an infinite ice mass. The simplified ice-failure model of Soininen (1998) will be used to prescribe the ice-induced pressure on a propeller blade.

[2] Only after the unsteady computation has converged, when the initial transients are negligible and inflow conditions and propeller speed remain constant.

The average ice-induced loading over a range of operation conditions from J = 0.2 to 0.7 is considered to obtain a well performing propeller in ice. From the prediction of the total ice force, the propeller root bending moment M_B and ice-induced torque M_Q can be used as objectives. In the context of ice-performance, the ice induced torque is to be limited. When minimizing for the bending moment, the propeller will be less prone to damage.

1.4.5 Constraint 1: Material Stresses

Following the ice-class rules, blade strength is the most important ice strengthening criterion; the drive train of the reference ship is assumed to comply to strength and fatigue requirements. Furthermore, the ice class rules assume that hydrodynamic loads are incorporated in the load cases. Hence, no additional hydrodynamic loads are considered at all.

For CPPs, spindle torque limits together with properly estimated hub-sizes would be required, while detailed fatigue life computations might disapprove best designs. However, in this study FPPs are considered while it is assumed that fatigue strength is sufficient since fatigue is explicitly based on the stresses from the ice-class load cases.

It is assumed that maximum stress from either ice-load case is the only governing criterion for ice-class propellers. The five load cases of the ice-class rules are considered for each propeller in a computational structural analysis. The maximum stress σ_m out of the five load cases is compared with the reference value σ_{ref}, which is given in the ice-class rules (TraFi, 2011, p. 38) as the lesser of:

$$\sigma_{ref} = 0.7\sigma_u, \qquad \sigma_{ref} = 0.6\sigma_{0.2} + 0.4\sigma_u \tag{4}$$

in which σ_u the ultimate tensile strength and $\sigma_{0.2}$ the 0.2% proof stress. While σ_u gives the ultimate strength allowing any permanent plastic deformations, $\sigma_{0.2}$ gives the stress at which the material experiences only 0.2% plastic strain. Hence, the ice class rules allow plastic deformation to a certain degree, although this is limited by their prescription of a safety factor in the final comparison equation,

$$\frac{\sigma_{ref}}{\sigma_m} \geq 1.5 \tag{5}$$

that defines the stress constraint within the optimization for each load case.

1.4.6 Constraint 2: Design Point Iteration

Within an optimization, propellers are compared on their performance in a certain design point. Ship speed and the required thrust should be prescribed. In this study also propeller diameter and hub size, rotational speed and blade area ratio are constant as they would introduce a bias in the objectives. Rotational speed and propeller diameter are strongly correlated with efficiency by means of the advance ratio. The optimization would converge to highly pitched, large diameter propellers working at low rotational speed which cannot be driven by the machinery installations. An iterative procedure is developed by Foeth (2013) which adapts the propeller's mean pitch to obtain the required thrust. Within the optimization, a constraint should ensure convergence of this procedure.

1.5 Case Study

The reference point for this study is the 'Streamline tanker'. Design and optimization studies in the 7th-Framework European project STREAMLINE[3] considered as common baseline the 7000 [DWT], 94 [m] single-screw vessel representative of small-size short-shipping vessels populating European sea routes. Although recent developments resulted in longer ships with larger L/B ratios[4], the Streamline tanker is still useful to take as case study. Only the design conditions and the wake field are important for the current study. For the reader's imagination, the outline of the wake field, the propeller and a picture of the ship are given in an overview in Figure 1-2.

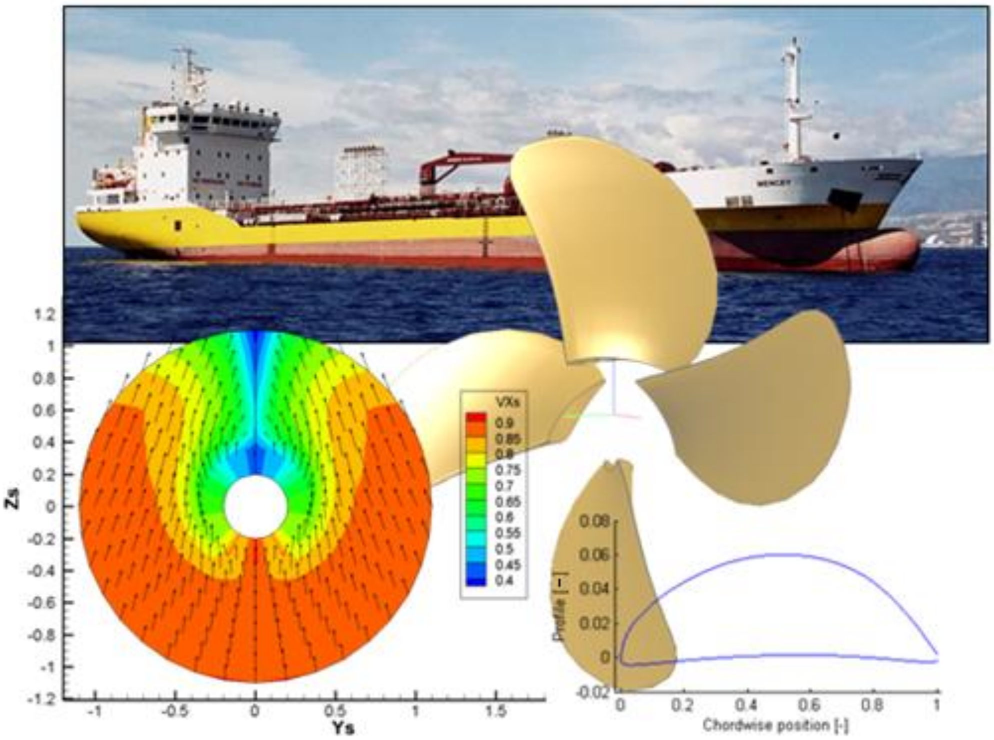

Figure 1-2: Overview of the Streamline tanker. The wake field is given as well as an outline of the reference propeller and a typical blade profile at 0.7R.

The Streamline tanker's design speed is similar to that of newer vessels. Also the shape of the aft-ship and gondola, on which the wake field mainly depends, is assumed to be representative for those newer vessels. Furthermore, not only newer ships are important, results of this study could be used for retrofitting older ships with better propellers. Finally, it is also assumed that the Streamline tanker is representative for ice class ships, although in reality the ship does not have an ice class. The propeller will be assessed on compliance with the ice class rules. The newly designed propeller should automatically comply with them, since the rules are implemented in the computational framework.

Besides the academic value as common test case in CFD, sufficient experimental results and numerical studies are available for the Streamline tanker, e.g. Ploeg (2011), Nuland (2014) and Foeth (2015).

The Streamline tanker's propeller will be referred to as the reference propeller in this study. It will be used as reference in comparison with optimization results. With 4 blades, a diameter of 3.85 [m] and BAR of 0.563 the reference propeller is able to propel the tanker to its design speed of 14 [knots] delivering a thrust of 271 [kN] at 132 [rpm]. In this design point, without ice-class, the reference propeller achieves an efficiency η = 0.648. Its material is a Nickel-

[3] STREAMLINE (Strategic Research for Innovative Marine Propulsion Concepts). http://www.streamline-project.eu/

[4] Ice pieces may float up again before reaching the aft-ship, diminishing the ice-interaction process considerably.

Aluminium-Bronze alloy with a tensile strength of 640 [MPa] and a 0.2% plastic proof stress of 260 [MPa]. The aforementioned properties of the propeller and details of the design point are summarized in Table 1-2.

Table 1-2: Details on the reference propeller and its design point.

Main Particulars			
Diameter	D	3.85	[m]
Blade Area Ratio	BAR	0.563	
Number of Blades	Z	4	
Mass	M	3527	[kg]
Shaft Immersion	h_s	3.75	[m]
Propeller Material			
Tensile strength	σ_u	640	[MPa]
Proof stress	$\sigma_{0.2}$	260	[MPa]
Density	ρ	7650	[kg/m^3]
Design Point			
Speed	V	7.20	[m/s]
Thrust	T	271.0	[kN]
Rotational Speed	n	2.20	[1/s]
Efficiency	η	0.637	
Advance Ratio	J	0.676	
Ice Strength	σ_{ice}	2	[MPa]

1.6 Report Structure

This Master's thesis continues in chapter 2 by considering the physical and theoretical models to describe and analyze the propeller. Also the working principles of the optimization algorithm are addressed.

Chapter 3 follows by explaining and assessing computational methods to solve the theoretical models. Grid refinement and uncertainty studies are carried out in order to find best practice guidelines that lead to the cheapest computation settings which are acceptable within the optimization. Of any propeller blade, both the hydrodynamic behavior and the structural integrity need to be predicted accurately. The ice-load prediction model will be assessed for its sensitivity to blade section geometry in 2D and implemented within the computational framework in 3D. All analysis tools are coupled with the propeller blade geometry generator and an automatic optimization algorithm. The flowchart and implementation details will be considered.

Chapter 4 starts with exploratory tests to check and debug the computational framework. Gradually, through thickness optimization, blade profile optimization with steady and unsteady computations, this chapter continues to full optimization in which the whole propeller is delivered to the capabilities of the optimization algorithm. Upon convergence, the trade-offs between the objectives and constraints are analyzed. Best propellers are assessed for performance.

Finally, the observations and guidelines are presented in conclusions and recommendations in chapter 5 which concludes this Master's thesis.

2 PHYSICAL AND THEORETICAL MODELS

Reality, its modeling and numerical implementations are to be distinguished. In the qualification of a computational method the separate effects of modeling and numerical errors compared to reality should be addressed. Figure 2-1 gives an overview of the modeling of a process in reality. Verification in this framework is a mathematical exercise to show that the physical model is solved correctly to a certain degree of accuracy. Validation is an assessment whether the right conceptual physical model is solved to represent reality (ASME, 2009). Modeling errors are introduced at the right side of Figure 2-1 while numerical errors are present at the left.

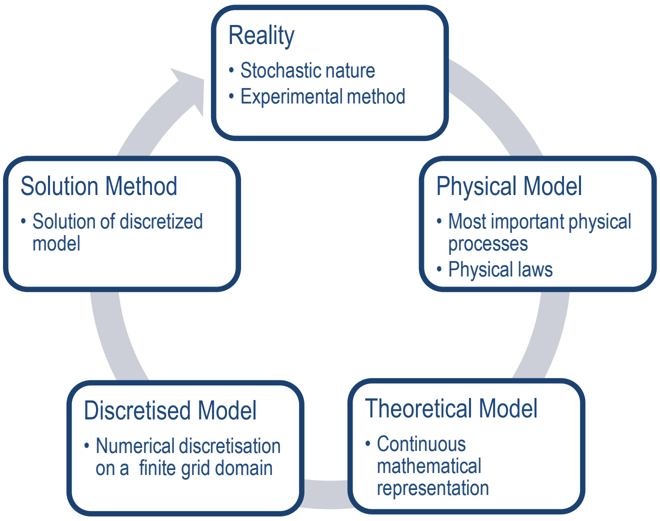

Figure 2-1: Overview of steps in the numerical modeling of reality.

Keeping Figure 2-1 in mind, this chapter considers physical and theoretical models for

1. a description of propeller geometry
2. hydrodynamic behaviour of a propeller behind a ship
3. extent and behaviour of cavitation on the propeller
4. ice loads on a propeller
5. stresses in propeller material due to mechanical loading
6. numerical uncertainties in computational methods
7. optimization of large, advanced systems

as ingredients of the computational framework. These subjects will be reviewed with their assumptions, strengths and limitations. The enumeration will be followed in the subsequent sections.

2.1 Propeller Blade Geometry

A description of traditional propeller geometry is given by means of a parameterization in radial and chordwise direction. Table 2-1 summarizes all parameters involved and some of their related parameters. As explanation the following should be noted:

- The global parameters define the overall size of the propeller blades while radial distributions shape the propeller blade outline.
- Chordwise distributions are used to design blade foil profiles which are constant over the radius.
- Details are not parameterized, and should be considered separately afterwards in detailed engineering.
- From the global parameters and the distributions, related parameters can be derived which are traditionally used to describe the propeller.

For propeller terminology the reader is referred to the standards of the ITTC (1999).

Table 2-1: Propeller geometry parameterization.

Global	Radial distributions	Chordwise distributions	Details	Related
Diameter	Pitch	Camber	Hub shape	Effective pitch
Hub size	Chord	Thickness	Root fillet	Blade Area Ratio
Number of blades	Skew		Edges	Skew angle
	Rake		Roughness	*and many more...*
	Camber			
	Thickness			

Besides skew [rad], the radial distributions are in [m] made dimensionless with propeller diameter. Chordwise distributions are dimensionless since they should be scaled with their corresponding radial distributions. To visualize and analyze the propeller, the six radial distributions and two chordwise distributions are converted and dimensioned into a point cloud in a Cartesian coordinate system. The steps are itemized in Table 2-2:

Table 2-2: Itemization of the steps involved in the conversion of propeller geometry from distributions to a point cloud.

Discretize	• all distributions with sufficient resolution
Scale	• chordwise distributions with their corresponding radial distributions
Add	• or subtract the thickness distribution from the camber distributions
Create	• blade foil geometry at each radial position.
Scale	• sections with chord length
Rotate	• sections with local pitch angle.
Translate	• sections by adding local rake.
Add	• skew in a cylindrical coordinate system
Convert	• to Cartesian coordinates to obtain a point cloud of chosen resolution.
Scale	• point cloud with propeller diameter for dimensioned propeller blade.

A coordinate transformation is convenient when adding skew to the propeller geometry description to include both the skew-induced rake translation and skew rotation.

2.1.1 Bézier Curves

Conform the parameterization of Table 2-1 a large family of propellers can be generated. In this Master's thesis the radial and chordwise distributions are limited to first-order smooth functions though. A description by means of Bézier curves is used.

An elaboration on the working principles and mathematics of Bézier curves can be found in e.g. the course notes of Sederberg (2014). The implementation of the curves, with their specific properties, is reported by Foeth (2013, 2015) and Nuland (2014). A concise summary of the working principles is given below.

With reference to Sederberg (2014) and Figure 2-2, the equation of a Bézier curve is similar to the equation of the center of mass $\boldsymbol{P}$ of a set of point masses m_0, m_1, m_2 and m_3 which are located at points $\boldsymbol{P_0}, \boldsymbol{P_1}, \boldsymbol{P_2}$ and $\boldsymbol{P_3}$ respectively:

$$\boldsymbol{P} = \sum_{i=0}^{3} \frac{m_i \boldsymbol{P_i}}{m_i} \tag{1}$$

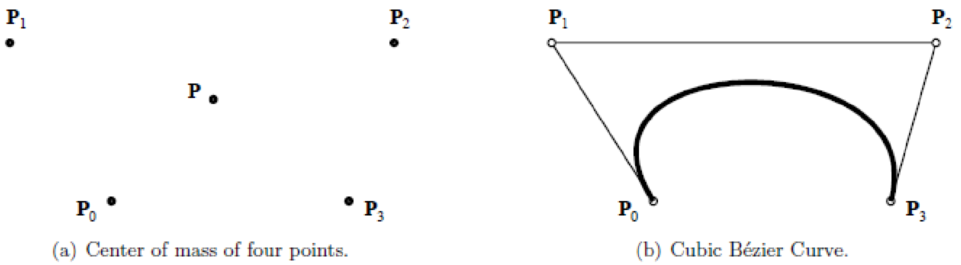

Figure 2-2: Working principle of a cubic Bézier curve. [Copied from Sederberg (2014, p.18)]

For a continuous curve, the masses should be varied as function of a parameter t, such that point $\boldsymbol{P}$ in Figure 2-2a is swept into the curve of Figure 2-2b. For a Bézier curve of order n, mass functions $m_i^n = m_i^n(t) = B_i^n(t)$ are called Bernstein polynomials. In this work usually cubic curves are used, i.e., $n = 3$ as in Figure 2-2. The Bernstein polynomials for a cubic curve as function of t are given in Figure 2-3. The general equation of a Bernstein polynomial $B_i^n(t)$ for point $\boldsymbol{P_i}$ can be written as[5]:

$$B_i^n(t) = w_i \binom{n}{i} (1-t)^{n-i} t^i \tag{2}$$

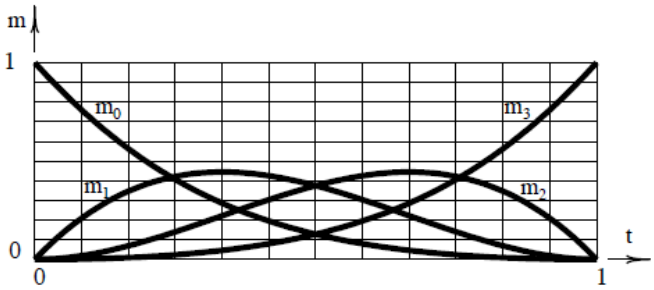

Figure 2-3: Bernstein polynomials for a cubic Bézier curve. [Copied from Sederberg (2014, p.19)]

For a standard cubic Bézier curve, weights w_i are equal to one. Although not utilized in this work, more shapes may be generated by varying the weights in addition to the location of the points.

The shape of the polynomials explains why the Bézier curve passes through its start and end point, further referred to as control points. The other points, $\boldsymbol{P_1}$ and $\boldsymbol{P_2}$, are referred to as handle points. Control points can be seen as nodes through which the curve goes and are explicitly used to define start and end points. Handle points are used to define the shape of the curve. A cubic Bézier curve is tangent to the poly-line connecting a control point and its handle point. As such, joining two Bézier curves generates a first-order smooth, continuous

[5] $\binom{n}{i} = \frac{n!}{(i!(n-i)!)}$ is a binomial coefficient.

curve by prescribing equal tangents at the joint. This joint can be used to define the location of an extreme.

2.1.2 Propeller Parameterization

Referring to Table 2-1, each radial and chordwise distribution can be described by means of Bézier curves. By means of their control and handle points different distributions may be created. In an optimization the coordinates of the control and handle points are the design parameters that are tuned by the optimization algorithm. Hence, the number of design parameters should be limited, while the design space should be as large as possible within generating infeasible[6] propeller geometry. Three types of parameterizations have been used as shown in Figure 2-4. Their philosophy is as follows:

1. Allow maximum design freedom which is required for the radial skew, rake, camber and thickness distributions. Hence, six design variables per distribution are used, namely c_{hub}, hx_{hub}, hy_{hub}, hx_{tip}, hy_{tip} and c_{tip}.
2. Limit the number of design variables by defining the extreme point and bounding the handle points. This is used for the chord distribution and in less extent for the pitch distribution. For the chord and pitch distribution, three and five variables are used respectively. For the radial chord distribution, $h_{tip} = 1$ and $r_{tip} = 100\%$ are prescribed. r_{hub} gives the reduction of chord and pitch at the hub while r_{tip} specifies the reduction at the tip. Note that the y-position of h_{hub}, c_{MAX} and h_{tip} is specified by the blade area ratio and mean pitch for the radial chord and pitch distribution respectively.
3. Control of the position of the extreme and the width of the curve for the chordwise thickness and camber distributions. As the leading edge curvature is important, the thickness distribution is controlled by four variables while the camber distribution is prescribed by only three variables, leaving $h_{LE}(y)$ constant. Note that only one blade profile distribution is used in radial direction, leaving varying blade profiles over radius for future work.

Figure 2-4 indicates control points with red squares, while green circles represent the handles of the control points. Labeled points may be varied as design parameters.

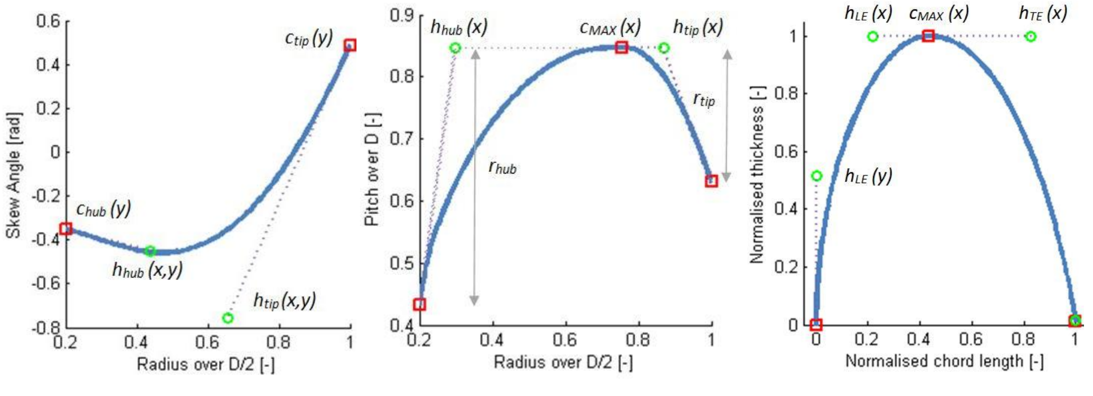

Figure 2-4: Examples of distributions in which the propeller is parameterized.

Bounds and constraints on the parameterized distributions will be developed during the test phase of the computational framework in section 4.1. An overview of all design variables with their bounds is given in Appendix A.

2.1.3 Grid Generation Procedure

Both the hub and the blade should be discretized for computational analysis. The hub is built from a series of helices and rings along the root pitch line. Their intersections form the grid-points. The blade grid generation procedure is shortly considered in the enumeration below:

[6] Such that the geometry cannot be generated by the procedure of Table 2-2 due to intersections, discontinuities or overlap.

1. Convert tabular data of the distributions into splines or Bézier curves
2. Define hyperbolic tangent distributions in radial and chordwise direction.
3. Evaluate the splines of the distributions and the blade sections at the new radial positions.
4. Transform to a point cloud according to Table 2-2. This defines the grid-points.

2.2 Hydrodynamic Analysis

The purpose of hydrodynamic propeller analyses in this study is the fast computation of the efficiency of a propeller behind a ship and its cavitation pattern. Consequently, simplifications have to be made as much as possible for an acceptable balance between computational time and validity.

2.2.1 Governing Equations

Fluid dynamics are governed by conservation laws of classical physics. Mass, momentum and energy should be conserved in an arbitrary material volume $V(t)$. Conservation of mass implies that the rate of change of mass in $V(t)$ equals the rate of mass production in $V(t)$, or

$$\frac{d}{dt}\int_{V(t)} \rho \,\mathrm{d}V = \int_{V(t)} \sigma \,\mathrm{d}V = 0 \tag{3}$$

where $\rho = \rho(t, \boldsymbol{x})$ and $\sigma = \sigma(t, \boldsymbol{x})$ are the local density and rate of mass production at time t and position $\boldsymbol{x}$. For normal propeller analyses the mass production is zero within $V(t)$. Single phase flow is assumed, cavitation and ventilation are not resolved directly. Using Reynolds transport theorem[7], Equation (3) can be expressed as

$$\int_{V(t)} \left(\frac{\partial \rho}{\partial t} + \nabla \cdot (\rho \boldsymbol{u})\right) \mathrm{d}V = 0 \tag{4}$$

$$\frac{\partial \rho}{\partial t} + \nabla \cdot (\rho \boldsymbol{u}) = 0 \tag{5}$$

Further simplification can be obtained when assuming incompressible flow: density differences due to fluid velocities are negligible. Conform the continuum hypothesis and the incompressibility assumption the flow density remains constant within the domain as density differences due to temperature or salinity are not considered. Equation (5) reduces to the continuity equation:

$$\frac{\partial \rho}{\partial t} + \nabla \cdot (\rho \boldsymbol{u}) = \frac{\partial \rho}{\partial t} + \rho \nabla \cdot \boldsymbol{u} + \boldsymbol{u} \cdot \nabla \rho = \rho \nabla \cdot \boldsymbol{u} = 0 \tag{6}$$

$$\nabla \cdot \boldsymbol{u} = 0 \tag{7}$$

Irrotational Flow Hypothesis

Furthermore, considering the hypothesis of irrotational flow in addition to the continuity equation, requires per definition that the curl or vorticity of the flow is zero:

$$\boldsymbol{\zeta} = \nabla \times \boldsymbol{u} = \boldsymbol{0} \tag{8}$$

An order-of-magnitude analysis of the vorticity equation[8] shows that at high Reynolds numbers the vorticity at the solid boundaries, where viscosity introduces shear, convects faster than it diffuses. Hence, vorticity remains in the boundary layer and is shed into the trailing wake as sketched in Figure 2-5. The external flow is hardly influenced.

[7] For a derivation and explanation of Reynolds transport theorem the reader is referred to standard fluid mechanics textbooks, e.g. White (2011)
[8] The vorticity equation is obtained by taking the curl of the Navier-Stokes equations. Order-of-magnitude analysis is explained by e.g. Tennekes & Lumley (1972) and Katz & Plotkin (2001)

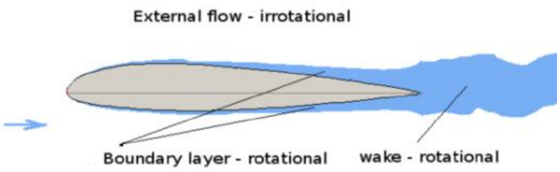

Figure 2-5: Sketch of blade profile in a flow [after Auld (2015)]

Since mutual shear forces between fluid elements are negligible, fluid in the outer portion of the flowfield will remain irrotational if a uniform irrotational inflow would be assumed. A solution of the outer portion provides the pressure distribution and related forces on the body, whereas the boundary layer is important for the frictional forces and the induced pressure drag.

Boundary layer thickness is negligible compared to the blade profile thickness. The pressure distribution on a propeller largely defines its performance in terms of thrust and torque. Hence, a solution of the outer portion of the flow will suffice for initial propeller geometry optimization. A correction for the viscous drag on the surface of the blade profile should be applied based on empirical methods such as flat plate resistance as function of Reynolds number.

However, in behind ship conditions, the inflow is highly disturbed and rotational. A further simplification is the introduction of the effective wake just in front of the propeller. It takes the mutual effect of ship wake and propeller induced velocities into account. Rotationality is advected in the effective wake velocity field such that Equation (8) can still be prescribed.

Definition of the Potential

Rewriting Equation (8) gives the following requirement[9]

$$\frac{\partial}{\partial x_i} u_j = \frac{\partial}{\partial x_j} u_i \tag{9}$$

for $i \neq j$. This can only be the case if a scalar function ϕ exists such that:

$$u_\alpha \equiv \frac{\partial \phi}{\partial x_\alpha} \quad \text{or} \quad \boldsymbol{u} \equiv \nabla \phi \tag{10}$$

Substitution in the continuity equation yields a Laplace equation:

$$\nabla \cdot \boldsymbol{u} = \nabla \cdot \nabla \phi = \Delta \phi \tag{11}$$

$\phi = \phi(t, \boldsymbol{x})$ is called the velocity potential function and can only be defined for potential flow, i.e., divergence free, irrotational flow. A solution of ϕ provides the velocity distribution within the domain. Note that irrotational, divergence free flow is also inviscid. Viscosity is the resistance to fluid shearing. In a divergence free flow, without fluid rotation no shear motions will occur. Hence, viscosity cannot play a role.

Conservation of Momentum

Furthermore, conservation of momentum is governed by Newton's second law of motion:

$$\frac{d}{dt} \int_{V(t)} \rho \boldsymbol{u} \mathrm{d}V = \int_{V(t)} \rho \boldsymbol{F^b} \, \mathrm{d}V + \int_{S(t)} \boldsymbol{F^s} \mathrm{d}S \tag{12}$$

---

[9] Note that the correct index notation would be $\epsilon^{ijk} \boldsymbol{e}_i \frac{\partial}{\partial x_j} u_k = 0$.

where body forces $\boldsymbol{F^b}$ are proportional to mass and surface forces $\boldsymbol{F^s}$ work on the surface of the body proportional to its area $S(t)$. Under the divergence free and irrotationality assumptions, shear forces are not present. This leaves $\boldsymbol{F^s} = -p \cdot \boldsymbol{n}$ where p denotes pressure. If a stationary frame of reference is considered, only gravity acts as body force. Hence, $\boldsymbol{F}^b = -\boldsymbol{g}$ where $\boldsymbol{g}$ denotes the constant gravity vector. Writing in index notation, applying Reynolds transport theorem on the first term in Equation (12) and the divergence theorem on the third term yields:

$$\int_{V(t)} \left[\frac{\partial \rho u_\alpha}{\partial t} + \frac{\partial}{\partial x_\beta} (\rho u_\alpha u_\beta) \right] \mathrm{d}V = \int_{V(t)} -\rho g_\alpha \mathrm{d}V - \int_{V(t)} \frac{\partial p}{\partial x_\alpha} \mathrm{d}V \tag{13}$$

where the repeated subscript β implies summation by the Einstein convention to denote the divergence in the second term. Since this equation should hold at any time for every $V(t)$ it should be that

$$\rho \frac{\partial u_\alpha}{\partial t} + \rho u_\beta \frac{\partial u_\alpha}{\partial x_\beta} = -\rho g_\alpha - \frac{\partial p}{\partial x_\alpha} \tag{14}$$

where the continuity equation was used to simply the divergence in the second term of Equation (13). The assumption of incompressible flow has been used to simply the first and second term by considering ρ constant.

Energy Equation

Equation (14) is the Euler equation for inviscid, incompressible flow. Note that this equation simplifies further if the irrotationality hypothesis would be applied. There exists a vector identity[10] that rewrites the convective term in terms of vorticity, which is zero, and the change in kinetic energy:

$$u_\beta \frac{\partial u_\alpha}{\partial_\beta} = -(\boldsymbol{u} \times \boldsymbol{\zeta})_j + \frac{\partial}{\partial x_\alpha} \left(\frac{1}{2} u_\beta^2 \right) \tag{15}$$

where $\boldsymbol{\zeta} = \nabla \times \boldsymbol{u} = \boldsymbol{0}$ the vorticity vector. Substitution in the Euler equations followed by the usage of the potential function, yields the energy equation:

$$\rho \frac{\partial u_\alpha}{\partial t} + \frac{\partial}{\partial x_\alpha} \left(\frac{1}{2} \rho u_\beta^2 + p + \Phi \right) = 0 \tag{16}$$

$$\frac{\partial}{\partial x_\alpha} \left(\rho \frac{\partial \phi}{\partial t} + \frac{1}{2} \rho (\nabla \phi)^2 + p + \Phi \right) = 0 \tag{17}$$

where $\Phi = \rho g z$ is the potential energy of gravity with z a coordinate in the direction of the gravitational field. Hence it follows, supplementary to the Laplace equation, that

$$\frac{\partial \phi}{\partial t} + \frac{1}{2} (\nabla \phi)^2 + \frac{p}{\rho} + g z = \text{constant} \tag{18}$$

within the flow to relate velocities to pressures. Equation (18) is the unsteady Bernoulli equation.

[10] For proof see e.g. Eggers (2012). For clarity and understanding, a mixed vector and index notation is used. Effectively, the momentum equation changes into an energy equation.

2.2.2 Lift Generating Bodies

White (2011), however, points out that a potential flow theory solution is non-unique since circulation is not taken into account. The lift on a body is proportional to its circulation Γ by the Kutta-Joukowski lift theorem. Hence, circulation should be addressed and solved as well.

Circulation

Circulation is defined as the line integral of the velocity field around a closed curve C, or in words, the amount of fluid rotation within a closed contour. Circulation Γ is related with vorticity by Kelvin-Stokes' theorem[11]:

$$\Gamma = \oint_C \boldsymbol{u} \cdot \mathrm{d}\boldsymbol{C} = \int_S (\nabla \times \boldsymbol{u})\, \mathrm{d}S \tag{19}$$

which states that without vorticity, i.e. irrotational flow, $\boldsymbol{\zeta} = \nabla \times \boldsymbol{u} = \boldsymbol{0}$, there cannot be any circulation. Hence, the irrotationality assumption prevents lift generation.

Wake Surface

If circulation would be manually added to a lifting body in potential flow, there should be a surface S_w in the wake that carries the shedded vorticity between lifting body and the far field. The wake surface is an infinitesimal small vorticity layer which is discontinuous for the velocity potential, while the pressure and the normal component of velocity must be continuous.

The wake surface should be a stream-surface of the flow such that no flow can pass through this surface and the pressure difference of the wake surface should be zero. This wake is included in the hydrodynamic analysis, varying from fully prescribed wakes supplied with empirical models for contraction to iterative wake-alignment methods with the above boundary conditions.

Kutta Condition

The Kutta condition forces the flow to behave like a viscous flow with the correct circulation. Physically, the Kutta condition forces the flow to leave the trailing edge smoothly like in real viscous flows. The rear stagnation point is artificially moved to the trailing edge due to the pressure equality. Mathematically, the Kutta condition states that the potential jump at the wake adjacent to the trailing edge should be equal to the difference of the potential values ϕ_s and ϕ_p at the suction and pressure side of the trailing edge (Morino, 1993):

$$\Delta\phi_{TE} = \phi_s - \phi_p \tag{20}$$

such that the potential difference, or simulated circulation, is carried by the wake surface.

Equation (20) does not necessarily satisfy the pressure equality at the trailing edge and over the wake surface, either due to unsteady effects by $\partial\phi/\partial t$ in the Bernoulli equation or due to deviation from local 2D flow by 3D effects. It can only be used for steady computations where there is no temporal variation in lift and the flow behaves as 2D plane flow.

An Iterative Pressure Kutta Condition (IPKC) should be used instead to explicitly prescribe the pressure at the trailing edge. Effectively, as Kerwin et al. (1987) states, the IPKC ensures in addition to Equation (20), the pressure equality between the suction and pressure sides of the trailing edge. The difference in pressure at suction and pressure side of the trailing edge, which is a function of the potential difference of Equation (20) by Bernoulli's equation, should be zero, yielding the non-linear equation

[11] This theorem is, similar to the divergence theorem, a special case of the general Stoke's theorem $\int_{\partial\Omega} \omega = \int_{\Omega} \mathrm{d}\omega$.

$$\Delta p(\Delta\phi_{TE}) = 0 \tag{21}$$

which should be solved each time step using an iterative method like Newton-Raphson iteration as proposed by Kerwin et al. (1987) and applied by Vaz & Bosschers (2006).

2.2.3 Fundamental Potential Flows

Focusing again on the governing equation, it should be noted that a Laplace equation is linear. Superposition of different potentials is possible. Elementary potentials satisfying the Laplace equation in axi-symmetric polar coordinates r, θ are uniform flow

$$\phi_u = Ur\cos(\theta) \tag{22}$$

and point sources

$$\phi_s = -\frac{\gamma}{r} \tag{23}$$

in which U and γ define their respective strengths. For a propeller, the flow field can be regarded as disturbance in a uniform flow[12]. Hence, the total potential can be written as

$$\phi = \varphi + \phi_u \tag{24}$$

where φ the disturbance potential which is to be solved. The disturbance potential can be compiled from sources, sinks and doublets. Their appearance in the governing equation will become clear from the next section.

A doublet can be created by placing two sources with strengths γ and $-\gamma$ close to each other. Taking the limit of their distance yields

$$\phi = \frac{\lambda\cos\theta}{r^2} \tag{25}$$

with λ as strength. Streamlines for a source and a doublet are drawn in Figure 2-6.

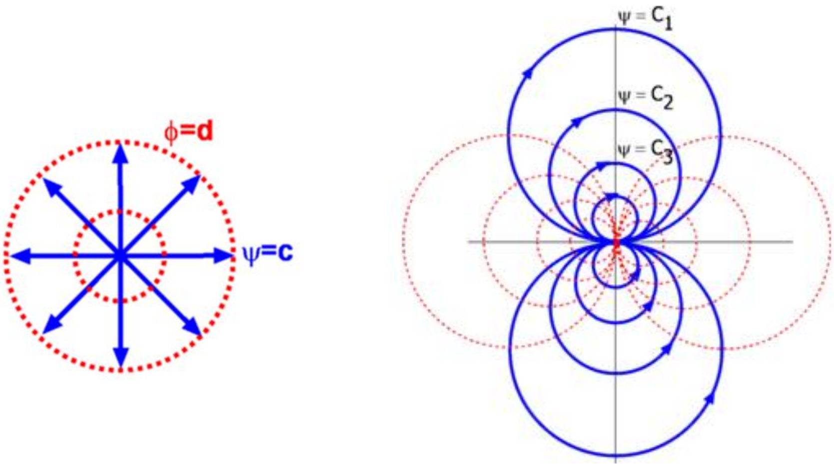

Figure 2-6: Source (left) and doublet (right). Red dotted lines give iso-potentials, blue solid lines represent streamlines. [Copied from Auld & Srinivas (2006)]

2.2.4 Boundary Element Method

The influence of the exact 3D propeller geometry is important for optimization purposes. Moreover, a full solution of the flow pattern within $V(t)$ is less important than the solution of

[12] Uniform in x-direction. Either prescribed by a wake field or uniform in radius as well.

resulting pressures on the propeller surface only. Hence, a boundary solution could suffice. This gives rise to a 3D Boundary Element Method (BEM).

Consider the integration of the governing equation (11) for the disturbance potential φ over $V(t)$, multiplied with some scalar function ϕ_r

$$\int_{V(t)} (\Delta\varphi)\phi_r \mathrm{d}V = \int_{V(t)} (\nabla \cdot \nabla\varphi)\, \phi_r \mathrm{d}V = 0 \tag{26}$$

Multiplication with ϕ_r is mathematically required to solve the problem. Since the discretized domain is likely to be not smooth enough to justify the use of the divergence theorem, a weak formulation is used[13]: ϕ can be solved relative to test or shape functions ϕ_r. A convenient test function for potential flow problems is the potential of a point source with strength $-\frac{1}{r}$ which always satisfies the governing equation.

By virtue of the divergence theorem, integration by parts and vector derivative identities, Green's second identity[14] can be derived from Equation (26). It relates the outward flux through a closed surface to the behavior of the flow within the surface.

$$\int_{V(t)} (\nabla \cdot \nabla\varphi)\, \phi_r \mathrm{d}V = \int_{S(t)} \boldsymbol{n} \cdot (\nabla\varphi)\, \phi_r \mathrm{d}S - \int_{V(t)} (\nabla\varphi) \cdot (\nabla\phi_r) \mathrm{d}V = 0 \tag{27}$$

Integration by parts a second time yields Green's second identity, formulated as

$$\begin{aligned} \int_{V(t)} (\nabla \cdot \nabla\varphi)\, \phi_r dV = &\int_{S(t)} [\boldsymbol{n} \cdot (\nabla\varphi)\, \phi_r - \boldsymbol{n} \cdot (\nabla\phi_r)\varphi]\, dS \\ &+ \int_{V(t)} (\nabla \cdot \nabla\phi_r)\, \varphi dV = 0 \end{aligned} \tag{28}$$

or after rearrangement

$$\int_{V(t)} [(\Delta\varphi)\, \phi_r - (\Delta\phi_r)\varphi]\, dV = \int_{S(t)} [(\nabla\varphi)\, \phi_r - (\nabla\phi_r)\varphi] \cdot \boldsymbol{n}\ dS = 0 \tag{29}$$

Hence, instead of solving Equation (26) in the whole volume $V(t)$, φ can also be solved on the volume's surfaces $S(t)$ only, i.e., by solving:

$$\int_{S(t)} [(\nabla\varphi)\, \phi_r - (\nabla\phi_r)\varphi] \cdot \boldsymbol{n}\ dS = 0 \tag{30}$$

Before substituting ϕ_r it should be noted that ϕ_r is singular for $r \to 0$ in the origin P from which distance r is defined. Imagine an infinitesimal small sphere within $V(t)$ with radius ϵ around P with $\int dS = 4\pi\epsilon^2$, as sketched by Katz & Plotkin (2001) in Figure 2-7. Within this sphere φ does not vary anymore, i.e., $\nabla\varphi$ can be neglected and Equation (30) reduces to

$$\int_{S_\epsilon} \frac{\varphi(P)}{r^2}\, dS = 4\pi\varphi(P) \tag{31}$$

with $r = \epsilon$. Subtracting singular point P from Equation (30) while substituting ϕ_r yields

[13] In-depth explanation of the weak formulation and test functions are is considered outside the scope of this thesis, but can be found in e.g. course notes of Sayas (2008) for an easy understanding or any mathematical text on the Finite Element Method for which weak formulations are also used.

[14] Mathematically, Green's second identity is explained in more detail in the first chapters of the course notes of Antes (2010).

$$\varphi(P) = \frac{1}{4\pi}\int_{S(t)} \left(\frac{1}{r}\nabla\varphi - \varphi\nabla\left(\frac{1}{r}\right)\right)\cdot \boldsymbol{n}\, dS \tag{32}$$

This equations states that the disturbance potential in point P can be written in terms of the disturbance potential on the other surfaces within $V(t)$ taking into account their distance r to P. For a further explanation and usage of this equation, Figure 2-7 should be considered. Equation (32) can be split for each surface. Besides the small sphere with surface S_ϵ, the domain $V(t)$ is shown with far field boundary S_∞. Furthermore, closed lifting body B with body surface S_B is accompanied with its wake surface S_w.

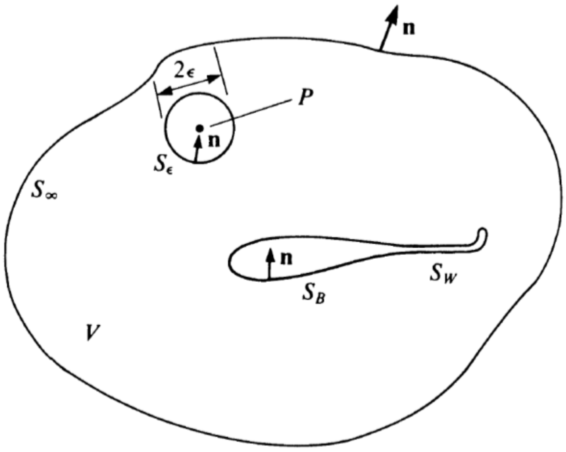

Figure 2-7: Definition of potential flow problem for a lifting body. [Copied from Katz & Plotkin (2001, p.45)]

The wake surface S_w contains no sources since the normal velocity should be continuous[15]. A potential flow solution within $V(t)$ can be divided into a flow outside S_B with solution φ and an imaginary flow inside S_B. This imaginary flow is not considered further, but both flows share a streamline at the solid boundary S_B, simulating the solid boundary of the propeller.

Taking all surfaces into account, Equation (32) can be expanded as

$$\begin{aligned}\alpha(P)\varphi(P) = &\frac{1}{4\pi}\int_{S_B(t)} \left(\frac{1}{r}\nabla\varphi - \varphi\nabla\left(\frac{1}{r}\right)\right)\cdot \boldsymbol{n}\, dS \\ &- \frac{1}{4\pi}\int_{S_W(t)} \varphi\nabla\left(\frac{1}{r}\right)\cdot \boldsymbol{n}\, dS + \phi_\infty(P)\end{aligned} \tag{33}$$

in which the potential at the far field boundary $\phi_\infty(P)$ is assumed to be zero. Note that $\gamma = \nabla\varphi$ can be regarded as a source strength, while $\mu_B = \varphi$ and $\mu_W = \varphi$ can be seen as dipole strengths from Equations (23) and (25). Note also that for non-lifting flow a distribution of sources would suffice. Sources are chosen such that a streamline is formed on the boundaries of the body. Lifting bodies require dipoles as well to simulate circulation. A factor α is added which depends on the location of P. For P outside V, $\alpha = 0$ and for P inside V, $\alpha = 1$. For P on a boundary, $\alpha = \frac{1}{2}$ since only half of S_ϵ surrounding P should be taken into account.

Discretization

For a boundary solution of the flow, the blade and wake surfaces can be discretized into elements according to section 2.1.3. The centre of each element is a collocation point P for which Equation (33) should be solved. A system of equations is obtained for each element i in which φ_i, γ_i, μ_{B_i} and μ_{W_i} are unknowns to be solved. Equation (33) gives the potential at point P induced by the distribution of sources and dipoles on surfaces S_B and S_W. A full matrix equation should be solved for the potential at each discrete point within the domain.

[15] Mathematical treatment of the boundary condition is given in Koning Gans (2012).

Now the sum of induced velocities from the sources and doublets forms the total flow field from which the pressures can be calculated by Bernoulli's equation (18).

2.2.5 Boundary Conditions

To be able to solve the propeller problem, the Laplace equation should be supplied with proper boundary conditions. The most important boundary condition is the no-penetration Neumann condition at the propeller surface S_B which implies that the normal velocity is zero, i.e.

$$\boldsymbol{n} \cdot \boldsymbol{u} = \boldsymbol{n} \cdot (\nabla\varphi + \boldsymbol{U}_\infty) = 0 \tag{34}$$

or

$$\boldsymbol{n} \cdot \nabla\varphi = -\boldsymbol{n} \cdot \boldsymbol{U}_\infty \tag{35}$$

where $\boldsymbol{n}$ the normal on the propeller surface and $\boldsymbol{U}_\infty$ the free stream velocity which depends on the wake, angular and radial position and rotational speed. Hence the source strength γ_i on S_B is determined by Equation (35). The source will have positive strength at the leading edge while at the trailing edge the source will be a sink to force the flow around the profile and satisfy the continuity equation. As already noted, the far field boundary condition is given as

$$\varphi_{S_\infty} = 0 \tag{36}$$

Because of the boundary conditions, Equation (33) only has be solved for dipole strengths and the unknown potentials in the collocation points with aid of the Iterative Pressure Kutta Condition.

2.3 Cavitation Analysis

Cavitation is regarded as a constraint due to its possible erosive characteristics. Cavitation is formed when the liquid's pressure drops below its vapour pressure (White, 2011, p. 34). Vapour bubbles are formed in the fluid, possibly causing damage upon implosion. Cavitation should be taken into account in every propeller design. Cavitation may influence propeller performance in terms of vibrations, noise and erosion. A well balanced design allows as much as possible cavitation without experiencing any hindrance.

The difference between the local pressure and the vapour pressure is an indication for cavitation inception. Bernoulli's Equation (18), neglecting gravity effects and assuming steady, incompressible, inviscid flow, can be used to express the pressure variation along the streamline of a body, or in this case a cavity surface:

$$p_{ref} + \frac{1}{2}\rho U_{ref}^2 = p_v \tag{37}$$

in which p_{ref} and U_{ref} are characteristic pressure and velocity at the location of interest, respectively, ρ is the density of water and $p_v = 1706$ [Pa] is the vapour pressure which is taken as reference in this Master's thesis. The cavitation number σ is formed from this relation. It gives the relation between the static and dynamic pressure head:

$$\sigma = \frac{p_{ref} - p_v}{\frac{1}{2}\rho U_{ref}^2} \tag{38}$$

As a reference the pressure at the propeller shaft is often taken with:

$$p_{ref} = p_a + \rho g h_s \tag{39}$$

$$U_{ref} = nD \tag{40}$$

in which $p_a = 101325$ [Pa] the atmospheric pressure, $\rho g h_s$ the static pressure head at the $h_s = 3.75$ [m] immersed propeller shaft[16]. The characteristic velocity for the reference cavitation number is rotational speed n times diameter D. The cavitation number acts as a measure for the vulnerability to cavitation. Higher numbers indicate that cavitation is less likely to occur.

At each location on the propeller with its local velocity and pressure the pressure coefficient

$$C_p = \frac{p - p_{ref}}{\frac{1}{2}\rho U_{ref}} \tag{41}$$

can also be evaluated and compared with the reference number:

$$-C_p \leq \sigma \tag{42}$$

If Equation (42) holds, cavitation is likely to occur. In general, bubble cavitation can be well-predicted by means of the cavitation number. Sheet cavitation, however, is initiated by the suction peak at the leading edge. A vapour sheet builds up which may remain attached to the propeller surface or separate and form erosive cloud cavitation. This process is highly dynamic and not limited to areas for which Equation (42) holds. Sheet cavitation can iteratively be solved in a hydrodynamic BEM analysis. The procedure is based on Fine (1992) and further described and implemented by Vaz (2005) and Bosschers (2009).

An additional cavitation surface S_C is added to the BEM with four boundary conditions. In words:

1. Sheet cavitation should be aligned with a streamline of the flow. Formally, a kinematic boundary condition states that any point on the cavity surface should remain there, or that the cavity surface is a material surface of the flow.
2. The pressure within a cavity is equal to vapour pressure p_v. Hence, it can be imposed that also the pressure on S_C should equal p_v.
3. While in reality cavity closure is highly complex with a re-entrant jet, closure conditions should be specified. The pressure recovery model form Salvatore et al. (2003) was chosen by Bosschers (2009) which models the closure as a region in which pressure is gradually recovered.
4. Also detachment conditions should be considered in order to have a continuous boundary of flow domain V. The detachment point may either be fixed on the leading edge which is valid for most blade profiles or be located at the point of minimum pressure.

In a BEM, the location of S_C is part of the solution of the boundary value problem specified by conditions 1. and 2. above. Each time-step an iterative procedure is to be applied to estimate the cavity extent. Source strength on the cavity is unknown, while dipole strength is related to the dipole strength at the detachment point. The cavity surface can be considered frictionless, such that no additional vorticity is introduced here.

Regarding the cavity thickness to be small compared to the blade profile thickness avoids mesh generation on the cavity surface. Boundary conditions are transferred to the propeller surface or wake surface in case of super cavity which extends beyond the propeller in the wake.

Further explanation and mathematical details are not given here since cavitation will not be considered within the optimization. Optimized propellers will be checked on their behaviour afterwards as design check.

[16] Shaft immersion h_s = 3.75 [m]is given for the reference 'Streamline' tanker

2.4 Ice Loads

Propellers operating in ice should be able to withstand the high impact loads. Ice class rules govern their design. The background of the ice class rules was investigated in a definition study (Huisman, 2015): Soininen's ice model and a time simulation of ice interaction served as the basis of the rules. Therefore, Soininen's model is considered in more detail in subsequent subsection. Furthermore, the ice class rules are briefly summarized.

2.4.1 Soininen's Ice Contact Model

Based on laboratory experiments and observation of failure processes, Soininen (1998) developed a physical model to estimate load levels during propeller-ice interaction. Different phases in the loading are distinguished as Soininen (1998, p.3) states: "*The blade leading edge opens cracks towards the groove formed by the previous blade… On the back side a spall is formed and the ice is crushed within the spall… The crushed ice is extruded towards both the leading edge and the trailing edge of the profile."* A time averaged, simplified pressure distribution was proposed, as given in Figure 2-8, which was eventually used in the simulation model (Koskinen et al., 1996).

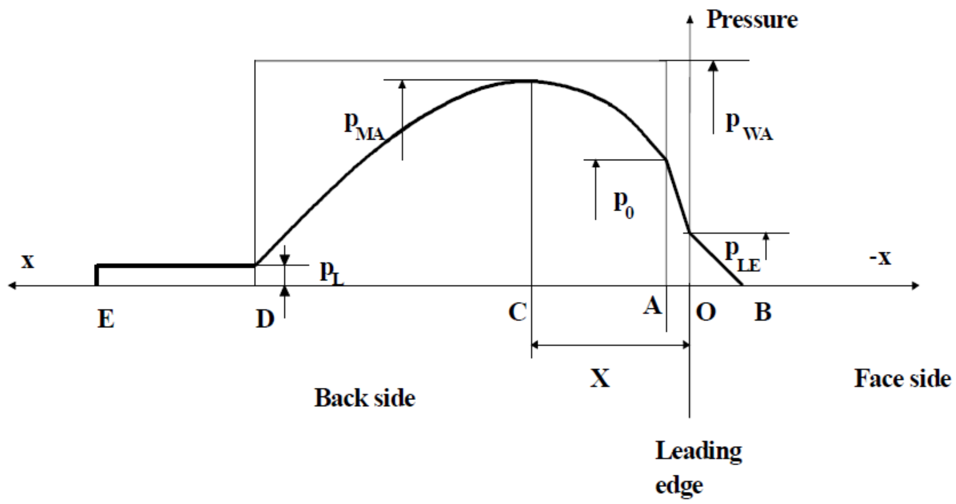

Figure 2-8: Idealized ice-load pressure distribution definition (after Soininen, 1998).

Figure 2-8 shows the pressure distribution over the outline of a propeller blade profile. Positive x denotes the back or suction side which impacts the ice, negative x gives the face or pressure side. The typical pressure points $\mathbf{E}, \mathbf{D}, \mathbf{A}, \mathbf{O}$ and $\mathbf{B}$ are defined in Figure 2-9. This figures shows a blade profile proceeding into the ice. Accompanying Figure 2-10 from Veitch (1995) sketches the physical processes. The following paragraphs define the pressure distribution in more detail.

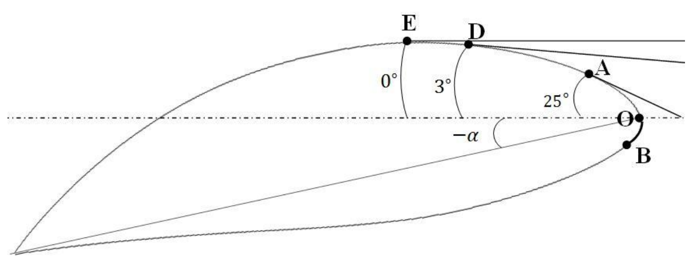

Figure 2-9: Definition of the typical pressure points in the ice-load pressure distribution according to Soininen (1998). The figure shows a blade profile under angle of attack α proceeding in the direction of the dotted line.

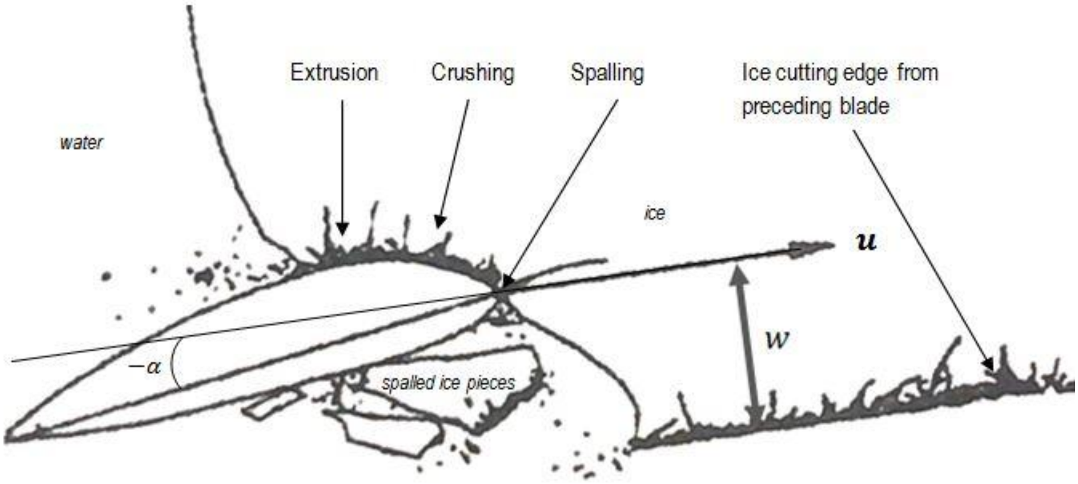

Figure 2-10: Sketch of a propeller blade profile proceeding into ice in direction (adapted from Veitch, 1995)

Point $\mathbf{B}$ is the location where the ice contact is lost on the pressure side. Single ice impacts from spalled ice pieces as sketched in Figure 2-10 are ignored since the ice is not confined at the pressure side. Loads will be negligible compared to the other loads. The location of point $\mathbf{B}$ is assumed to be proportional with cut width w in [m] according to

$$\mathbf{B}^* = 0.055w \tag{43}$$

in which $\mathbf{B}^*$ the length along the outline. Physically, the relation with cut width w represents the size of the spalls at the leading edge. Larger cut width w gives rise to larger spalls which impact the blade on a larger area. A linear loading distribution is assumed on $\mathbf{OB}$ from p_{LE} to zero. Point $\mathbf{O}$ denotes the leading edge of the blade while its pressure, p_{LE}, is defined as a total time averaged pressure on the leading edge which can be approximated by

$$p_{LE} = 4.5 + 26w \tag{44}$$

with cut width w in [m] and pressure in [MPa]. Above a critical stress state, the propeller blade can proceed into the ice. A tensile crack between the leading edge and the open ice edge is formed. The global load to open up these cracks into spalls is directly proportional to cut width w.

Cut width w depends on forward speed and rotational speed by

$$w = \frac{V}{nZ} \tag{45}$$

in which V ship speed, n rotational speed of the propeller and Z the number of propeller blades. Effectively, cut width w is the ratio between forward speed and the time between successive impacts from each propeller blade in the ice. Slowly rotating, highly pitched propellers at high advance speed may feature large cut width. The pressure at the leading edge is, however, limited to the maximum pressure p_{MA}.

Point $\mathbf{A}$ is located at the point where the angle between the local tangent along the blade profile outline and the angle of attack equals 25 degrees as visualized in Figure 2-9. This should represent the point on which the leading edge spalling behavior transitions into a crushing process with significant higher loading. The maximum time averaged value of the crushing pressure was found as

$$p_{MA} = 10\sigma_{ice}{}^{0.3} \text{ [MPa]} \tag{46}$$

during the laboratory experiments. It is assumed that the maximum pressure during the impact cycle p_{WA} relates to p_{MA} by

$$\frac{p_{MA}}{p_{WA}} = 0.9 \tag{47}$$

Soininen used p_{WA} and its ratio with the leading edge pressure p_{LE} to define the pressure in the transition point $\mathbf{A}$ according to

$$\frac{p_0}{p_{WA}} = 0.54 + 0.33\frac{p_{LE}}{p_{WA}} \tag{48}$$

The position of the maximum pressure, point $\mathbf{C}$, also depends on this ratio:

$$\frac{\mathbf{AC}}{\mathbf{AD}} = \left(1.18 - 0.018\frac{d}{\mathbf{AD}}\right)\left(0.55 - 0.41\frac{p_{LE}}{p_{WA}}\right) \tag{49}$$

where $\mathbf{AC}$ and $\mathbf{AD}$ denote the length in [m] in x-direction between the respective points. Also a dependency on the typical ice grain size $d = 0.005$ [m] is assumed.

Similarly to point $\mathbf{A}$, points $\mathbf{D}$ and $\mathbf{E}$ are defined for 3 and 0 degrees respectively as visualized in Figure 2-9. The pressure distribution on $\mathbf{AC}$ and $\mathbf{CD}$ is found from the quadratic distributions

$$p_{\mathbf{AC}} = p_{MA} - \frac{p_{MA}-p_0}{(X-AO)^2}(X-x)^2 \quad \text{[MPa]} \tag{50}$$

$$p_{\mathbf{CD}} = p_{MA} - \frac{p_{MA}-p_L}{(AD+AO-X)^2}(x-X)^2 \quad \text{[MPa]} \tag{51}$$

Between $\mathbf{D}$ and $\mathbf{E}$, forceful ice crushing is fully transitioned in extrusion. Crushed is extruded towards open water over the trailing edge. The confinement zone between $\mathbf{D}$ and $\mathbf{E}$ gives still significant loading. A constant time averaged pressure $p_L = 1$ [MPa] is assumed. After point $\mathbf{E}$ the extrusion is not confined anymore and the pressure cannot be maintained and is assumed to be zero.

The angle parameters in Soininen's model are defined with respect to the zero-angle of attack line. They define the shape of the pressure distribution. Physically, they represent the extent of the progressive crushing and extrusion processes. Refer to Huisman (2015), Soininen (1996) or Veitch (1995) for a detailed description of the ice failure processes on a propeller blade. Significant ice loads on the pressure side are limited to a small area at the leading edge as sketched in Figure 2-10 due to spalling of the ice. This sketch also clarifies that the extent of the load is limited to the point of maximum thickness for a given angle of attack. In Soininen's model, maximum pressure is a constant value due to brittleness of ice in combination with the high impact speeds of the propeller blades.

Referring to Huisman (2015) in which the ice-interaction process is described in more detail, Soininen's model only describes part of the complete ice-interaction process. Despite this, and all assumptions and simplifications, it is expected that the model will give valuable insight in the relation between geometry, ice loads and hydrodynamics at normal operation points within the first quadrant of propeller operation. It can be hypothesized that the blade shape and angle of attack will be the most important parameters. Since the location of the pressure distribution depends on the angle parameters, both the location of points $\mathbf{A}$, $\mathbf{D}$ and $\mathbf{E}$ and the angle of attack influence the pressure distribution.

The proposed pressure distribution is compatible with the propeller parameterization and can be implemented. Further details on the implementation are described in section 3.3.

2.4.2 Ice Class Rules

With reference to Huisman (2015), the general formulation of the ice class loads is

$$F = f(BAR, Z, H_{ice}, D, d, n) \tag{52}$$

for force F in which BAR the expanded blade area ratio, Z the number of blades, H_i the ice thickness which differs for each ice class, D the propeller diameter, d the hub diameter and n rotational speed. Coefficients are used to tune the forces with respect to angle of attack, ice strength and inertia effects. The force is considered as the maximum force which will be experienced during the lifetime of the ship. Two separate physical phenomena are taken into account.

The first is a load on the suction side which originates from milling loads which are described by Soininen's model, section 2.4.1. Regression analysis of the results of this model in a time simulation (Koskinen et al., 1996) produce the backward bending force in [kN]

$$F_b = 27\,(n \cdot D)^{0.7} \left(\frac{BAR}{Z}\right)^{0.3} D \cdot D_{l_b} \tag{53}$$

where $D_{l_b} = \max\{D, 0.85\,H_{ice}^{1.4}\}$ and $n = 0.85 n_{MCR}$ for a FPP. Here nD specifies the operation point in analogy with the angle of attack within Soininen's model while D_{l_b} represents the radial contact height with the ice. The other terms specify the ice contact area. Note that, besides contact area based on BAR, no propeller geometry dependency is present.

The second is a load on the pressure side although in reality the load is formed by suction due to ice-block proximity effects on the suction side. This hydrodynamic disturbance load is based on full-scale measurements and assumed to be reasonably represented by

$$F_f = 250 \frac{BAR}{Z} D \cdot D_{l_f} \tag{54}$$

with typical radial blockage factor D_{l_f} based on ice thickness and the exposed blade area:

$$D_{l_f} = \max\left\{D, \left(\frac{2H_{ice}}{1 - \frac{d}{D}}\right)\right\} \tag{55}$$

Note that F_f does not take, contrary to F_b, the propeller operation point into account. The severity of the suction due to blockage is assumed to be sufficiently captured with the constant factor in front of Equation (54).

Design loads F_b and F_f are applied on the propeller blade by means of load cases which should be considered in a Finite Element Method (FEM) stress analysis. The load cases are given as a uniform pressure applied on a certain area of the propeller blade. The total force should equal the maximum blade force F_b or F_f, uniformly applied on the area. The shaded area in Figure 2-11 should be considered for both backward and forward bending. In case of an FPP also the trailing edge should be loaded to account for operation in the third quadrant[17] with the left load case in Figure 2-11 on the pressure side[18] of the trailing edge. The load cases are summarized in Table 2-3.

[17] The four quadrants of propeller operation are assumed to be known. The third quadrant specifies backward rotation of the propeller while the ship also moves backward.

[18] Note that the face in backward operation becomes the back or suction side which experiences the highest loads as described in section 2.4.1.

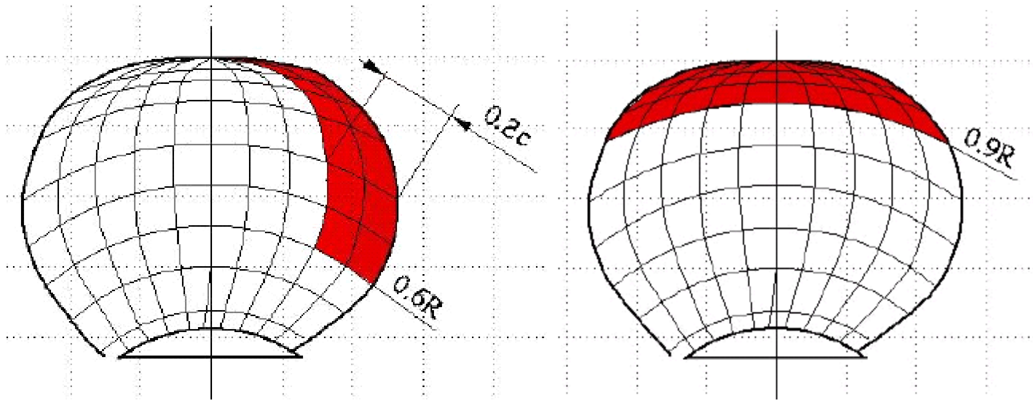

Figure 2-11: Load cases as defined by the ice class rules. The left case represents ice milling loads at the leading edge, while the right case accounts for tip impacts. R and c represent the dimensionless radial and chordwise length respectively.

Table 2-3: Summary of the ice-class load cases.

Load case	Force	Side	Area
1	F_b	Suction	Leading Edge
2	$0.5F_b$	Suction	Tip
3	F_f	Pressure	Leading Edge
4	$0.5F_f$	Pressure	Tip
5	$\max\{0.6F_f, 0.6F_b\}$	Pressure	Trailing Edge

2.5 Strength Analysis

As introduced in previous sections, the propeller should be analyzed for sufficient strength to withstand extreme ice loads as specified by the ice-class rules. Cantilever beam theory is inadequate for complex blade shapes[19]; class requires in-depth strength analysis.

2.5.1 Governing Equations

The governing equation of the strength analysis will be derived in this section with an emphasis on the involved assumptions[20]. The starting point is similar for fluid and solid mechanics. Conservation of linear momentum, Eq. (12), is valid for both. Contrary to inviscid fluids, both normal and shear stresses are present in solids. All nine components of stress which define the stress state of a material can be written in the Cauchy stress tensor $\boldsymbol{\sigma}$. Hence, surface forces $\int_{S(t)} F_\alpha^s \mathrm{d}S$ may be written as

$$\int_{S(t)} F_\alpha^s \mathrm{d}S = \int_{S(t)} \sigma_{\beta\alpha} n_i \mathrm{d}S = \int_{V(t)} \frac{\partial}{\partial x_\beta} \sigma_{\beta\alpha} \mathrm{d}V \tag{56}$$

by virtue of the divergence theorem. Substitution in the equation of motion yields

$$\int_{V(t)} \left[\frac{\partial \rho u_\alpha}{\partial t} + \frac{\partial}{\partial x_\beta}(\rho u_\alpha u_\beta)\right] \mathrm{d}V = \int_{V(t)} F_\alpha^b \mathrm{d}V + \int_{V(t)} \frac{\partial \sigma_{\beta\alpha}}{\partial x_\beta} \mathrm{d}V \tag{57}$$

It can be noted that this equation should hold at every instance in time such that, after rearrangement, this equation becomes Cauchy's first equation of motion[21]

[19] Classical cantilever beam theory to analyze propeller strength is explained in e.g. Kerwin & Hadler (2011).
[20] In-depth explanation of continuum mechanics is not given here. The reader is referred to Holzapfel (2000).
[21] Note that the subscripts α and β have been swapped. Considering the angular momentum equation (noting that local material elements should not be spinning) yields that the Cauchy stress tensor should be symmetric, i.e. $\sigma_{\alpha\beta} = \sigma_{\beta\alpha}$.

$$\frac{\partial \rho u_\alpha}{\partial t} = \frac{\partial}{\partial x_\beta}\left(\sigma_{\alpha\beta} - \rho u_\alpha u_\beta\right) + F_\alpha^b \tag{58}$$

Furthermore, static analysis is prescribed by the ice class rules, unsteady effects are assumed to be covered by the magnitude of the forces. Hence, neglecting the acceleration and convective term results in the governing balance equation

$$\frac{\partial}{\partial x_\beta}\sigma_{\alpha\beta} + F_\alpha^b = 0 \tag{59}$$

with six unknown stress components.

Constitutive Equations

The number of unknowns can be reduced by the both the kinematic relation between displacements and strains and the constitutive equations that relate the strains to stresses. Under the assumption of small deformations the kinematic relation can be linearized and written as

$$e_{\alpha\beta} = \frac{1}{2}\left(\frac{\partial s_\alpha}{\partial x_\beta} + \frac{\partial s_\beta}{\partial x_\alpha}\right) \tag{60}$$

in which displacement is denoted by s. This relation is known as the linearized Cauchy-Green strain tensor in which stretch and rotation are combined into strain.

The constitutive relation between stress and strain for linear elastic materials simplifies to

$$\sigma_{\alpha\beta} = E_{\alpha\beta\gamma\delta} e_{\gamma\delta} \tag{61}$$

in which $E_{\alpha\beta\gamma\delta}$ are elastic moduli and $e_{\gamma\delta}$ are strain components. Due to the isotropic-material assumption, the governing constitutive equation can be expressed as

$$e_{\alpha\beta} = \frac{(1+\nu)\sigma_{\alpha\beta}}{E} - \frac{\nu\sigma_{\gamma\gamma}\delta_{\alpha\beta}}{E} \tag{62}$$

in two independent material constants: Young's modulus E to describe elastic properties and Poisson's ratio ν to define contraction properties.

Substitution in the governing equation yields the partial differential equation

$$(\lambda + \xi)\frac{\partial^2 s_\beta}{\partial x_\alpha \partial x_\beta} + \xi\frac{\partial^2 s_\alpha}{\partial x_\gamma \partial x_\gamma} + F_\alpha^b = 0 \tag{63}$$

with constants $\xi = \frac{E}{2(1+\nu)}$ and $\lambda = \frac{2\xi\nu}{1-2\nu}$ to define the material properties. With proper boundary conditions this equation can be solved for displacement field s after which the stresses can be computed.

Boundary Conditions

At the hub the propeller blade is thought to be constrained for displacement and rotations such that $s_{hub} = s_{hub_0}$ on boundary S_{hub}. Furthermore, the pressure from the ice-class load cases is converted into external surface forces F^{ice} on boundary S_{ice} based on the area of each boundary element.

Weak Formulation

In order to solve Equation (63), however, a weak formulation should be constructed based on the principle of virtual work. A weak formulation is required for a numerical evaluation of the problem, in analogy with Equation (26) of the BEM. The partial differential equation is multiplied with a test function, a virtual displacement δv_α, and integrated over the domain to obtain the work done by the force components. Additionally, the external surface forces are added to the equation. Without giving the derivation this can be written as

$$\int_V E_{\alpha\beta\gamma\delta} \frac{\partial s_\gamma}{\partial x_\delta} \frac{\partial \delta v_\alpha}{\partial x_\beta} \, \mathrm{d}V - \int_V F_\alpha^b \delta v_\alpha \mathrm{d}V = \int_{S_{ice}} F_\alpha^{ice} \delta v_\alpha \mathrm{d}S \tag{64}$$

for all δv_α in V satisfying the displacement boundary conditions on S_{hub}.

2.5.2 Finite Element Method

Equation (64) can be solved for the unknown displacement s. Therefore, the displacement field is discretized into a set of n discrete nodes within the computational domain. Interpolation between the nodes gives the displacement field at an arbitrary position $\boldsymbol{x}$ within the domain. In general, the displacement field can be written as

$$s_\alpha(\boldsymbol{x}) = \sum_{i=1}^{n} N^i(\boldsymbol{x}) s_\alpha^i \tag{65}$$

where the interpolation functions N are a function of position only.

Substitution of interpolated displacement fields gives

$$\int_V E_{\alpha\beta\gamma\delta} \frac{\partial N^i}{\partial x_\delta} s_\gamma^i \frac{\partial N^j}{\partial x_\beta} \delta v_\alpha^j \, \mathrm{d}V - \int_V F_\alpha^b N^j \delta v_\alpha^j \, \mathrm{d}V = \int_{S_{ice}} F_\alpha^{ice} N^j \delta v_\alpha^j \mathrm{d}S \tag{66}$$

where the summation signs are omitted such that besides summation over α, β, γ and δ, also summation over i and j is required. Factoring out the virtual displacement δv_α^j and rewriting gives the following well-known equation of the Finite Element Method (FEM):

$$K_{\alpha\gamma} s_\gamma = F_\alpha \tag{67}$$

with $\boldsymbol{K} = K_{\alpha\gamma}$ the stiffness matrix

$$K_{\alpha\gamma} = \int_V E_{\alpha\beta\gamma\delta} \frac{\partial N^i}{\partial x_\delta} \frac{\partial N^j}{\partial x_\beta} \, \mathrm{d}V \tag{68}$$

and $\boldsymbol{f} = F_\alpha$ the force vector

$$F_\alpha = \int_V F_\alpha^b N^i \delta v_\alpha^i \, \mathrm{d}V + \int_{S_{ice}} F_\alpha^{ice} N^i \delta v_\alpha^i \mathrm{d}S \tag{69}$$

which is a system of n linear equations for the n nodal displacements.

The FEM allows to subdivide the structure into small building elements which are connected through their mutual nodes. Each element has it's stiffness, connectivity, geometry, applied loads and boundary conditions. It is possible to solve these individual element equations at once with Equation (67). Stiffness is a function of geometry, material and element type. Equation (67) states that displacement of the propeller blade under the action of a force is proportional to the constant stiffness of the structure. This equation can be solved for the nodal displacements s under the action of nodal forces F^{ice} and F^b and appropriate boundary conditions. The system is relatively small; a sparse matrix solver can be used.

If the displacement of the structure is known, the corresponding material strains can be calculated with Equation (60) after which Hooke's law gives the desired stresses by evaluating Equation (62). The von Mises yield criterion[22] is used to check for stresses that give rise to material yielding. Yielding implies permanent plastic deformation which should be avoided. Hence, material yielding is used as failure criterion. Each material has its own typical yield stress.

2.5.3 Element Choice

Crucial for any FEM is the element choice. Elements define the shape of the structure, describe its stiffness and distribute the nodal forces. Their polynomial functions $N(\boldsymbol{x})$ interpolate the deformation over each element. Elements may differ in geometry, degrees of freedom, the polynomial-order or integration technique. By connecting the elements, the deformation is interpolated over the entire structure.

For the analysis of a propeller blade, which is relatively thin, both shell and solid elements can be used. These elements use either linear or quadratic interpolation functions for displacements, however, shell elements are geometrically defined in two dimensions only. Thickness at the element nodes is prescribed externally, while solid elements feature a 3D geometry such that the elements describe the thickness directly. Shell elements work with the assumption that shear strains are linear over thickness which is valid for isotropic thin structures. Displacements in thickness direction are integrated by means of an integration method, e.g. Simpson's rule.

2.6 Numerical Uncertainty Analysis

Numerical uncertainty analyses can be used to choose the cheapest solution method while limiting numerical errors. A numerical uncertainty assessment is usually based on grid refinement studies of the discretized model, see Figure 2-1.

With reference to Eça et al. (2010) and the standard of the ASME (2009) , the aim is to estimate the numerical uncertainty U_{φ_i} of a certain solution φ_i for which the exact solution φ_{exact} is unknown. Numerical uncertainty analysis strives to estimate U_{φ_i} within 95% confidence:

$$\varphi_i - U_{\varphi_i} \leq \varphi_{exact} \leq \varphi_i + U_{\varphi_i} \tag{70}$$

The basis of the estimate lies in Richardson extrapolation, in this context defined as expanding φ_{exact} in a power series in which the coefficient is the typical grid-spacing h multiplied with an unknown factor α, i.e.

$$\varphi_{exact} \approx \varphi_i + \alpha {h_i}^p \tag{71}$$

Then it follows further for the discretisation error ϵ_ϕ and its estimate δ_{RE}

$$\epsilon_\phi \approx \delta_{RE} = \varphi_f - \varphi_0 = \alpha {h_i}^p \tag{72}$$

in which φ_0 is an estimate of φ_{exact} and p the order of convergence. At least four geometrically similar grids with their respective φ_i and h_i are required to obtain an acceptable fit. A least squares fitting procedure is used from which α and p follow, together with some translation factors. The fit value at h_i, φ_f, can be determined. Taking the limit for h to zero gives φ_0.

[22] This criterion gives an equivalent stress based on principal stress vectors. Only stresses which act to distort the structure matter when checking for yield. It is widely used for ductile materials in engineering applications.

Finally, in general, the numerical uncertainty can be composed of a safety factor c_{cf} and the standard deviation of the least square fits σ_f, like

$$U_{\varphi_i} = c_{cf}\delta_{RE} + \sigma_f + |\varphi_i - \varphi_f| \tag{73}$$

Also the absolute difference between the fit and calculated result is added. Depending on the order of convergence p, possible oscillatory or anomalous behavior, appropriate safety factors are applied.

A few requirements should be mentioned for the above theory. Although a constant grid refinement factor is not required, the grids should geometrically similar. In this context grid refinement is defined as

$$\frac{h_1}{h_i} = \frac{n_1 - 1}{n_i - 1} \quad \text{or} \quad \frac{h_1}{h_i} = \sqrt{\frac{N_1}{N_i}} \tag{74}$$

depending on grid refinement in one direction only with n cells in that direction or refinement in two directions with N the total number of grid cells. Subscript 1 denotes the finest grid during the analysis. Geometrically similar grids feature similar grid refinement ratios within the whole domain. Also, cell shapes, i.e., orthogonality, skewness, aspect ratio, etc. should remain similar. Furthermore, the approximation in Equation (72) should be reasonable accurate such that higher order terms are not required for the fitting. This requires that the solutions should behave asymptotically towards the exact solution, ideally, without fluctuations. If not, higher safety factors are applied.

Despite the prediction of the exact value, the uncertainty is the important result in the analysis. The predicted exact value is based on the fit and has its own, unknown, uncertainty. For all grids the uncertainty can be estimated with Equations (72) and (73).

Implementation

The implementation details of the numerical uncertainty prediction method are left outside the scope of this report, but can be found in Eça & Hoekstra (2014). A MARIN in-house tool incorporates the analysis. Its input is generated by a MATLAB function `tjh_gridUncertainty.m` created by the author which only requires φ_i and h_i to deliver U_{φ_i}. This function executes the uncertainty analysis tool and processes the output.

2.7 Optimization

Optimization is the process of determining the best solution to a certain problem. Or, as Papalambros & Wilde (2000) define: "improve the design so as to achieve the best way of satisfying the need, with all the available means". A formal definition of optimization is also given in this text: "The determination of values for design variables which minimize the objective, while satisfying all constraints". Optimization provides a systematic problem solving approach with minimal human interaction. It also provides insight in design problem characteristics, the underlying physics and their sensitivities and weaknesses.

2.7.1 Standard Formulation

Design variables $\boldsymbol{x} = (x_1, x_2, \dots, x_n)$, $\boldsymbol{x} \in X$ are variables by which the design problem is parameterized. The design space X is the set of all possible designs for which $\underline{\boldsymbol{x}} \leq \boldsymbol{x} \leq \overline{\boldsymbol{x}}$ where $\underline{\boldsymbol{x}}$ and $\overline{\boldsymbol{x}}$ are the lower and upper bound of the design variables respectively. Usually, an optimization problem is given in its Negative Null Form (NNF). An objective $f(\boldsymbol{x})$ is a quantity as function of the design variables that is to be optimized. Optimization is a minimization of the objective, $\min_{\mathrm{x}} f(\boldsymbol{x})$, in case of a NNF. A constraint is a condition that has to be satisfied. Inequality constraints $\boldsymbol{g}(\boldsymbol{x})$ or equality constraints $\boldsymbol{h}(\boldsymbol{x})$ should be defined for a NNF such that $\boldsymbol{g}(\boldsymbol{x}) \leq 0$ and $\boldsymbol{h}(\boldsymbol{x}) = 0$.

Typically, an optimization problem consists of an iterative procedure with a model and a optimization algorithm like indicated in Figure 2-12a. An optimal solution should be achieved using the smallest number of function evaluations.

2.7.2 Multi-Objective Optimization

Multi-objective optimization problems, with objective vector $\boldsymbol{c}(\boldsymbol{x})$ where $\boldsymbol{c} = (c_1, c_2, \ldots, c_m)$, are often used to quantify design trade-offs. A possible design space is given in Figure 2-12b. Pareto points are points on the Pareto set or Pareto front for which "no other feasible point exists that has smaller c_i without having a larger c_j" as Papalambros & Wilde (2000) define. There is no improvement of an objective possible without worsening another objective. A propeller designer should balance the design and pick a propeller on the Pareto front based on the design requirements and practical application.

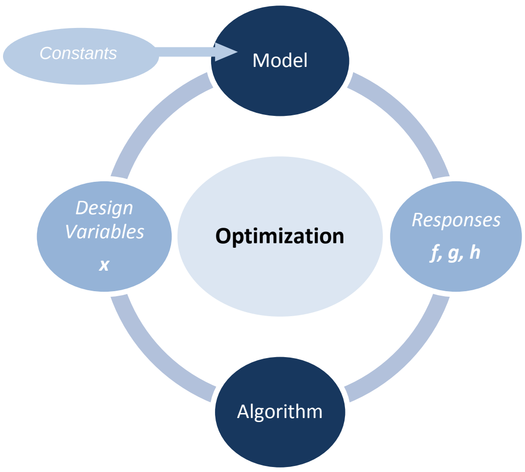

Figure 2-12a: Iterative optimization cycle

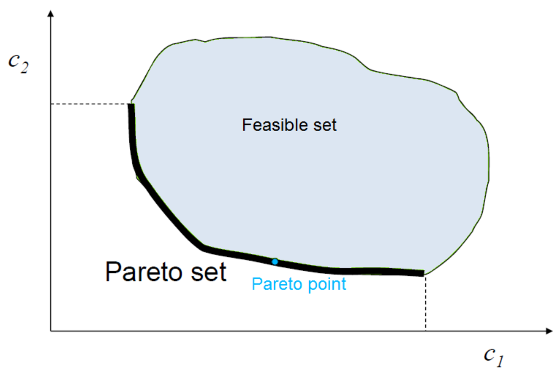

Figure 2-12b: Visualisation of a Pareto set

2.7.3 Genetic Algorithm

A Genetic Algorithm (GA) is inspired from biological processes. A genetic algorithm can be compared with evolutionary spawning or breeding. The algorithm makes use of a generation with a certain propeller population, a collection of propellers, which is subjected to a fitness function. Based on fitness parents are selected for reproduction, crossover and mutation. Higher fitness gives higher probability to stay within the population and share geometrical information with others.

A fitness function incorporates the objectives and constraints. Fitness is also function of the location of the propeller within the objective space. Pareto-front propellers get higher fitness than propellers which are dominated by the Pareto-front propellers. Although propellers on the Pareto-front are non-dominated, further distinction is made by the propeller crowding. Fitness is assigned such that the propellers will be distributed along the fronts without clustering.

Design parameters are discretized in binary strings[23], comparable with the chromosome structure in biology. Hence, discrete variables may easily be included. The used algorithm within this Master's thesis, the Non-dominated Sorting Genetic Algorithm II (NSGAII), uses analytical alternatives instead, based on probability density functions to avoid the discretisation errors (Deb et al., 2002).

[23] In the binary number system, any number may be represented as the sum of powers of two. Real valued numbers are to be discretized, often exact representation is not possible.

A first generation with a certain population size is randomly generated using a uniform distribution within the prescribed bounds of the design parameters to cover the design space. Better coverage and results are obtained with a larger population size, at the cost of longer computational time.

The four steps of the algorithm for a certain generation G_i are summarized in the enumeration below.

1. **Tournament.** The population within G_i is subjected to a tournament. The tournament gives a further probability-based selection of propellers for reproduction, the parents P_t within the population. The weakest propellers within G_i are rejected and the fittest are prioritized. A random pair of propellers is picked from G_i of which fittest propeller selected and the weakest is both rejected for reproduction and sidelined in the tournament. Hence, fittest propellers may occur multiple times within the parent population while weaker propellers have the chance to also be chosen.
2. **Offspring**. An offspring, the child population, is created from parents P_t. The principles to create an offspring are based on crossover and mutation of the binary strings of the parent propellers. Crossover shares random binary code between parent and child propellers while mutation randomly flips bits in the binary strings. Crossover ensures that child propellers will inherit the best properties of the parent propellers. Mutation, in addition, searches within the design space to overlook local optima and explore new designs towards the global optimum. Choices for the number of parameters to be subjected to crossover and mutation and their probability to occur are algorithm-specific. Details for the NSGAII can be found in Deb et al. (2002). Details of Simulated Binary Crossover (SBX) to simulate binary crossover with continuous variables are discussed in Deb and Agrawal (1995).
3. **Fitness.** The propellers within the child population are computed for their performance in terms of feasibility, hydrodynamics and strength. The fitness function is evaluated together with the constraints.
4. **Sorting.** The child population is added to the original population. The fittest half of this population forms the new generation G_{i+1}. The other half will extinct.

Note that the algorithm starts with step three for the first generation. The algorithm keeps running until the last generation has been evaluated and sorted. Either the number of generations is prescribed or convergence properties determine the stopping criterion.

The algorithm is based on randomness and probabilities, both within the tournament and creation of offspring. Since no information on gradients is required, highly scattered, discontinuous and non-differentiable objective functions are allowed. Although computationally expensive compared to higher order methods, the algorithm is versatile and overlooks local optima. In addition, the population can easily be computed in parallel.

Nuland (2014) did extensive research in the properties and settings of the NSGAII for a propeller study. His conclusions are utilized in this Master's thesis, although primary focus is on propeller design instead of algorithm performance. Algorithm test cases from Srinivas & Deb (1994) have been reproduced by Foeth (2014) which verifies the NSGAII version that is used in this Master's Thesis.

3 COMPUTATIONAL METHODS

Having explained the physical and theoretical models in the previous chapter, computational methods to solve these models are considered in the current chapter. The computational methods are assessed on their validity, uncertainty and best practice settings.

This chapter is organized as follows:

1. First, section 3.1 considers hydrodynamic Boundary Element Method PROCAL. Its capabilities will be assessed in a grid refinement study and numerical uncertainty estimations. A procedure to iterate for mean thrust will be explained as well. This section is finished with open water validation computations and a self-propulsion test case.
2. Second, in section 3.2 different implementations of the Finite Element Method are developed and compared to a reference computation for one ice-class load case. Numerical uncertainty studies show that a linear shell element implementation will be a good choice within an optimization.
3. Third, section 3.3 assesses and develops the ice-load model based on an idealized simplified ice pressure distribution. First the sensitivities in 2D will be shown after which the implementation of a steady 3D model is presented.
4. Last, section 3.4 combines the geometry generation procedure and the optimization algorithm together with the analysis tools into a computational optimization framework.

3.1 Boundary Element Method

The theory as explained in section 2.2 is implemented in Marin's in-house BEM PROCAL. Details on its implementation are reported by Bosschers (2009, 2014). PROCAL is widely used at MARIN and within the industry. Validation and benchmark computations have been reported internally at MARIN and published by i.e. Vaz & Bosschers (2006) and Bosschers et al. (2008).

The goal of this section is to assess the capabilities of PROCAL as hydrodynamic analysis tool within an optimization. The following will be considered:

- Numerical uncertainty should be as low as possible when comparing different propellers on geometrical details. This will be the topic of the first subsection 3.1.1 which considers the reference propeller from the case study, section 1.5, as basis.
- Different propellers should be predicted with similar numerical uncertainty which requires, beside a check afterwards, an assessment of grid layout and spacing. This will be covered in subsection 3.1.2.
- As already mentioned in the introduction, propeller pitch needs to be corrected to obtain the required design point thrust. Besides an explanation of this method, an analysis is carried out to assess the sensitivity of efficiency to the design point in subsection 3.1.3. Combined with the numerical uncertainty and the physical relation with thrust and torque, a final uncertainty for efficiency will be assumed.
- Although PROCAL is validated extensively and confidence in computational settings has been obtained with previous subsections, a short comparison of the open water data and the self propulsion model tests is performed to touch upon the relative differences between experimental and computational results in subsection 3.1.4.

3.1.1 Grid Refinement Study

A grid refinement study is carried out to estimate numerical uncertainty of different computational grids. In addition, a study into the grid distribution is performed to check the grid dependency. Steady computations with the reference propeller in open water conditions serve as basis. Note that different propeller geometry or design points could give different results. However, as indication for the best practice grid settings during an optimization this analysis is deemed to be sufficient.

Extensive grid refinement studies for PROCAL have already been performed in e.g. Boorsma (2005) in which it is shown that a grid of 30 to 40 panels chordwise direction and 20 to 30 panels in radial direction is sufficient for conventional propellers. Numerical uncertainty and grid details, however, are not addressed in detail.

Therefore, a grid refinement study is carried out in which the number of panels is varied. Following Boorsma (2005), the difference between the number of panels in radial and chordwise direction equals 10. Figure 3-1 shows the results for K_T and K_Q. Table 3-1, in addition, presents the numerical uncertainty for efficiency.

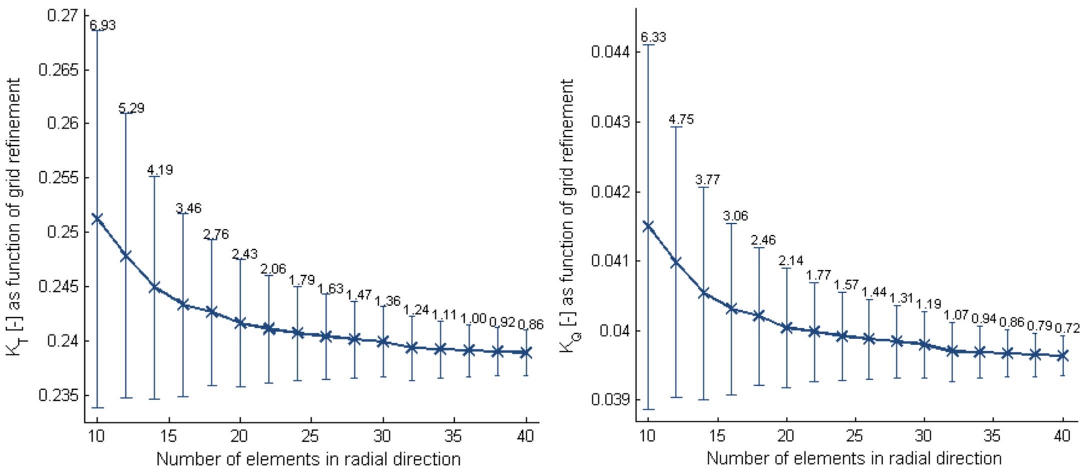

Figure 3-1: Grid refinement study results for K_T and K_Q. The bars give the numerical uncertainty, also presented by the values in percentages. The number of elements in chordwise position is ten more than in radial direction.

Table 3-1: Uncertainty percentages for K_T, K_Q and η. Assuming independent variables, an uncertainty U_{η^*} is obtained for the efficiency. The number of elements is given in radial x chordwise direction.

	Steady				Unsteady			
Elements	U_{K_T} [%]	U_{K_Q} [%]	U_{η^*} [%]	U_η [%]	U_{K_T} [%]	U_{K_Q} [%]	U_{η^*} [%]	$U_{\delta T}$ [%]
10x20	6.93	6.33	0.690	14.16	6.83	6.58	0.92	13.85
14x24	4.19	3.77	0.380	8.27	3.93	3.77	0.57	8.34
18x28	2.76	2.46	0.210	5.35	2.57	2.44	0.38	5.76
22x32	2.06	1.77	0.140	3.90	1.82	1.72	0.27	3.96
26x36	***1.63***	***1.44***	***0.120***	***3.11***	***1.45***	***1.37***	***0.25***	***3.09***
30x40	1.36	1.19	0.100	2.58	1.15	1.12	0.25	2.44
34x44	1.11	0.94	0.0800	2.07	0.93	0.88	0.21	2.05
38x48	0.92	0.79	0.0600	1.72	0.75	0.74	0.15	1.79

Numerical uncertainty for η could be based on a similar method assuming independent variables, which yields that the predicted numerical uncertainty U_{η^*} is an order smaller than the uncertainty for K_T and K_Q. Physically, however, η is defined as

$$\eta = \frac{K_T}{K_Q}\frac{J}{2\pi} \tag{75}$$

which implies that the uncertainty of η incorporates the uncertainty of K_T and K_Q. Considering both the upper and lower bound of η yields uncertainty U_η as

$$U_\eta = \left(\frac{(1 \pm U_{K_T})K_T}{\left(1 \mp U_{K_Q}\right)K_Q} - \frac{K_T}{K_Q}\right)\frac{K_Q}{K_T} = \frac{U_{K_T} + U_{K_Q}}{1 \pm U_{K_Q}} = \frac{U_{K_T} + U_{K_Q}}{1 - U_{K_Q}} \tag{76}$$

which is also represented in Table 3-1. This physically more justified uncertainty for η yields much higher uncertainty values than assuming η independent from K_T and K_Q.

Acceptable Numerical Uncertainty of Efficiency for Optimization

A numerical uncertainty of 3.11% is predicted for η when using a grid of 26x36 elements in radial and chordwise direction. For optimization purposes this uncertainty is hardly acceptable since relatively small efficiency gains are obtained in the order of few percents only.

If one would only be interested in the prediction of η, it could be argued that its numerical prediction for uncertainty, the much lower U_{η^*}, could also be accepted. However, within an optimization also thrust should be predicted accurately to repitch the propellers towards the design point. For instance, the grid of 26x36 elements in radial and chordwise direction predicts thrust with 95% confidence with 1.63% uncertainty. This could be acceptable if

- the bias between experimental and computational results for thrust is greater or equal than their uncertainty and
- the sensitivity of efficiency to the design point is less or equal to U_{η^*}.

which will be considered in the next subsections.

Numerical Uncertainty in Unsteady Computations

The grid refinement procedure was repeated for unsteady computations, taking the interaction with the wake field into account. These results are also given in Table 3-1. Numerical uncertainty for efficiency and the mean thrust and torque proved to be 10% lower on average compared to steady computations. The uncertainty for thrust variation $U_{\delta T}$, however, is predicted as 3.09% while it should be noted that the wake field resolution is not varied.

For thrust variation it might be argued that the uncertainty is acceptable, since the thrust variation objective is also only an estimate of the interaction with the wake field. Detailed noise, vibration and cavitation analyses should be carried out to validate the validity of the thrust variation criterion.

Neither grid refinement nor numerical uncertainty studies in combination with cavitation have been performed in this Master's thesis. Nuland (2014), however, shows that the cavitation extent is highly grid dependent. The reference mesh of 26x36 elements in radial and chordwise direction will not suffice. For a balance between accuracy and computational time a grid of 40x50 elements in radial and chordwise direction will be used for cavitation computations.

3.1.2 Grid Dependency

No considerations on the shape and details of the grid have been made so far. Grid dependency on the relative spacing and shape of the elements may have significant influence. Ideally, the least grid dependency is desired since a range of geometries is to be considered within an optimization.

A hyperbolic tangent is used to distribute the grid over the radius and chord outlines. The weight factors of the tangent are referred to as grid spacing. Higher weight factors give larger spacing. The grid spacing at the trailing edge, leading edge, hub and tip is varied for which the results are given in Figure 3-2 in percentages with respect to a reference grid of 26 x 36 elements in radial and chordwise direction. For the sake of imagination, Figure 3-3 presents three typical computational grids of 26x36 elements in radial and chordwise direction with different grid distributions.

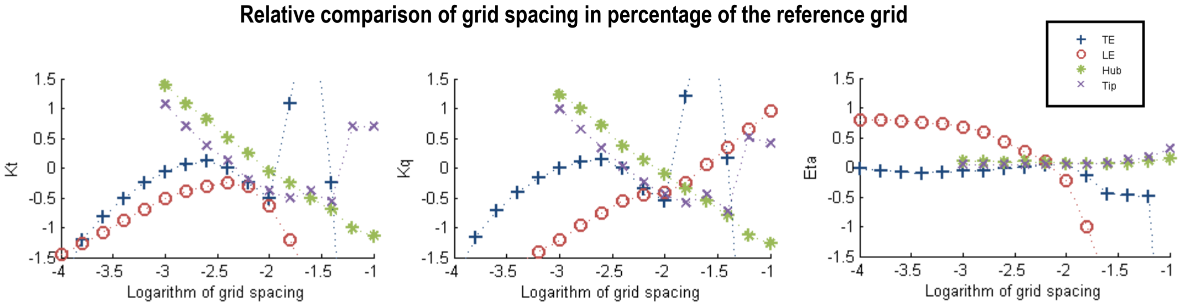

Figure 3-2: Variation of the grid spacing (10log) for the trailing edge (TE), leading edge (LE) and both (LE & TE). Also the spacing in the hub and tip region is varied. The reference grid with 26x36 panels in radial and chordwise direction serves as basis. K_T, K_Q and η are given in percentages with respect to the reference grid.

The reference grid features the spacing for the trailing edge (TE), leading edge (LE), hub and tip as the respective logarithmic values of -2.15, -2.15, -1.70 and -2.0.

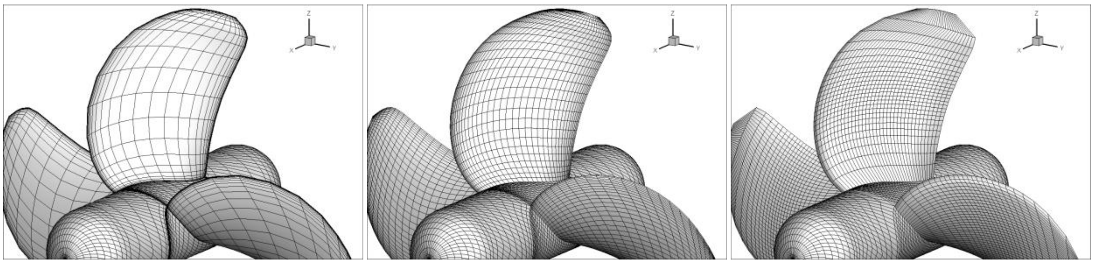

Figure 3-3: Typical computational grids with different spacings. The left presents a case with extreme refinement at the edges representing the left side of Figure 3-2, the middle figure shows the reference grid and the right picture shows a typical grid for the right side of Figure 3-2.

For smaller spacing, less panels are located in the midsection for which results will be computed less detailed. However, the refined region is described more accurate. The resulting pressure is predicted with higher resolution. Also, when the leading edge is refined more, effectively, the trailing edge will become less refined. These balances are presented in Figure 3-2. The following observations and notes should be made concerning this figure:

- Hub spacing can be chosen large such that the grid is uniformly spaced
- Tip spacing can be chosen as large as a logarithmic spacing of around -1.75. Above that, the grid would resemble the right grid of Figure 3-3 which does not capture the tip geometry correctly.
- Both the leading edge and trailing edge need both to be refined below a logarithmic spacing of -2.0. Above that, numerical errors are introduced at the trailing edge or geometry is not captured accurate enough at the leading edge.

This analysis shows that the edges should be refined, while the midsection and hub may remain relatively coarse. Note that the reference grid spacing is well chosen[24]: the spacing is outside the diverging or alternating trends. Hence, the reference grid settings can be used for future optimization. It is assumed that other propeller geometries behave similarly to the reference propeller.

3.1.3 Propeller Design Point

The goal of this section is twofold:

1. Explanation of the pitch correction routine to obtain the design point thrust for each propeller geometry.
2. Investigation of the sensitivity of efficiency on the design point.

[24] The grid refinement study in section 3.1.1 and this study have been iterated to choose a reference grid that performs well: the grid refinement study is carried out with the best practice spacings from Figure 3-2.

Pitch Correction Routine

Although an equality constraint on thrust could be prescribed within an optimization algorithm, thrust is adjusted within a separate routine. After a propeller geometry has been generated, a steady BEM computation delivers its thrust. Mean pitch is iteratively adapted to meet the required thrust in the design point. Convergence is typically fast with only three to four iterations to obtain thrust within 0.1% accuracy at the design point.

Steady hydrodynamic computations are used to save computational time. This assumption will be checked in the optimization results, since the converged propeller is subjected to an unsteady computation after convergence to analyze the thrust variations.

A first estimate of the difference in thrust is based on the Wageningen B-series polynomials (Oosterveld & Oossanen, 1975) which requires pitch, number of blades, advance ratio and BAR to obtain thrust coefficients. After this estimate a linear interpolation and a quadratic interpolation are used. Typically, convergence within 0.1% of the design point thrust is reached by then. Sometimes, a fourth iteration is required for fine-tuning. Linear interpolation suffices, otherwise the propeller is marked as diverged.

Efficiency Sensitivity on the Design Point

Considering the numerical uncertainty U_T = 1.63% for the thrust prediction with steady computations and the numerical uncertainty for efficiency of U_{η^*} = 0.12% it should be studied how the influence of the thrust uncertainty is reflected in efficiency through the design point. The reference propeller is iterated to the design thrust T = 271 $\pm$ 4.4 [kN]. It appears that the efficiency is predicted as 0.6445 $\pm$ 0.0022 or 0.34%. Hence, the influence of the design point on efficiency is larger than its numerical uncertainty. Table 3-2 shows the analysis. Efficiency is calculated for three design points. While the numerical uncertainty for efficiency is taken into account, the efficiency difference for the three design points can be calculated.

Table 3-2: Sensitivity of efficiency on the design point.

Thrust [kN]	Efficiency	Efficiency with U_{η^*}	Percentage
266.6	0.6467	0.6475	0.465%
271.0	0.6445		
275.4	0.6423	0.6415	-0.465%

Concluding Remark

It might be argued, that for the reference propeller with a grid of 26x36 elements in radial and chordwise direction, efficiency can be predicted with an uncertainty of 0.47% within 95% confidence instead of the more justified prediction of uncertainty of 3.11%.

3.1.4 Validation Computations

Considering the case study, both open water results as self-propulsion tests are available which can be used to assess the validity of PROCAL. First the open water results will be compared, after which the self-propulsion tests will be computed, with a steady and unsteady computation.

Open Water Tests

Validation studies have been performed at MARIN by comparing PROCAL open water computations with model test results. Figure 3-4 repeats this study for the reference propeller of the 'Streamline' case study. Solid lines represent open water model experiment results as given by Di Felice (2011) as polynomial expressions. Markers represent PROCAL results. Grids were generated according to the gridding guidelines by Boorsma (2005). Figure 3-4 gives no notion on experimental uncertainty. Experience, however, learns that 2 to 3 percent is generally accepted.

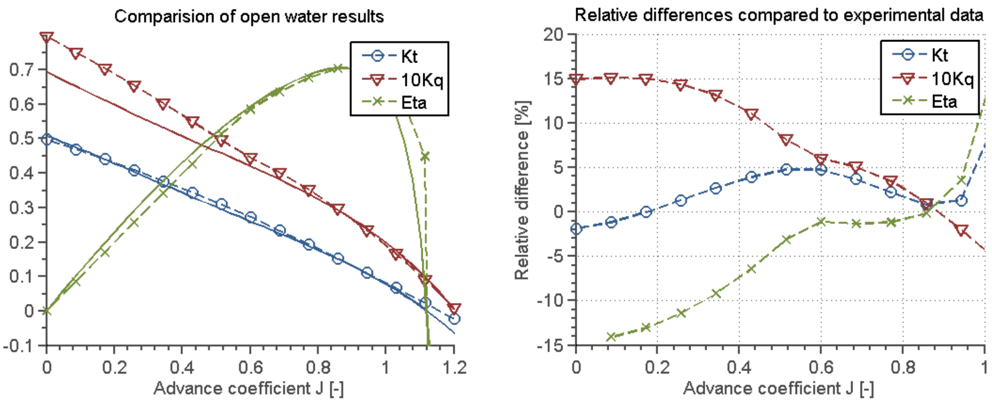

Figure 3-4: Comparison of open water results for the reference propeller.

Typical relative differences are around 3 to 5 percent at the design point J = 0.676. Without further investigation, for heavy loaded conditions outside the design point, K_Q and η deviate up to 15%. The assumptions for the wake modeling might not be valid here while flow separation in combination with viscosity might play a role in reality.

Although this compares well with earlier studies at MARIN, these studies also showed that the relative differences depend on propeller geometry. While this will be a recommendation for further study, in this Master's thesis it is assumed that optimized propellers with significant different geometry feature similar relative differences with respect to experimental model tests as the reference propeller.

Self Propulsion Tests

Self propulsion model tests have also been performed for the case study on the 'Streamline' tanker. They form the basis of the definition of the design point as given in the introduction, section 1.5. Taking the effective wake field in steady and unsteady computations with BEM PROCAL would give an indication of the combined effect of the errors within geometry modelling, experiment measurements and the computational method.

This comparison is given in Table 3-3 and its accompanying figure of the relative differences. It is shown that the thrust of the original, non-pitch-corrected propeller deviates from the design point with -3.1 $\pm$ 1.63 [%] for steady computations and -2.3 $\pm$ 1.45 [%] for unsteady computations taking the numerical uncertainty into account.

Table 3-3: Comparison between experimental model test results, steady BEM computations and unsteady BEM computations

	Thrust [kN]	Power [kW]	K_T [-]	K_Q [-]	η [-]
Experiment	271.0	2367	0.248	0.0406	0.657
Steady	262.8	2323	0.240	0.0399	0.649
Unsteady	264.8	2349	0.242	0.0403	0.648

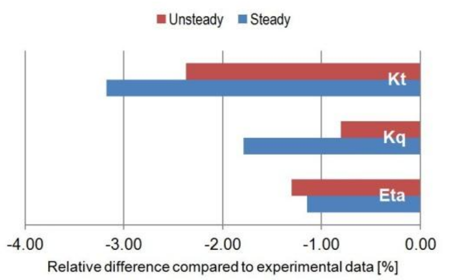

This analysis shows that, although numerical uncertainty might be acceptable, optimization results should be compared with experimental results or full scale data to check whether the optimization resulted in physical improvements, rather than numerical artefacts.

3.2 Finite Element Method

Similar to any propeller, an ice-class propeller should be strong enough to withstand its lifetime loads. Ice-class rules specify the maximum lifetime loads in five load cases. If the propeller would be too strong, efficiency will be compromised. Damage will occur when the propeller is too weak. A FEM should predict the load carrying capacity of the propeller with sufficient accuracy. Taking the margins of safety within the ice-class loads into account, maximum stresses can be compared with the allowable stress.

Preferably, the propeller geometry is meshed with unstructured solid elements with sufficient resolution in thickness including the connection of the hub to include all geometric details. The procedure as indicated by Valtonen (2015) at Aker Arctic should be followed. Unstructured meshing requires a solid model of the propeller blade. Due to geometry singularities in the tip region this process is not yet automated and requires considerable manual effort and 3D modeling skills. Therefore, this method is not suitable for automated optimization. However, it suits to check the results of other methods.

Hence, four implementations of the FEM are considered in subsequent subsections:

1. An unstructured dense solid mesh with tetrahedral elements is created to serve as reference for the three other implementations.
2. To compare, an unstructured sweep mesh with hexahedral elements is considered. It allows a check of the effect of element shape and the influence of the number of elements in thickness direction can be analysed.
3. To avoid the manual creation of a solid of the propeller geometry, a structured mesh can be used. A structured mesh with solid hexahedral elements is assessed for its performance.
4. Considering the drawbacks of structured solid modeling, a FEM implementation with structured shell elements is assessed as well.

For each implementation numerical uncertainty is assessed if possible and necessary. This section closes with conclusions and recommendations on the preferable method to be used in an optimization.

The ANSYS workbench environment is used for the preprocessing of unstructured meshes, while the MATLAB programming environment is used as preprocessor with the user-defined function `tjh_prep4ansys.m` and its supporting underlying functions for the structured meshes. All four implementations are solved in batch with ANSYS Mechanical APDL. Details on the implementation of the elements and solver can be found in the theory reference by ANSYS (2013).

3.2.1 Unstructured Tetrahedral Solid Elements

Meshing is based on a free meshing method[25] with tetrahedrons. A typical cell size can be prescribed. Pressure is directly applied on the element boundaries by means of interpolation. The root fillet and hub are not modeled, although this method allows full modeling of any propeller geometry details.

A mesh refinement study with six different meshes is performed to check whether the finest mesh is refined enough to serve as reference for less computational expensive methods. Only one load case from the ice-class rules, load case five with load on the trailing edge as described in Figure 2-11, is considered for this study . This load case is the most severe one for the reference propeller.

Comparison of different meshes is based on maximum stress. Figure 3-5 gives an overview of the stress contours and the mesh outline, while Table 3-4 summarizes the results quantitatively.

[25] ANSYS Workbench 15.0 was used. Details can be found in ANSYS (2015).

Table 3-4: Summary of solid model stress results

Typical element size [m]	0.00625	0.0125	0.025	0.05	0.1	0.2
Number of elements	563589	154618	44285	9662	1996	70
Probe stress [MPa]	3.167E+08	3.165E+08	3.183E+08	3.228E+08	3.192E+08	2.472E+08

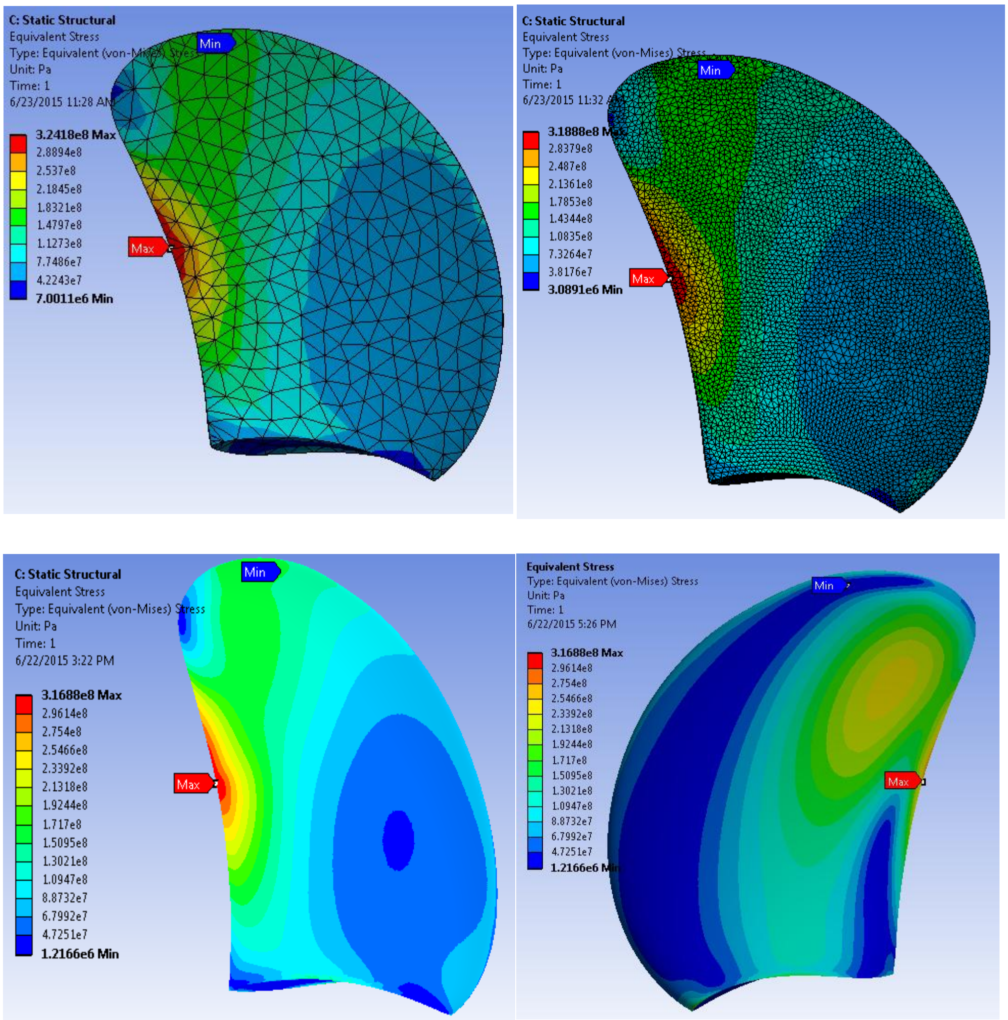

Figure 3-5: Stress contours [Pa] on the reference propeller for unstructured triangulations with different mesh density. The results for load case five of the ice-class rules are presented. Top left is a mesh with 2.00e3 elements, top right with 9.66e3 elements and bottom the results of the mesh with 5.64e5 elements with the pressure side in the left and the suction side in the right picture.

Qualitatively, all meshes capture the stress distribution in the propeller material. The four finest meshes have been used to estimate the numerical uncertainty as presented in Figure 3-6. The two coarsest meshes are not in the asymptotic range which are not used in the estimation of numerical uncertainty. The relative numerical uncertainty of 0.70% is acceptable for the finest mesh to be used as reference for other FEM implementations. In conclusion, the reference value of stress for load case five can be given as $\sigma_5 = 316.7 \pm 2.2$ [MPa].

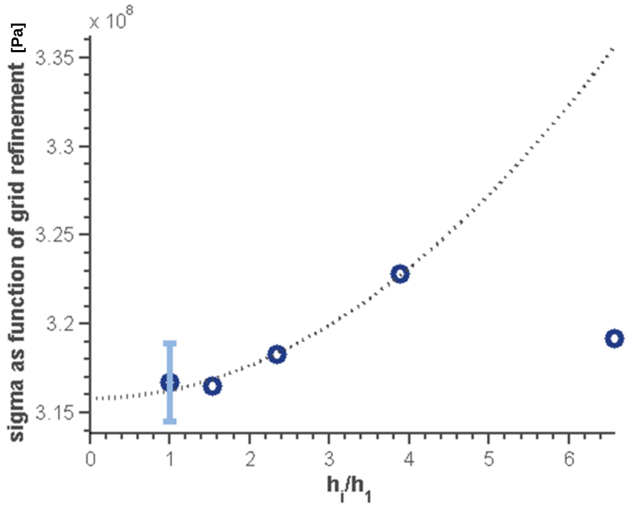

Figure 3-6: Numerical uncertainty analysis for results within the asymptotic range according to maximum stresses sigma. The horizontal axis which indicates the refinement level with respect to the finest mesh is defined as in Equation (74).The errorbar gives the uncertainty of 0.70% for the finest mesh.

3.2.2 Unstructured Hexahedron Solid Elements

Also hexahedron swept meshes were analyzed in which the number of elements in thickness can be varied while keeping the mesh constant. Similar results were obtained for the maximum stresses, i.e., the maximum stress approaches the reference value for load case five σ_5 with mesh refinement. Figure 3-7 shows that also for the coarser meshes the distribution of stresses compares well with Figure 3-5.

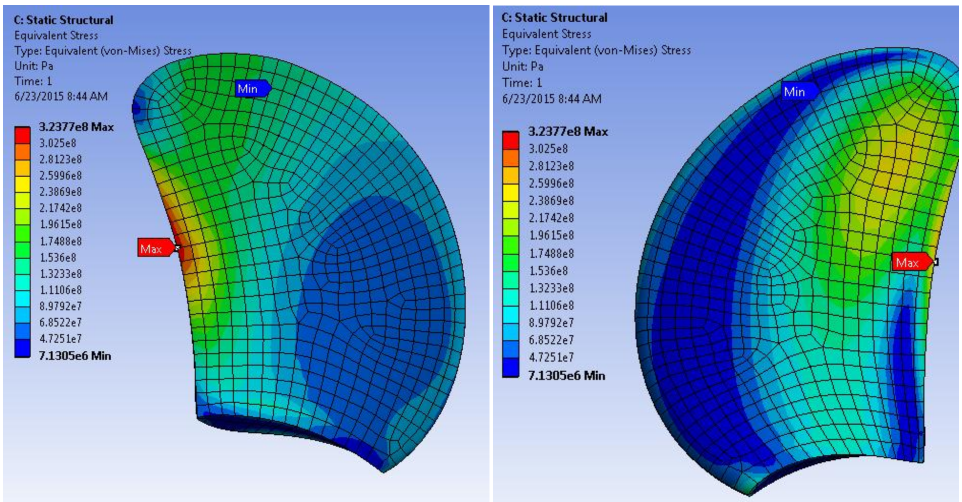

Figure 3-7: Stress levels in [Pa] of the reference propeller based on a coarse sweep mesh with hexahedrons for load case five of the ice-class rules.

The swept meshes allow an assessment of the influence of the number of elements in thickness of the propeller blade. The coarse mesh of Figure 3-7 was used as basis in the comparison[26]. Only the element type and number of elements in thickness was adjusted. It is expected that shear locking[27] is avoided by using elements with quadratic interpolation functions which use mid-side nodes.

Table 3-5 gives an overview of the results. It shows that one quadratic element over the thickness would suffice for a swept mesh: there is no difference when using one or two elements in thickness direction. Linear elements, however, require more than four elements

[26] A coarse mesh is used to shorten computational time. This analysis requires significant user interaction, while also the meshing time can be significant for finer meshes.

[27] Shear locking is a numerical error that occurs in FEM when using linear elements. Linear elements do not accurately model the material curvature under bending; an artificial shear stress is introduced.

in thickness direction to converge towards the reference stress value. Since the additional computational time for using quadratic elements diminishes with the required meshing time by using multiple elements in thickness, quadratic solid elements should be used to analyze propellers.

Table 3-5: Comparison of results with or without mid-side element nodes

Mid-side nodes	# elements in thickness	# elements	σ_{max} / 10^8 [MPa]
Yes	1	3046	3.237
No	1	3046	3.323
Yes	2	6092	3.236
No	2	6092	3.281
No	4	11900	3.258

Besides the notion that the stress levels are apparently similar for tetrahedron and hexahedron shaped elements, no further analysis is deemed necessary in the context of this work. Although the load cases can be implemented more accurately, the effort to obtain the solid model of the propeller outweighs the benefits. Hence, an automated and faster method is to be used which also predicts the correct stress levels.

3.2.3 Structured Solid Elements

A structured solid element implementation was supplied as starting point[28] with two quadratic elements in thickness. Referring to Table 3-5, two quadratic elements are sufficient. Although the results compare well qualitatively comparing Figure 3-5 and Figure 3-8, quantitatively the method is not suitable for optimization purposes. Besides the significant larger preprocessing time[29], unphysical stress concentrations in the tip region are present due to poorly shaped brick elements which do not vanish with mesh refinement. The red oval in Figure 3-8 indicates the incorrect position of maximum stress. The actual value of maximum stress of 3.26e8 [MPa] compares reasonably well with both its magnitude and location with previous results, which justifies its use as qualitative method.

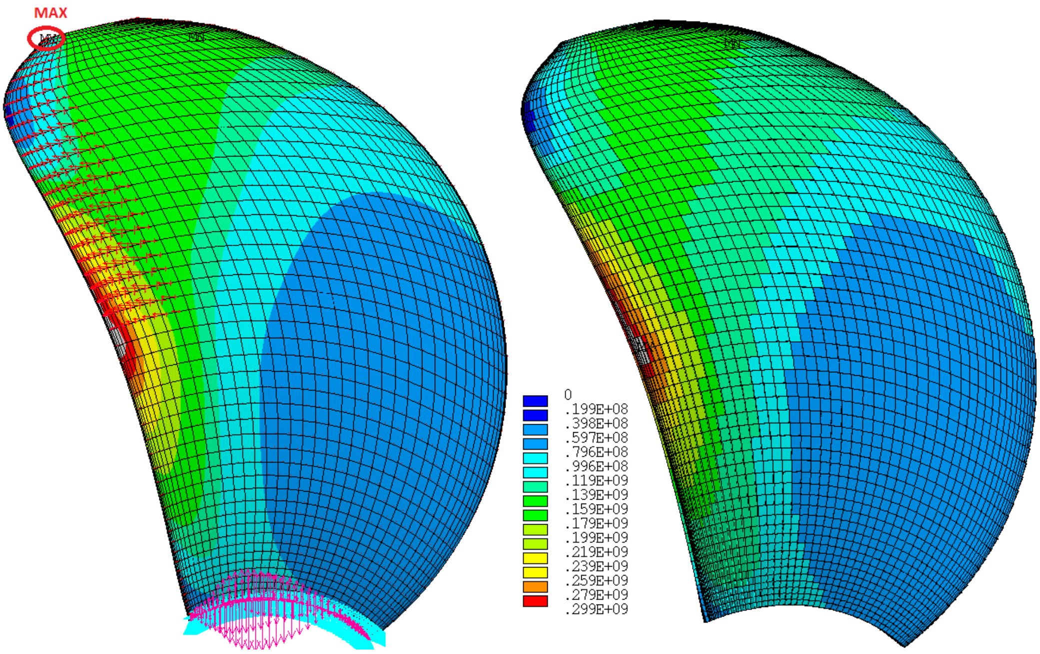

Figure 3-8: Structured solid modelling results on the left, structured shell modelling results on the right. Contour levels are identical and in [Pa].

[28] This implementation was available upon the start of this Master's thesis at MARIN.

[29] Despite several improvements were made by moving pre-processing tasks from ANSYS to MATLAB, additional steps in the element definition require significant computational resources. Hexahedral elements cannot be used at the propeller edges. Prism shaped elements are to be used instead. Prior to the element definition, volumes are defined in which an algorithm creates elements.

3.2.4 Structured Shell Elements

Lack of robustness of the structured solid modeling and faulty results due to degenerated elements in the tip region require a more robust method. Based on the prescription of a mid-surface, a shell element implementation is more efficient and robust, especially in the edge regions of a propeller blade. Elements are formulated directly by defining nodes of the mid-surface with their corresponding thickness.

Load Application

Grid refinement studies, however, revealed high scatter and poor convergence. Only for computational expensive grids the results compare well with the unstructured reference computation. High numerical uncertainty was present in this shell implementation due to incorrect application of loads. Although the magnitude of the forces was always scaled afterwards to the correct value, the location of the forces is highly grid-dependent since the nodes lie not the radial and chordwise positions as prescribed by the ice-class loads.

To solve this issue, the hyperbolic tangent distributions to define the distribution of panels in radial and chordwise direction are split at the required locations of the ice-class load cases as indicated in Figure 2-11.

Grid Refinement Study

Either linear or quadratic shell elements can be used. A grid refinement study is used to compare both: each implementation is considered for a sequence of ten grids in which the number of elements in radial direction is 10 higher than in chordwise direction. This gives more or less square elements in case of for the reference propeller. An example of the grid with results from linear shell elements is given in Figure 3-8. Quadratic shell elements produce a similar figure. Both elements converge to the reference value $\sigma_5 = 316.7 \pm 2.2$ [MPa]. An overview of the maximum stresses with their numerical uncertainty as is given in Figure 3-9.

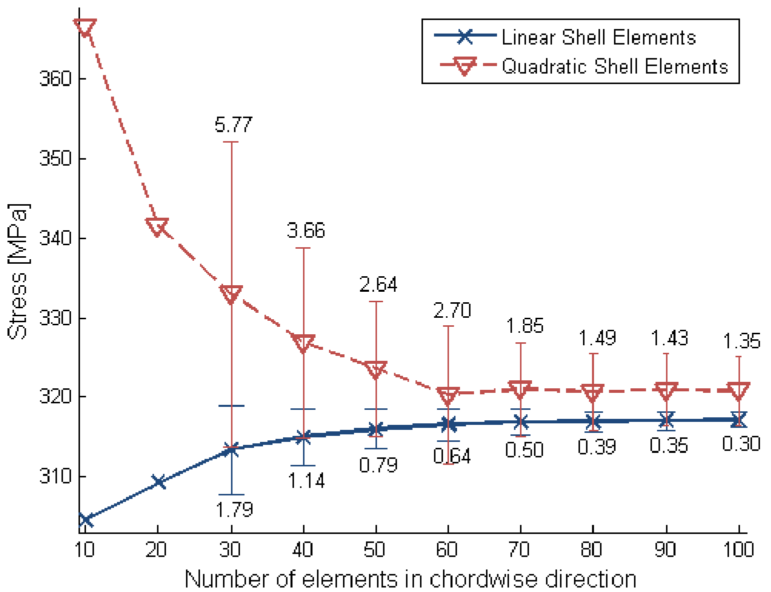

Figure 3-9: Comparison between linear shell elements and quadratic shell elements for different grid resolution. The number of elements in radial direction is 10 higher than the number of elements in chordwise direction. The errorbars present the numerical uncertainty. The numbers beneath and above the errorbars give the numerical uncertainty as percentage of the prediction.

As seen in the results, the quadratic shell implementation does not converge faster than its linear variant. Probably due to the inaccurate position of the mid-side nodes with respect to blade curvature, an error is introduced, which vanishes with finer grids. In the implementation it was assumed, for simplicity, that mid-side nodes could be defined as the average of the element corner nodes.

Mid-side nodes could be placed correctly by using the panelling procedure as outlined in section 2.1.3 for both corner nodes and and mid-side nodes. It is expected that this procedure would not result in shorter computational times for similar results. There is significant more pre-processing in both the panelling procedure and the FEM. In this Master's thesis no further comparison has been performed since linear shell elements perform well and can be used in an optimization.

Note that so far only the fifth load case was considered. Convergence and numerical uncertainty of the other load cases is given in Figure 3-10.

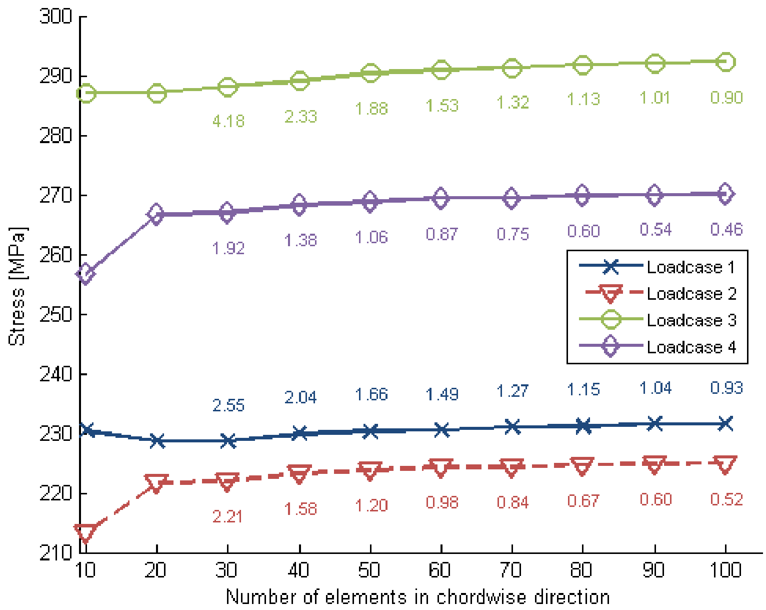

Figure 3-10: Convergence properties of the ice-class load cases with linear shell elements. The numbers in the figure give the numerical uncertainty in percentage of the prediction.

Maximum stress for load cases two, four and five is located at the trailing edge while for load cases one and three it appears at the hub, similarly to the propeller as presented with Figure 4-4. As the root fillet is not modelled, the results for load case one and three may feature higher numerical uncertainty. Valtonen (2015) indicates that the root fillet radius may have significant influence on stresses at the blade root. Conservativity is included in the current analysis method on top of the safety factor within Equation (5).

For the grid of 40x30 elements the numerical uncertainty of $U_{\sigma_3} = 4.18\%$ is acceptable. Disregarding load case one and three, load case two gives 2.21%. Noting the high safety factors within the ice class rules, uncertainties within the material and shape this is deemed acceptable. Also, the stresses will only be checked by the inequality of Equation (5), instead of being used and compared mutually for different propeller geometries within an optimization.

Concluding Remarks

This section will be closed with concluding remarks concerning the strength prediction of an ice-class propeller blade.

- A comparison between unstructured solid elements, structured solid elements and shell elements shows that shell elements perform the best on computational efficiency, numerical uncertainty and robustness. The shell element implementation has been developed within MATLAB and ANSYS in this Master's thesis. Best practice guidelines for the shell element implementation are created based on numerical uncertainty studies which shows that a grid of 40x30 elements in radial and chordwise direction already suffices within an optimization.

- A check of the displacements yields that they are in the order of 0.7% of the propeller diameter which is considered to be small and negligible. Hence, the linearization within Equation (60) is justified. There might be thin blade profiles with high stresses which do not comply, but they will automatically be rejected due to the stress constraints within the optimization framework.
- Grid dependency has been studied together with the grid refinement study. The grid was iteratively adapted such that the numerical uncertainty for the all load cases balanced. The edges need to be refined such that the pressure can be applied over the arc length of the profile in the correct direction. To predict the root bending stresses or buckle points of high skew propellers, resolution is needed in the midsection. A rectangular grid was generated while capturing the edge curvatures to be prepared for different locations of the maximum stress.
- The foregoing analysis was performed for the reference propeller only, while other propeller geometries might feature high stresses at other locations due to different physical mechanisms. Hence, it is recommended to repeat an uncertainty study for different propellers.

3.3 Ice Load Model

The ice-induced pressure distribution from Soininen (1998) as outlined in section 2.4.1 is implemented in MATLAB function `tjh_Soininen.m` such that the model is compatible with propeller blade profile parameterizations from section 2.1. This script follows the steps as indicated in Table 3-6. Its input consists of the blade profile, cut width, angle of attack and the ice strength giving the output in the form of the pressure distribution, loaded area and total force and its point of application.

Table 3-6: Flowchart of the 2D Soininen model as followed by `tjh_Soininen.m`

Specify	• blade profile, cut width, angle of attack & ice strength
Rotate	• blade profile according to the angle of attack
Determine	• pressure values and location of the pressure points
Apply	• pressure distribution on the profile arclength
Integrate	• pressure distribution using a rectangle method
Decompose	• resulting force and moment
Determine	• point of application of the force

The model is considered in subsection 3.3.1 for its sensitivity to the angle of attack and the blade profile geometry. However, since an ice simulation model is explicitly needed in combination with Soininen's model to investigate ice loading for a complete propeller, Soininen's ice contact model is only suited in a full stochastic simulation in which the ice block position and size is randomly varied. It makes no sense to optimize the propeller for one angle of attack only. It would, however, be computationally too expensive if ice simulation parameters have to be varied like was done in the work for the ice class rules for each propeller geometry. A compromise is sought: leaving time simulations, a steady milling situation for an infinite ice block can be analyzed. This simulation will be developed in subsection 3.3.2.

3.3.1 2D Parameters

To become familiar and get confidence in the pressure distribution as proposed by Soininen, variation of thickness, location of maximum thickness and angle of attack are considered in the itemization below.

1. **Thickness.** The angles on which Soininen's model is based are located at larger chordwise positions on the profile for thicker blade profiles. Hence, high ice contact pressure will extent over a larger area of the blade: thicker propellers will undergo higher forces according to Soininen's model. Figure 3-11 supports this hypothesis. Three blade profiles, with different maximum thickness, are presented with their pressure distributions at zero angle of attack. Note that the chordwise distribution of thickness and camber is constant; the pressure distribution extents to the chordwise position of maximum thickness for all blade profiles. The magnitude of pressure, however, extends further on the blade profile with increasing thickness.
2. **Position of maximum thickness.** If the chordwise position of maximum thickness would be moved, the chordwise length of ice-exposure area will change. An overview of the variation is given by Figure 3-12. Blunt edges will experience short ice-contact while its force is directed in blade profile direction. Sharper leading edges, on the other hand, are longer exposed to the ice. The force is directed more perpendicular with respect to the blade which might give higher bending moments.
3. **Angle of attack.** Besides blade profile geometry, the angle of attack largely influences the ice-contact area. According to Soininen's model, ice contact at the pressure side induces much lower pressure as contact on the suction side. Hence, positive angles of attack will cause high ice-loads. An overview is presented in Figure 3-13 in which three angles of attack are presented. The blade profile in green with angle of attack α of 5 degrees is loaded over the entire suction side.

The observations are based on the graphs in Figure 3-11 to Figure 3-13. In these figures the colors and line-style indicate different blade profiles in the left-hand graph. The bold part of the blade profile contour gives the extent of ice-contact. The right hand graph gives the ice-induced pressure according to Soininen's model.

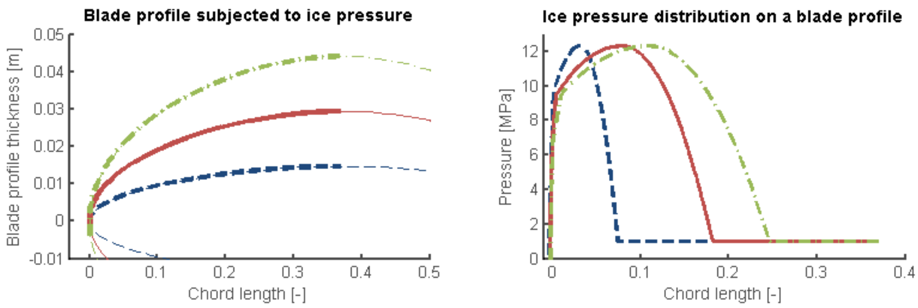

Figure 3-11: Variation of maximum blade profile thickness. The left graph gives three blade profiles with different thickness. Colors and line-style are repeated in the right figure which gives the ice-induced pressure according to Soininen's model.

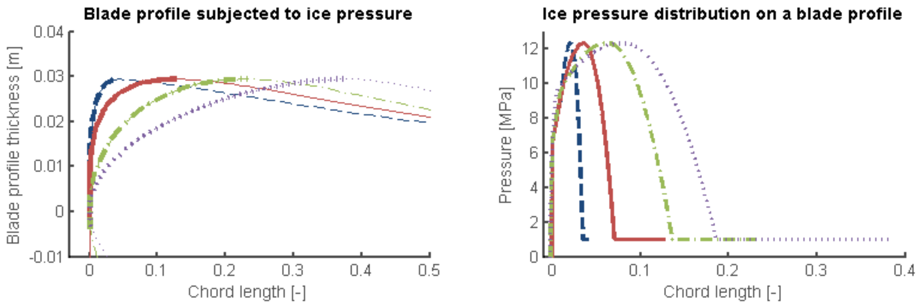

Figure 3-12: Variation of chordwise position of maximum thickness. The left graph gives four blade profiles with different position of maximum thickness. Colors and line-style are repeated in the right figure which gives the ice-induced pressure according to Soininen's model.

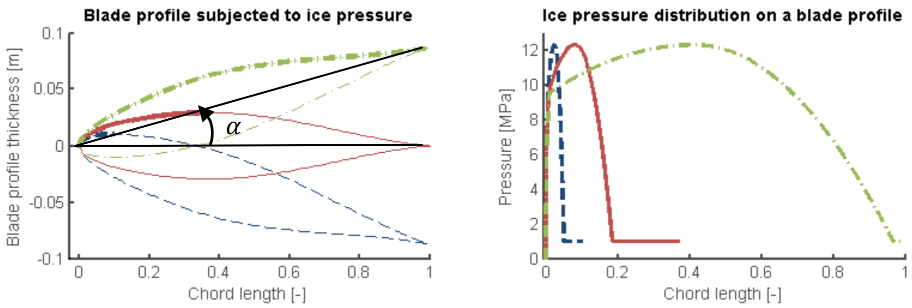

Figure 3-13: Variation of the angle of attack α. The left graph shows three blade profiles under -5, 0 and 5 degree angle of attack. α is positive counter clockwise and further defined in Soininen's model as indicated by the line from leading edge to trailing edge. The right graph gives the pressure distribution.

It should be noted that only one propeller geometry was tested during Soininen's laboratory experiments, his model is hence only valid for conventional ice-class propellers with similar geometry. Further validation for other propeller geometries is outside the scope of this Master's thesis.

It may be argued that the results of Soininen (1998) and Veitch (1995) compare qualitatively. Veitch used tools that can be imagined as either side of a blade profile, split in half at the chord line to separate the physical ice failure mechanisms of spalling and crushing. Pressure side tools have almost no contact with the ice which is represented by Soininen's model as well. Veitch' suction side tools yield forces which are a factor 2 to 5 higher than pressure side tools, depending on angle of attack and profile shape. Roughly, these mechanisms are incorporated by Soininen which permits the usage of Soininen's idealized pressure distribution as predictor of ice-induced loading.

In Huisman (2015) it was hypothesized in that sharper edge could lead to lower ice-induced forces. This hypothesis should be rejected considering the governing physics of ice interaction. Soininen's idealized pressure distribution, which models these physical processes, predicts that blunt leading edges yield lower forces.

3.3.2 3D Milling Simulation Model

The idealized pressure distribution as proposed by Soininen (1998) acts on the propeller blade sections. To include the complete propeller geometry, the propeller should be discretized into blade profile sections over the radius.

It is assumed that the maximum ice-load during ice milling can be predicted using a steady computation. If the cut depth is large, the whole propeller blade profile cuts through the ice from a certain radius and upwards. Propeller pitch together with the apparent propeller blade speed is taken as a measure for the angle of attack.

A conceptual sketch of the propeller and the ice in this simulation is presented with Figure 3-14. It shows a cross section of a large idealized rectangular ice mass through which the propeller mills. Concerning this figure the following notes should be made:

- A propeller impacts the idealized massive ice piece from 0.6R and above yielding a cut depth of 0.4R.
- The grooves from the previous blades are also visualized. These define the cut width w which is non-constant over de radius as function of advance ratio, propeller pitch and blade profile shape. For low advance ratio the suction side crushing is dominant. The whole suction side is in contact with the ice. For high advance ratios the physical failure mechanism differs as only as only a small part of the blade crushes the ice while the leading edge spalls most of the ice.
- In the tip section the angle of attack will not only be worse, such that the suction side is loaded more, also the cut width is larger yielding a higher leading edge pressure. Hence, while the ice-class rules assume uniform pressure, the pressure distribution will be non-constant, both in radial and chordwise direction.
- In reality the contact surface will be non-smooth and highly irregular. Moreover, the spalling behavior at the pressure side is not visualized, but indicated with the black irregular lines.

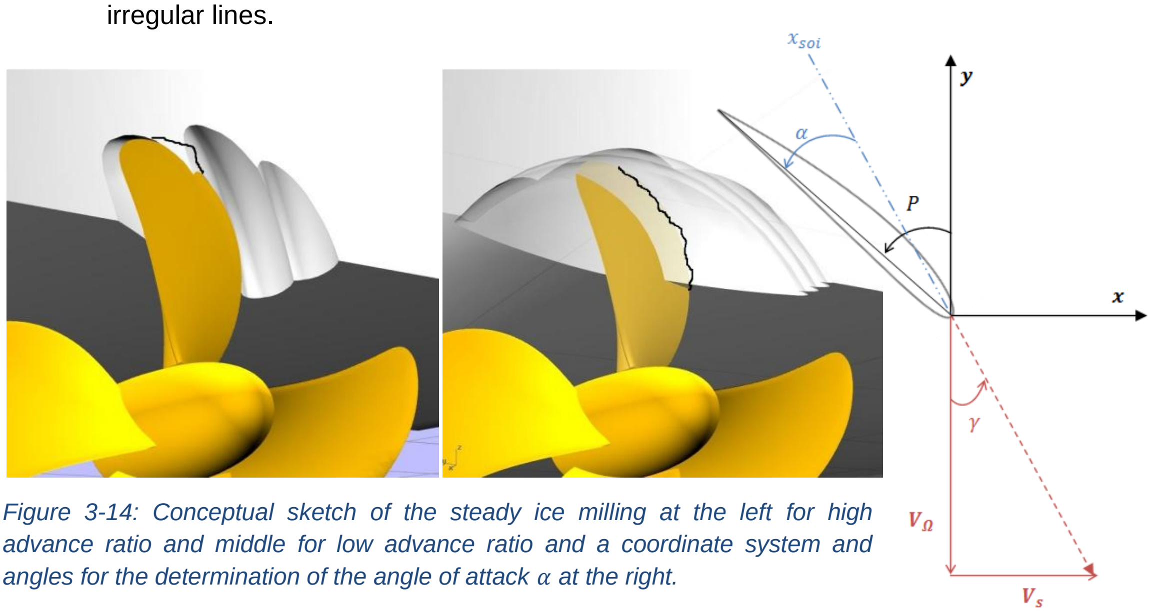

Figure 3-14: Conceptual sketch of the steady ice milling at the left for high advance ratio and middle for low advance ratio and a coordinate system and angles for the determination of the angle of attack α at the right.

A flowchart of the 3D model is given in Table 3-7 in which all the steps of the implementation are listed[30]. The right of Figure 3-14 defines the coordinate system in which V_Ω denotes the rotational speed, V_S the velocity between ship and ice, γ the advance direction of a propeller blade, P the propeller pitch at a certain radius and α the resulting angle of attack.

In the 2D implementation of Soininen's model the forces are computed with reference to the x_{soi}-axis as given at the right in Figure 3-14. Hence they have to be transformed to the propeller axis system (x, y). A cylindrical coordinate system is used to find the normal vectors at the points of application. The propeller is discretized using the paneling procedure such that at each radial and chordwise location the normal vectors can be computed with the cross product of the tangential vectors in radial and chordwise direction. Based on these vectors the resultant force is rotated in the correct direction in space.

[30] Similar steps are programmed in the user defined MATLAB function tjh_Soininen_3D which is available upon request.

Table 3-7: Flowchart of 3D ice-interaction analysis based on Soininen's model and a steady infinite-mass ice block during ice milling.

Transform	• propeller in a description for R = 0.6-1.0 [-] only.
Determine	• angle of attack α and cut width w as function of propeller pitch P and advance ratio J
Scale	• sections with chordlength
Evaluate	• 2D Soininen model for forces and points of application per section
Determine	• the resultant forces per section
Transform	• forces into force components in the propeller coordinate system
Position	• points of application in 3D according to the procedure in Table 2.1
Determine	• 3D orientation of the forces by means of normal vectors to the blade at the point of application
Rotate	• the force in z-direction
Decompose	• resultant force into 3D components
Integrate	• the forces over radial length and dimensionalise
Compute	• ice-induced torque and bending moment around the root

Comparison with the ice class rules

A comparison with load of the ice class rules can be performed as check whether Soininen's model gives loads within the same order of magnitude. A computation for the reference propeller yields Figure 3-15 below.

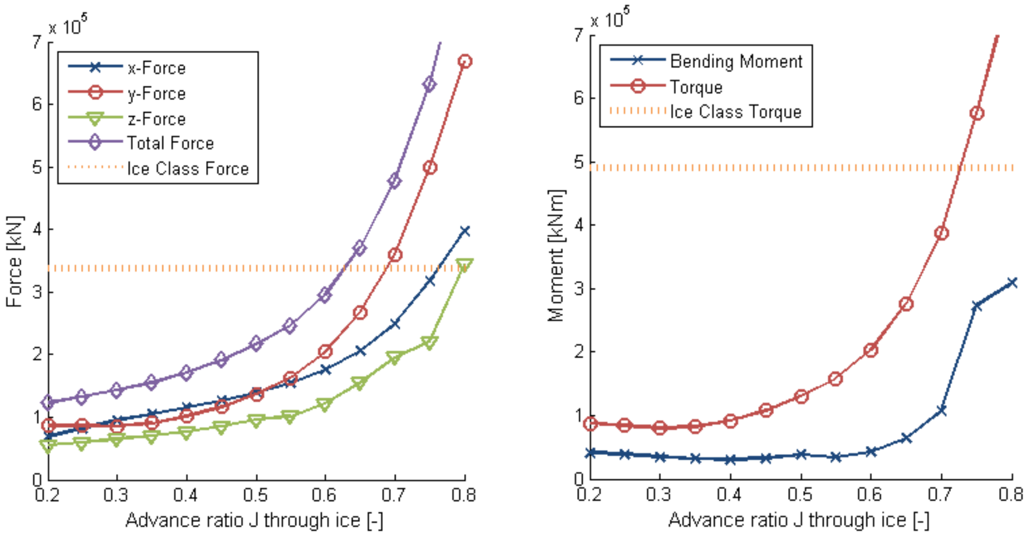

Figure 3-15: Comparison of the magnitude of ice loading as function of advance ratio for the reference propeller. The value prescribed in the ice class rules is presented with the dotted orange line. At the left the forces are given, while at the left the ice-induced bending moment and torque are shown.

In addition to the value of the total force and its comparison with the prescribed force within the ice-class rules, the root bending moment and the ice-induced torque are presented as well. The following can be observed from Figure 3-15:

- The order or magnitude is correctly predicted for both the ice-induced force and torque.
- Ice-induced loading is, as expected from the sketches in Figure 3-14, dependent on the advance ratio. Typical advance ratios in ice are below the normal operation point of J = 0.676 due to the added resistance in ice. For this region is appears that there is additional conservativity within the ice-class rules if the assumption is valid that steady ice load computations suffice for the estimation of the highest ice loading. The predication of the total force is significantly lower as prescribed within the ice class rules. It appears that the alternative design route within the ice-class rules can be utilized in the future to design higher efficient propellers as described in Huisman (2015).
- The location of the ice load as predicted within the simulation differs with the first ice-class load case which it should resemble for lower advance ratios. While on average over de radius the prescribed impact location of 20% of the chord length corresponds well with the simulation for higher advance ratios, the impact location for lower advance ratios is located towards the leading edge with a length of only 2% of the chord length. This also explains the behavior of the bending moment. For low advance ratios, the force is low with a higher moment arm while at higher advance ratios, for higher forces, the moment arm becomes lower.

Since the bending moment is a function of both the force and the moment arm, optimization is not only required for the total ice-induced force, but also for the bending moment itself. Pitch becomes not only important in the prescription of the angle of attack, but also in the determination of the bending moment. It is assumed that the root bending moment is one of the mechanisms which govern the required propeller blade strength.

Concluding Remarks

Following the conclusions from the 2D model, it can be hypothesized that the most important parameters for the 3D simulation model are the angle of attack α, the blade profile shape, propeller pitch and thickness. Other parameters such as camber can also indirectly influence the ice-induced loading due to the mean pitch adaptation procedure within the optimization.

The developed ice simulation model can be used within an optimization to quantify ice performance as function of ice-induced propeller torque, ice bending moment and total ice force. Limiting the ice torque as function of propeller geometry provides a larger operational window for the ship in ice conditions, while the ice-induced bending moment might be considered as measure for fatigue and strength. Possibly, the alternative design route within the ice-class rules may be utilized by allowing lower design ice forces for such propeller geometries.

3.4 Computational Framework

The goal of this section is to combine the geometry parameterization, optimization algorithm and computational methods for hydrodynamics, structural strength and ice loads into a computational framework.

A fully operational optimization framework for geometry parameterization, optimization algorithm and the coupling with hydrodynamic BEM PROCAL was already provided by MARIN within MATLAB as basis. Besides numerous small updates and debugging, the following expansions were made to the existing computational framework within this Master's thesis:

1. Generalization of optimization structure by separating the optimization algorithm, geometry parameterization and computational methods.
2. Implementation and coupling of a shell element based FEM and the ice-load model.
3. Update and expansions of the geometry parameterization to allow for chordwise distributions and different radial distributions including thickness according to section 2.1.2.

Separation

Generalization of the computational framework is achieved by using a data array ***O*** in which optimization relevant data such as objectives, design parameters, ranks and constraint violations are tracked per generation, independently of parameterization, optimization algorithm or computational methods. Data array ***P*** stores propeller geometry and all computational results. An interface writes new optimization algorithm generated design parameters to ***P***. After geometry generation and analysis this interface searches within ***P*** for the required input for ***O***.

Coupling

Strength computations are performed with ANSYS and coupled to the computational framework. ANSYS however, could not be installed on the LINUX cluster of high performance computers. To still allow PROCAL computations on a LINUX cluster[31], ANSYS computations are performed separately outside the main computational optimization loop in a different MATLAB process. Each second thrust convergence is checked by the ANSYS loop. Upon thrust convergence, the propeller geometry is stored and read by the ANSYS computation loop. ANSYS is called on the local WINDOWS computer for an ice-load strength analysis. After all propellers have been computed, the main computational optimization loop checks whether all propellers have been computed by ANSYS after which the results are collected. The ice load model is directly implemented within the main loop. An overview and flowchart of the current computational framework is provided with Table 3-8.

Computational Time

Typically, an unsteady PROCAL computation takes between 7 to 12 minutes with grid of 26x36 elements in chordwise and radial direction. In comparison, a complete strength analysis with ANSYS takes up to 30 seconds for a 40x30 grid including pre- and post processing in MATLAB. Computation time for the ice-load model is negligible with only 3 seconds for a range of angles of attack. A Windows 7 workstation with an Intel® Xeon® CPU W3520 @ 2.67 [GHz] was used with 6.00 [GB] installed work memory.

Analysis Failures

If a computation fails for any reason the optimization should still proceed. Errors may appear in the geometry generation procedure, paneling procedure or in the hydrodynamic or strength analysis. Also for thrust divergence, the whole propeller is disqualified for further analysis. Hence, the propeller will get a low rank and become extinct. Failure is dealt with by assigning the objectives the worst possible value such that the optimization algorithm will disregard the propeller during the ranking process.

[31] Although tested and implemented for the cluster, results for this thesis are generated on a single Windows workstation due to cluster maintenance and updates at the time. Preferably, the cluster should be used with larger population sizes and possibly cavitation computations.

Table 3-8: Computational sequence of the optimization procedure. The first four blocks in present the start-up phase, the next four blocks are performed for each individual propeller. Each generation is processed in the last two red blocks.

Get	• all input and settings to run the analysis tools and define the optimization problem
Check	• input with common defaults and reference propeller
Initialize ***O***	• optimization structure with design variables, objectives and constraints
Generate P_0	• first propeller generation by random independent design parameters
Iterate	• the mean pitch in steady hydrodynamic computations for the required thrust in the designpoint
Subject (1)	• converged propellers in an unsteady time simulation to the hydrodynamic BEM PROCAL
Subject (2)	• converged propellers to the load cases of the ice class rules within the shell FEM implementation in ANSYS
Subject (3)	• converged propellers to the ice-load model based on Soininen's simplified ice pressure distribution
Write	• results of each propeller to the optimization structure
Rank P_{i-2}, P_{i-1}	• the current population of propellers according to their objectives and constraint violations
Generate P_i	• new generation in a genetic algorithm based on sorting, reproduction, crossover and mutation.

4 OPTIMIZATION RESULTS

The computational methods to obtain the optimization objectives and constraints as introduced in the introduction have been discussed in previous chapters. This chapter applies the computational framework on the case study as introduced by section 1.5.

Prior to full optimization, numerous test cases have been performed. Only four will be considered in this report which cover all adaptations, tuning and conclusions from the test phase. Table 4-1 gives an overview of the simulations which are addressed in this chapter.

Table 4-1: Definition of optimization cases. For each case the distributions that have been varied and the objectives are indicated. Note that the C- in the design parameters stands for a chordwise distribution while the others are defined over the radius as discussed in section 2.1.2.

				Design Parameters								Objectives				
		ICE CLASS	UNSTEADY	CHORD	PITCH	RAKE	SKEW	THICKNESS	CAMBER	C-THICKNESS	C-CAMBER	EFFICIENCY	MASS	Δ THRUST	ICE BENDING	ICE FORCE
Test Cases	T-I	■						■				■	■			
	T-II	■						■	■	■	■	■	■			
	T-III	■	■	■	■			■	■	■	■	■		■		
	T-IV	■	■	■	■	■	■	■	■	■	■	■	■	■		
Full Optimization	F-I	■	■	■	■	■	■	■	■	■	■	■	■	■	■	■

All optimization cases have been performed while taking the ice-class stress constraints into account. Design parameters are based on the parameterization of the radial and chordwise geometry distributions according to section 2.1.2 which defines the free variables within each optimization case. If not varied, the distributions from the reference propeller are maintained. The bounds for the design variables are iteratively found during the test phase. The final numbers for the case study can be found in Appendix A.

This chapter is organized in two sections. Section 4.1 describes the test phase prior to more extensive optimization with the full design parameter set. After confidence in the computational framework has been grown, the full optimization will be addressed in section 4.2. It should be noted that often the conclusions from the test cases are also valid for the full optimization.

Before continuing this chapter the following remarks should be made for legibility and understanding:

- In this chapter the best propellers are defined as propellers which feature the best objective values within a certain population, generation, geometry parameterization and choice of design variables. It is possible that when other optimization or parameterization techniques would be applied, even better propellers could be designed in the future.
- The optimization computations in this Master's thesis are limited to small populations due to computational resources. Nonetheless, the principles can be applied for larger populations which will, eventually, reach better objective values as observed by Nuland (2014).
- In optimization-case overview plots the colours vary from blue to red from left to right, indicating later generations within the optimization. Results of the last generation are encircled. The reference propeller from the case study will be indicated with a larger circle. Gray x-marked results indicate propellers which do not satisfy at least one of the ice-class stress constraints but survived the ranking process within the genetic algorithm.

4.1 Test Cases

Optimization test cases prior to full optimization have been performed to enhance, debug and test the computational framework. It should be assessed whether the geometry parameterization suffices while best practice bounds for the design parameters should be established. Above all, the ice-class stress constraints should be automatically satisfied to design for ice-class propellers. In general the test phase suits to prepare for full optimization and provides direction to the answering of the main question. The test cases are summarized into four parts as indicated in Table 4-1 with T-I to T-IV. Specifically, the test cases are intended

1. to assess the ability to comply with the ice-class stress constraints (T-I),
2. to define proper bounds for the chordwise thickness and camber distributions while assessing the ability to use steady computations only (T-II),
3. to include hydrodynamic effects of the interaction of the propeller with the ship by unsteady hydrodynamic computations (T-III) and
4. to show that ice-class propellers may feature significant skew (T-IV) and still be in accordance with the ice-class rules.

These test cases will subsequently be addressed in the following subsections. Each subsection will be closed with concluding remarks and recommendations.

4.1.1 Thickness Optimization (T-I)

This optimization case is intended to test the algorithm in its ability to comply with the ice-class stress constraints. Two objectives to maximize efficiency and minimize mass are chosen. The propeller is fully based on the reference propeller of the case study from section 1.5. Only the radial thickness distribution is varied. A population of 128 propellers is analyzed in steady computations for 30 generations.

Optimization Results

A plot of the optimization progression and its results of the simulation is given in Figure 4-1. All propellers within the simulation are plotted, also the reference propeller is included with the black dotted circle. It is observed that an improvement in efficiency cannot be reached. Propeller mass, however, is slightly reduced with 5.4%. More importantly, the optimized propellers are ice-class propellers in contrast to the reference propeller which does not satisfy the ice-class constraints.

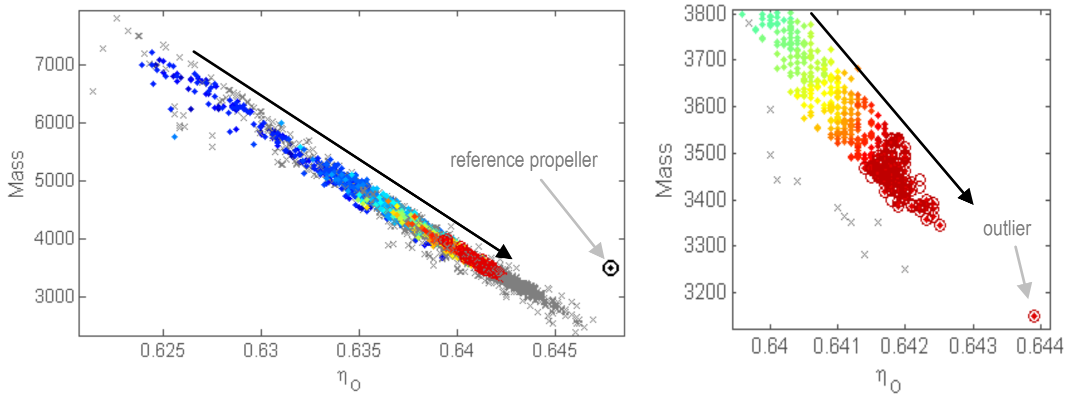

Figure 4-1: Overview of thickness optimization of the reference propeller. Mass [kg] versus efficiency η_O [-] is plotted for the unsorted full design space to the left. A close-up on the best propellers is given to the right where the propellers are ranked for clarity of the representation. The large black dotted circle gives the initial reference propeller of the case study.

The algorithm searches its way to the bottom right for highest efficiency while having the lowest possible mass.The randomly generated initial designs define the starting point of the optimization. Only thick heavy propellers satisfy the ice-class constraints, hence, the algorithm starts in the top left of Figure 4-1. In the early generations, the search area is wide, while later on the algorithm coverges almost linearly. Physically, mass is indirectly linked with efficiency via the expanded blade area ratio and the chord and camber ratios with respect to thickness. Hence, this case also indirectly varies the blade shape and the resulting pressure distributions.

Infeasible propellers

The current algorithm actively searches towards higher efficiency propellers within the prescribed design parameter bounds, but is limited by the ice-class stress constraints. Although the algorithm is sufficiently adventurous to search the allowable design space, 48% of the computed propellers did not satisfy the ice-class constraints. Only 10% of them survived at least one generation and were subjected to the optimization tournament procedure, refer to section 2.7.3.

The low-ranked short-living propellers which extinct after the ranking process are indicated with gray 'x' markers. They obtain higher efficiency and lower mass, but do not satisfy at least one of the ice-class stress constraints. The close-up of Figure 4-1 and following figures of the optimization results show only the ranked population for clarity of the presentation. The close-up shows that very little stress violating propeller survive their generation. However, taking the constraint violating propellers explictly into account could lead to faster convergence and more efficient optimization instead of the current trial and error behaviour. The optimium could then be approached from both constraint violation and constraint obedience points of view.

Prior test cases showed that the algorithm performs better by prescribing five separate constraints for each load case instead of constraining the maximum of the five load cases. Propellers can be ranked according to the number of ice-class load cases that are satisfied.

Population Size

Prior to the case presented here, a smaller population size of 30 propellers was considered which did not converge. Probably due to the absence of a clear Pareto front, the genetic algorithm could not rank the propellers properly. Hence, the optimization was restarted with the current large population size of 128, which eventually reached better convergence as already observed and concluded by Nuland (2014).

Convergence

Behaviour of the optimization algorithm can also be studied by means of a visualisation of convergence. Figure 4-2 presents convergence for both the pure offspring or unranked generations and the generations after the tournament ranking process. Especially the first two generations produce a lot of propellers which violate the constraints. Generation three tries to correct this and searches for thicker heavier propellers; mass rises and efficiency falls. When the parent population in generation four and further satisfies the stress constraints the efficiency rises again until convergence. The unranked population, which does not necessarily comply to the constraints, is plotted as well to show the aforementioned adventurousness of the algorithm.

Outliers

Probably due to an error in a restart around generation seven, an outlier is present there that spoils the convergence plot for both efficiency and weight. The outlier is not present in the unranked offspring while it suddenly appears after ranking. Hence, a design check is recommendable. It indeed shows that the outlier does not satisfy the stress constraints and remains an outlier throughout the whole optimization altough the algorithm actively tries to fill the gap between the best propellers and the outliers considering the large density of infeasible propellers. If the outlier would be absent, it is expected that the ratio between infeasible ice-class constraint violating propellers and feasible propellers would be lower. Note that the outlier predicted in generation twelve satisfies the constraints and attracts the whole generation towards better objectives. This outlier survives until the end as best propeller.

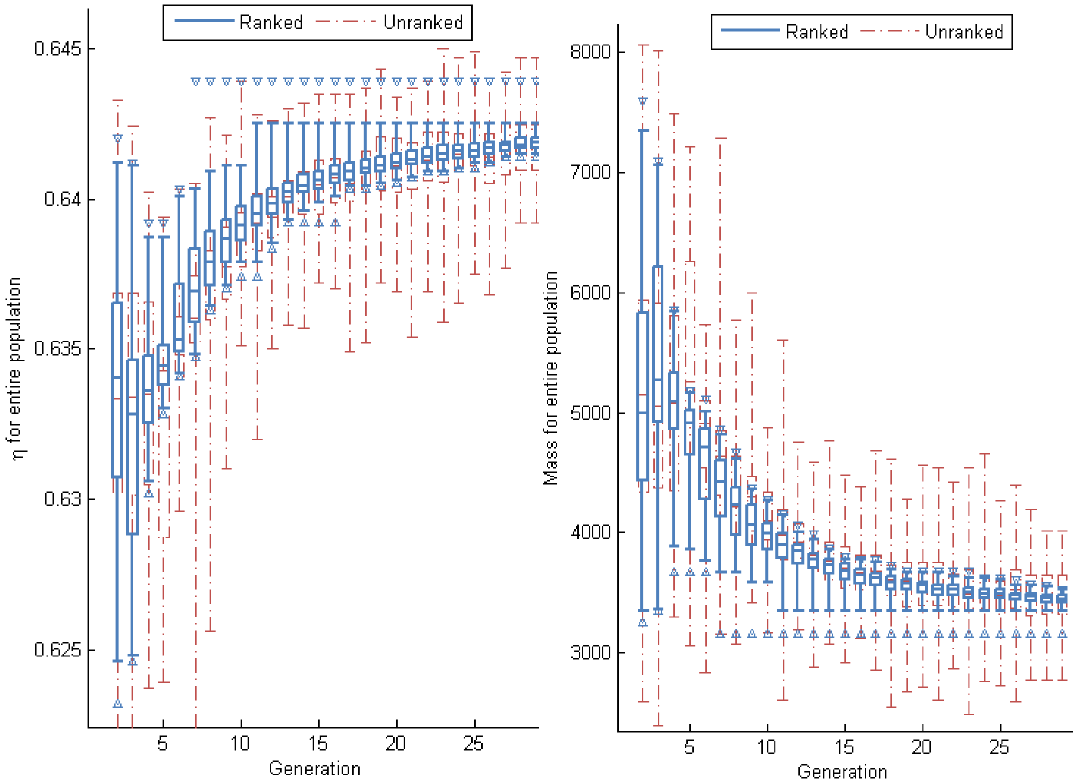

Figure 4-2: Convergence of the thickness optimization of the reference propeller. Both the ranked generations and the unranked generations (pure offspring) are given for efficiency (left) and mass (right). The box plots give the extremes, first and third quartiles and the median of each generation. Outliers for the ranked population are plotted separately with markers.

Analysis of best propellers

The best propellers are selected for further analysis. The ten best performing propellers are plotted in Figure 4-3. The thickness distribution only suffices, the other parameters are constant.

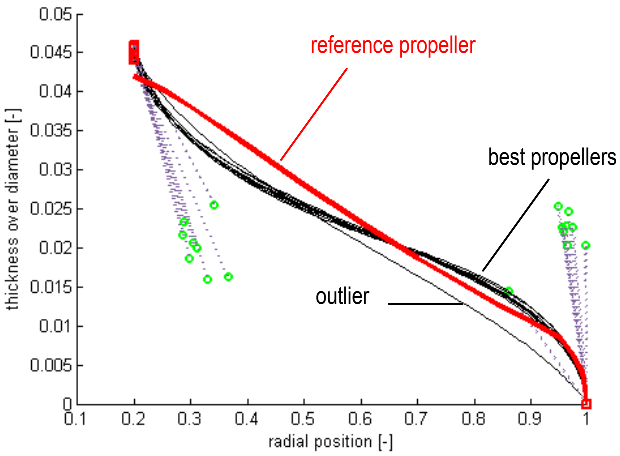

Figure 4-3: Comparison of simulation results. Thickness distributions with their control and handle points are visualised. Also the thickness distribution of the reference propeller is plotted for comparison.

The shape of the thickness distribution might be explained as follows. The thickness at the hub is governed by the third load case. As already observed in Figure 3-10, the third load cases gives the highest stresses at the hub for the reference propeller. The fifth load case with load on the pressure side of the trailing edge requires thickness in the mid-section of the blade. The tip is non-critical for the current settings. Hence, there may be room for improvement by more advanced parametrization of the thickness distribution. The five load cases are presented in an overview below in Figure 4-4. The side with highest stresses is shown. Critical load cases three and five are presented in the top, while the other, non-critical load cases are visualised below them.

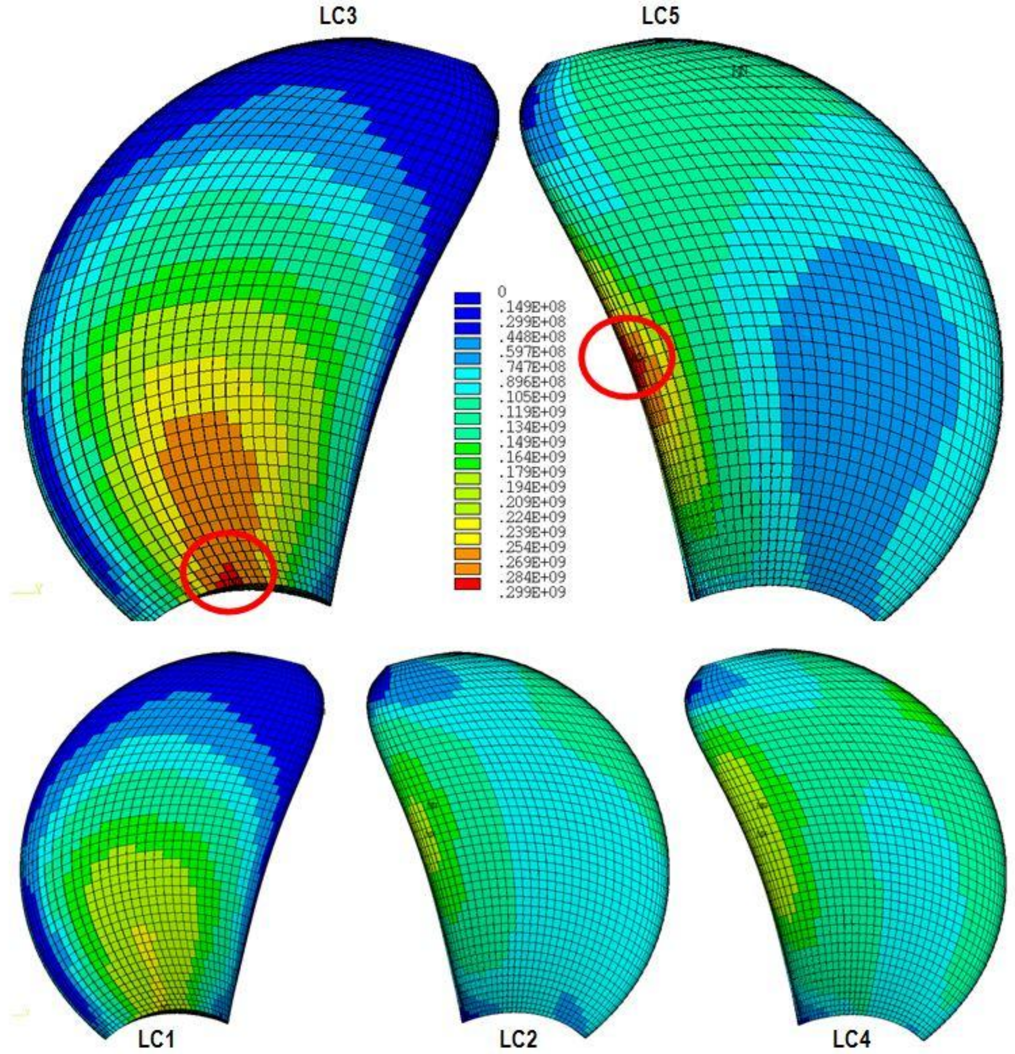

Figure 4-4: Overview of stresses due to the application of the ice-class load cases for the thickness optimization test case. The colours present the Von Mises stress in [Pa]. Load case (LC) three and five feature critical stresses for the optimization algorithm. Their location of maximum stress is indicated with a red circle.

Concluding Remarks

Concerning this optimization test case in which only the thickness and its distribution is varied, the following concluding remarks should be made:

- The proposed computational framework seems suitable for ice-class propeller design. The ice-class stress constraints can be evaluated and satisfied automatically.
- A large portion of constraint violating propellers is rejected by the algorithm. Taking them into account in addition to the feasible propellers could lead to both faster convergence and higher computational efficiency of the complete optimization.
- This thickness optimization test case does not give improvements in efficiency for the chosen thickness parametrization. Mass, however, can be reduced substantially with 5% in this case study which might be interesting in practice for FPPs.
- A large population reaches better convergence while the probablity in finding the global optimum is increased. However, current computational resources limit the size of the population.
- It is recommended to use a more sophisticated thickness distribution which avoids the generation of a fillet at the hub and allows for a finite thickness at the tip. Considering the efficiency, thickness distribution and stresses of the reference

propeller, it is expected that the optimization can converge further towards lower mass and higher efficiency.

- Although laid out for ice-class propellers, the computational framework can be used for non-ice class propellers too. Hydrodynamic pressures could be applied, either with matching meshes for BEM and FEM or with interpolation techniques.

4.1.2 Blade Profile Design (T-II)

The goal in this optimization case is to define proper bounds for the chordwise thickness and camber distributions such that reasonable blade profiles can be generated. Steady hydrodynamic computations are used to search for pitfalls within the computational framework. As initial bounds were solely intended to generate smooth, continuous distributions, test cases showed that additional bounds need to be prescribed.

Both the radial and chordwise description of the camber and thickness distributions are taken as design parameters. A population of 30 propellers is analyzed in steady computations for 65 generations taking mass and efficiency as objectives.

Optimization Results

Although the algorithm converges to high efficiency and low mass, see Figure 4-5, this optimization case does not result in better propellers than before when only thickness was varied in the previous section 4.1.1. There is no significant higher efficiency and even higher propeller mass. Probably, the absence of a clear trade-off curve complicates convergence. Since ranking is based on the position along the front, the low efficiency propellers with low mass spoil convergence towards high efficiency.

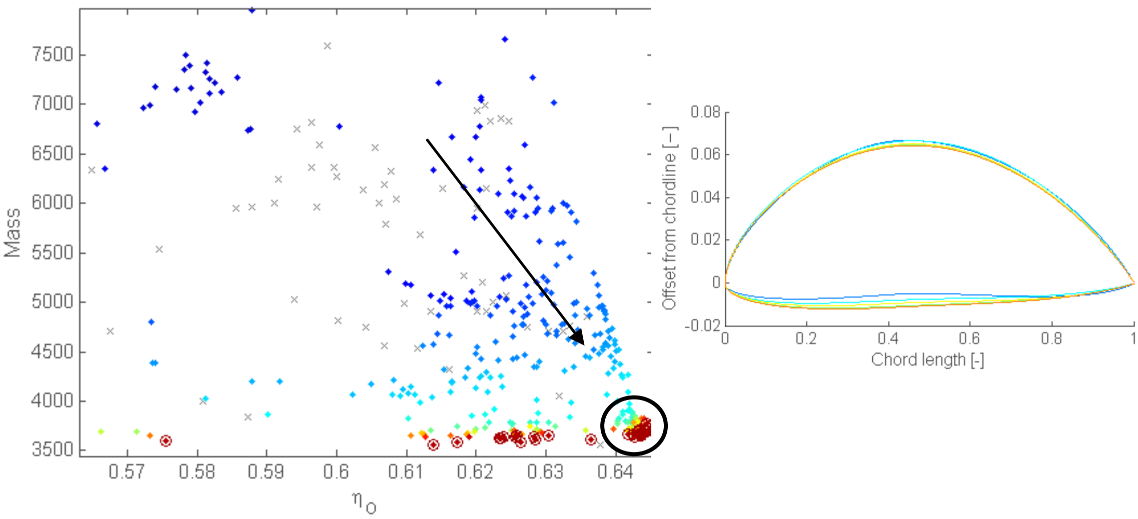

Figure 4-5: Optimization overview for case C.I with mass [kg] and efficiency η_O [-]. Blade profiles are varied as well as the radial thickness and camber distribution. A selection of blade profiles within the encircled clustering is given in the right graph. The offset is dimensionless with propeller diameter.

Similar thickness distributions as for the thickness optimization test case in Figure 4-3 are observed. Apparently, the population size of 30 propellers is also able to converge to the expected result from section 4.1.1 which used 128 propellers per generation.

Hence, it can be concluded that the computational framework can generate blade profiles which are as efficient as the blade profile of the reference propeller. The parameterization can be used for further optimization cases.

Prior Test Cases

Prior test cases, however, did not generate profiles that are worth to be considered as visualized in Figure 4-6. Three typical undesirable blade profiles are selected for discussion:

- Green striped-dotted profile which features a very blunt leading edge, high thickness and a sharp shoulders at the suction side.
- Blue solid profile which seems worth to consider. However, a numerical artefact is introduced at the trailing edge. As in reality separation will occur from the small flap, the assumptions within the BEM imply that the flow will follow the profile, yielding unphysical wake alignment and circulation. Consequently, pressures will not be predicted correctly.
- The red dotted profile which has pronounced shoulders at both pressure and suction side. In addition, the location of maximum thickness is located too far from the leading edge for proper chordwise pressure distributions.

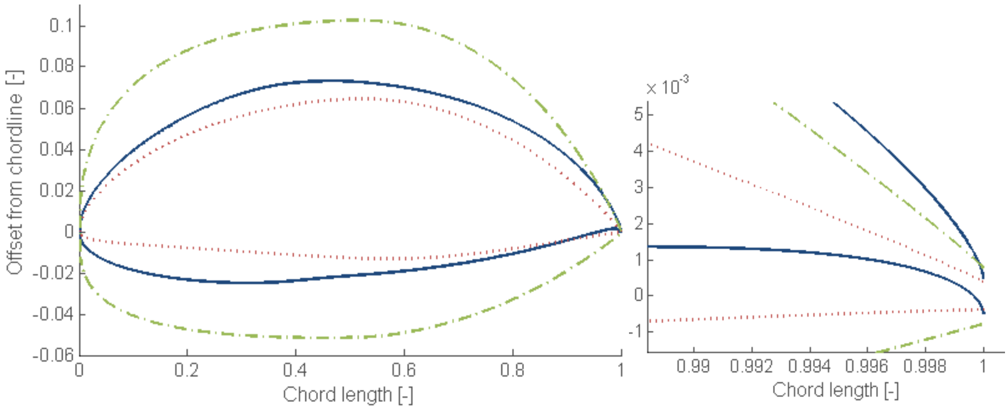

Figure 4-6: Profiles at 0.7R from prior optimization test series. The right graph is a close up of the trailing edge. The offset is dimensionless with propeller diameter.

Hence, proper bounds are required for the chordwise thickness and camber distribution to avoid unfeasible geometries such as the wedges and those presented in Figure 4-6. The bounds resulting from the test phase are presented in Appendix A.

Concluding Remarks

Although it is noted that the computational framework can generate blade profiles which are worth to consider further, it is also observed that due to the limitations of BEM and steady computations, the optimization algorithm cannot find reasonable profiles automatically. Solely considering the efficiency objective without any bounds on the geometry generation, hydrodynamic properties such as flow separation, pressure pulses, noise and cavitation are not taken into account sufficiently well.

Hence, steady hydrodynamic computations, without consideration of the wake field, do not suffice for propeller optimization. In addition, proper design parameter bounds on the chordwise thickness and camber distributions are required to avoid numerical artefacts implied by the BEM assumptions.

There is a trade-off between geometry parameterization bounds and the number of infeasible propellers due to the absence of the bounds. Bounds might overcast the global optimum if chosen too conservative. They are always a compromise to avoid the generation of too much diverged propellers on which the algorithms fails.

Furthermore it should be noted that a pronounced trade-off or relation between objectives is required for optimization progression. This case shows several low mass propellers with low efficiency which are ranked for the parent population therewith interfering with the high efficiency propellers.

4.1.3 Unsteady Hydrodynamic Computations (T-III)

The goal for this case is to test the applicability of the thrust variation objective in unsteady hydrodynamic computations to include the interaction with the ship by means of its effective wake field.

Design Parameters

The trade-off between thrust variation and efficiency should be predicted during this test case without the large bias which would be introduced by taking skew into account. This optimization case, when leaving the skew distribution constant, gives insight in the possibilities to reduce thrust variations without featuring high skew angles. Rake was not considered too due to its little influence on the hydrodynamics and the need for a limited number of design parameters for earlier convergence. Moreover, due to the forward and backward forces of about equal magnitude within the ice-class rules, it is hypothesized that rake will be balanced.

Computational Settings

Again a population of 30 propellers was analyzed within the computational framework for 65 generations. Propellers were iterated for the required thrust in the design point using steady computations, followed by unsteady computations and strength analysis. Both the radial and chordwise thickness and camber distributions are parameterized with Bézier curves. In addition, the radial distributions for pitch and chord were parameterized in design variables according to section 2.1.2 and included in the optimization.

Optimization Results

The progression of the optimization is presented in the Pareto-front overview of Figure 4-7. Contrary to the preceding results, here the trade-off between efficiency and thrust variation is clearly visible: high efficiency can only be obtained at the cost of high thrust variations which may cause noise, vibrations and erosive cavitation. Corresponding to Figure 4-7, the propeller distributions are shown in Figure 4-8. The colours and arrows indicate the direction for high efficiency. While the chordwise positions appear to have a clear trend, the pitch and chord distribution are not yet fully converged and are presented without further consideration. The following observations should however be made before proceeding with full optimization:

- Compared to the non-ice class reference propeller, it is noted that the efficiency of the optimized ice-class propellers is below the reference propeller. Thrust variation, however, is significantly[32] lower.
- The right plot within Figure 4-7 shows the blade profiles. Note the thick, heavy propellers to obtain low thrust variation. In addition, the chordwise thickness and camber distribution the middle position is preferred. This indicates a preference for thick elliptical profiles which are less sensitive to variations in the angle of attack while operating in the wake field yielding lower thrust variation.
- The higher efficiency propellers, visualized in red in the inner part of the right graph in Figure 4-7, are very slender and well shaped which gives confidence for the final optimization. While the position of chordwise maximum thickness moves towards the leading edge, the position of maximum camber prefers the trailing edge. Hence, hydrodynamic pressure will be distributed more evenly over the complete blade profile.
- Note that the thickness distribution of high efficient propellers resembles Figure 4-3. However, the fillet is more pronounced such that the maximum stress occurs further away from the hub. For full optimization, it is recommended to constrain fillet generation to allow other variations in the thickness distribution.
- It should be noted that the optimization controls the camber by the normalised camber over diameter where the camber at the tip was constant and equal to zero.

[32] Even though the numerical uncertainty for thrust variation is around 3%.

Likewise the thickness distribution, the design freedom is limited which rises the recommendation for allowing finite tip camber. The higher efficiency propellers prefer high camber in tip to obtain higher efficiency. For cavitation however, this should be avoided.

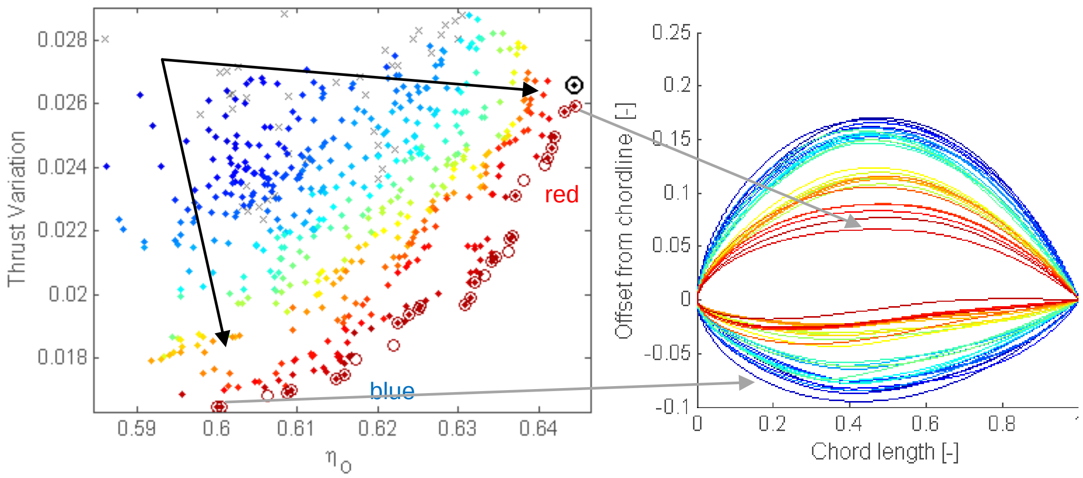

Figure 4-7: Optimization for efficiency and thrust variation by means of pitch, chord, thickness, camber and blade profiles. The reference propeller is indicated with the larger black circle. The arrows indicate the direction of the optimization progression. The right figure shows the shape of the blade profile at 0.7R over the Pareto front. The thick blue blades are propellers with high mass, low efficiency and low thrust variation. Red slender blades feature high efficiency at the cost of thrust variations.

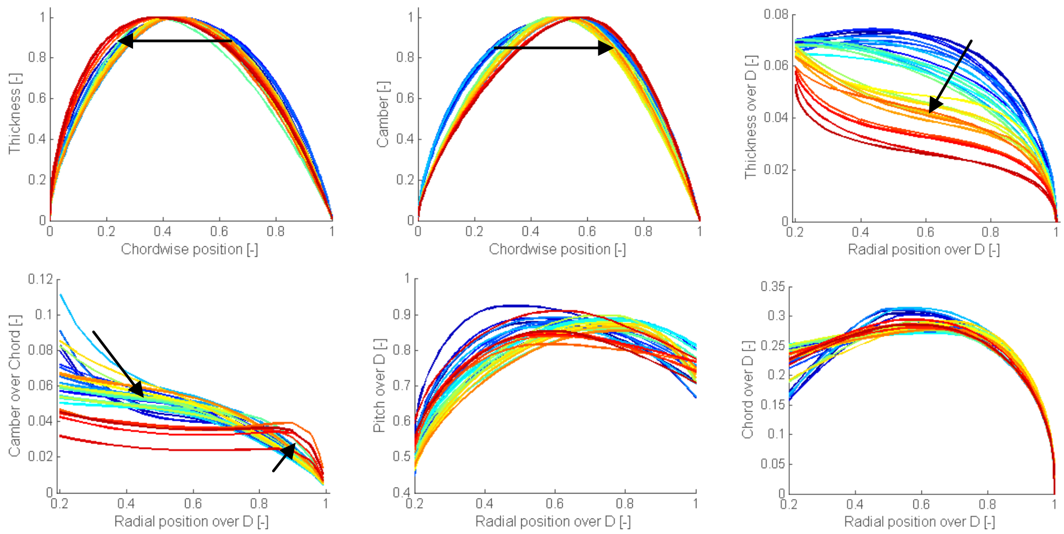

Figure 4-8: Overview of the propeller distributions of the propellers within the Pareto front. Red corresponds to high efficiency, while blue indicates low thrust variation. The arrows indicate the general direction for high efficiency. Arrows are omitted for the pitch and chord distribution, no clear trend is visible.

Convergence

If one would plot the convergence of efficiency and thrust variation it is observed that the optimization is not yet converged. Efficiency was improved by 0.4% in only two generations. Especially the radial pitch and camber distributions are not yet converged and could be improved further as observed from Figure 4-8. Note that Figure 4-7 and Figure 4-8 show three different families within the generation presented with the blade profiles in red for high efficiency, orange/yellow in between and green/blue for thick low thrust variation propellers. If optimized further, sharing of information will probably lead to the extinction of the thick heavy propeller family while efficiency is still being improved.

Also the material stresses give room for improvement as the most efficient propeller still has a margin of 36 [MPa] or 12% before the inequality of Equation (5) from the ice-class rules is violated. Additionally, the maximum stress is located at the hub near the fillet region where the ice-class criterion is conservative in the current strength analysis. In the tip region there still is a margin of about 20%. Furthermore, it can be observed that the stress constraint is not active for the low thrust variation propellers.

Design Check

A design check of the most efficient propeller has been performed before going to full optimization in order to assess whether the thrust variation objective steers the optimization towards non-cavitating propellers with well-defined pressure distributions such that the computational framework can be used for full optimization. First the hydrodynamic pressures will be presented after which the cavitation behavior will be discussed. An unsteady computation with cavitation serves as basis on a grid of 40x50 elements in radial and chordwise position.

Figure 4-9 shows a selection of pressure profiles for different circumferential positions and radial positions. Pressure is plotted non-dimensionally disregarding hydrostatic effects with the normalized pressure coefficient $-c_p$ such that suction side pressure is presented on top of the pressure side pressure. The area between the closed curves is an indication of the lift per surface area of the blade profile section. The angle θ denotes the position within the propeller plane in which $\theta = 0°$ denotes the top position.

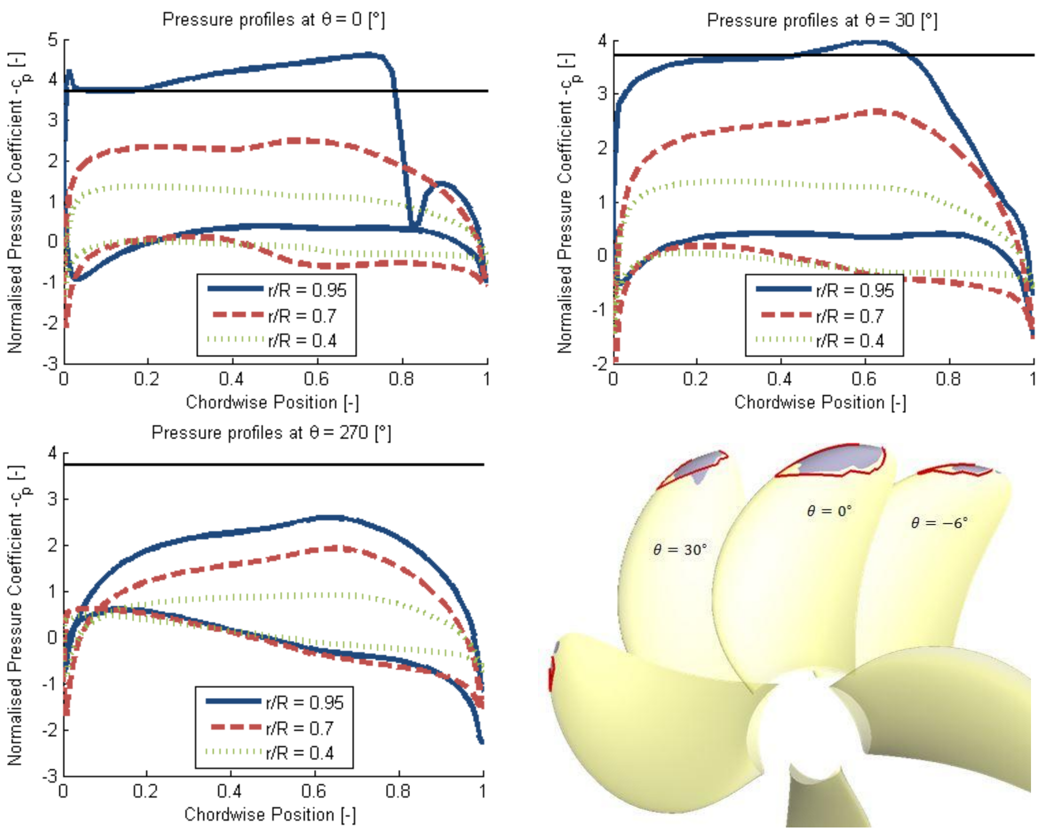

Figure 4-9: Pressure profiles over de blade profiles from leading edge to trailing edge. The black horizontal line corresponds to the cavitation inception pressure coefficient. In the bottom right, the cavitation extent (red line) and pressure below the cavitation inception pressure (shaded area) are sketched.

Concerning the pressure profiles it should be noted that the load is smeared out over the complete blade area. Sharp suction peaks are only present in the tip area. Note that for upwards motion ($\theta = 270°$) the leading edge produces negative thrust. The black horizontal line denotes the cavitation inception pressure which is exceeded for the tip region in the top half of the wake field. Although Figure 4-9 also presents a prediction of the sheet cavitation extent, the exceedance of the cavitation inception pressure in other locations indicates the risk of other cavitation appearances. The following is observed for cavitation:

- Between $\theta = -6°$ and $\theta = 0°$ the cavitation expands violently due to the flat pressure distribution in the tip region. As seen in the pressures for $\theta = 0°$ this leads to the collapse of pressure near the trailing edge. Cavitation will be unstable and may easily break up into patches which leave the trailing edge irregularly and erosive.
- The sheet cavitation does not leave the tip smoothly, but sticks to the blade surface. An erosive re-entrant jet might be formed there to close the sheet cavitation and reattach the flow.
- For the downward blade motion between $\theta = 0°$ and $\theta = 45°$ cavitation inception pressures are observed outside the prediction of the sheet cavitation. In reality, sheet cavitation could occur there too, but may be prone to separation and shedding yielding erosive cloud cavitating.

Concluding Remarks

A population of only 30 propellers is sufficient to find the Pareto front and seems to be usable for full optimization. Due to limited computational resources, optimization convergence has not been obtained. Either a larger population size or a larger number of generations should be chosen.

Although the best efficiency propeller shows possibly erosive cavitation, it provides a starting point for high efficiency ice-class propellers. The behavior of the tip cavitation can be further improved manually by correcting the radial camber distribution for instance.

Possibly, when taking a mass objective into account, the optimization will reject the thick propellers and tries to converge to low thrust variation without adapting the thickness distribution.

In addition to more sophisticated radial thickness and camber distribution, it would be a recommendation to improve the chordwise distributions as well. Besides increased robustness of the optimization algorithm, more design freedom in the feasible space is created. An overview of existing blade foil parameterization techniques is given in Salunke et al. (2014). Also a Bézier-based, second-order continuous description is addressed which can be implemented in the current computational framework.

4.1.4 High Skew Propellers (T-IV)

This optimization test case is intended to show that ice-class propellers may feature significant skew. The computation settings are similar as for previous test case T-III. In addition, the mass objective is taken into account while skew and rake distributions are varied as well.

The optimization progression is visualized in Figure 4-10. Thrust variation and mass are presented first on the left which produces a similar trade-off as was observed in Figure 4-7 of optimization case T-III. Thicker blade profiles yield lower thrust variation. In addition, due to highly skewed propeller geometry, the thrust variation is significantly lower compared to the results of T-III.

The best performing propellers in terms of mass and thrust variation are not the best in terms of efficiency which is the reason for the scattering of the optimization result in the right of Figure 4-10. Although the lowest mass propellers feature significant lower efficiency than the highest efficiency propeller, the optimization also converges to high efficiency, low thrust variation propellers as seen in the bottom right clustering of propeller in the right graph of Figure 4-10.

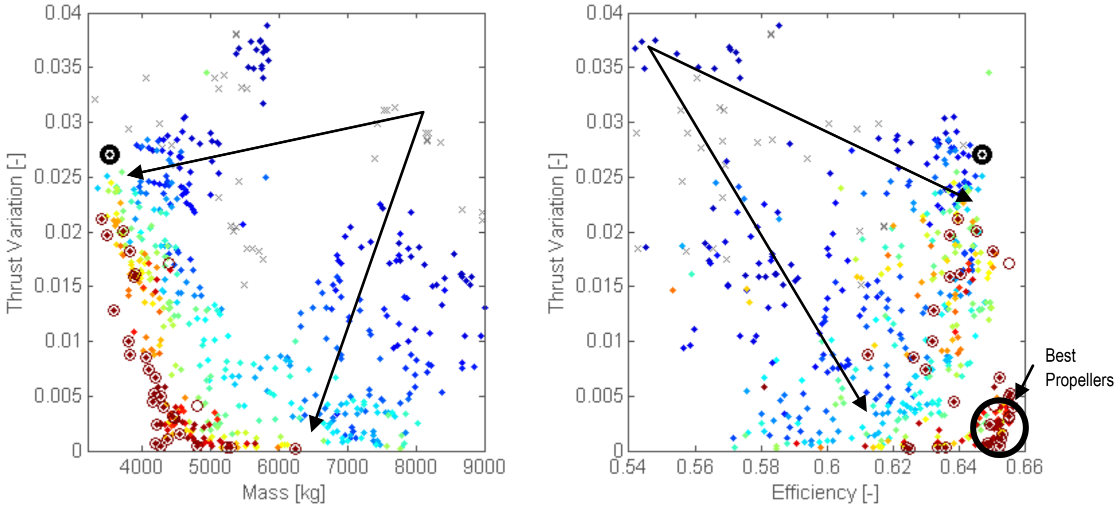

Figure 4-10: Optimization progression plots of full optimization case (F-II).The optimization result in the form of the last generation is encircled. The reference propeller is presented by the larger black encircled dot. The arrows indicate the direction of the optimization progression which is also represented by the colors from blue to red.

Propeller Geometry

Without going into details on all propellers, the average of the design parameters of the clustering of high efficiency, low thrust variation propellers is considered as the optimization result. It is indicated with the black circle in the left of Figure 4-10. The geometry distributions are presented below in Figure 4-11.

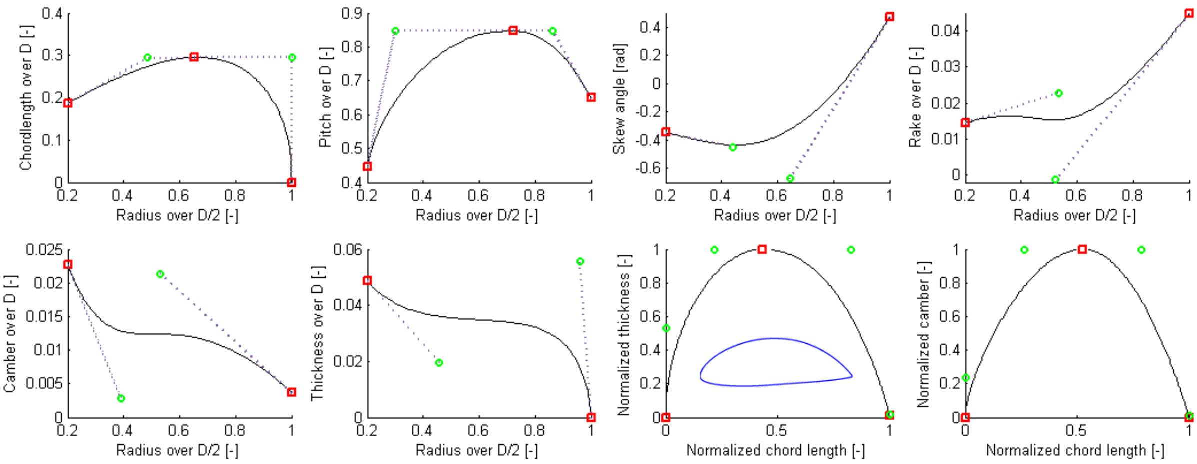

Figure 4-11: Overview of propeller distributions for the best propeller within optimization test case T-IV. The green circles represent the handle points of the Bézier curves, while the red squares are their control points. A sketch of the blade profile at 0.7R is given inside the chordwise thickness distribution.

Note the pitch reduction in the tip and the significant skew angle to obtain low thrust variation. Sectional profiles are laid down for high efficiency by moving the point of maximum thickness towards the leading edge while maximum camber is shifted towards the trailing edge as also observed in Figure 4-8 of test case T-III.

High Skew Ice-Class Propellers

From Figure 4-11 it becomes clear that the best propeller features a significant skew angle of more than 50 degrees. As explained in Huisman (2015), high skew propellers are prone to ice damages. The tip load cases were introduced for that reason, however, the optimization algorithm apparently manages to find highly skewed propellers which do satisfy the ice-class stress constraints. Note that the thickness in the tip region has significantly increased compared to optimization case T-III. Due to increased skew, more thickness is required in the tip region. The stress contours for each load case (LC) are given in Figure 4-12.

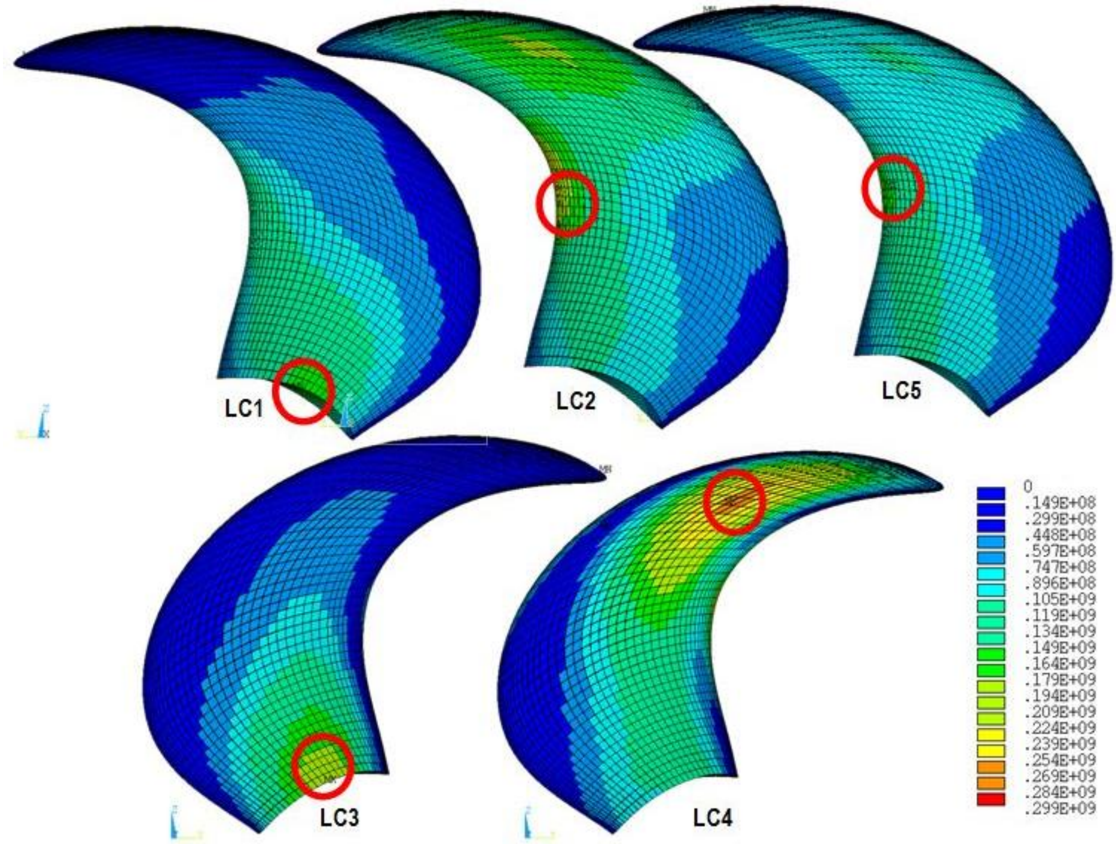

Figure 4-12: Stress contours for the high skew propeller in [Pa]. None of the ice-class load cases is critical. The most severe stress occurs for LC4 as 260 [MPa]. The red circles indicate the position of maximum stress.

The maximum stress occurs for load case four in the middle of the blade. Load case five, intended for backing operations, results in acceptable stresses. For high skew propellers, however, the tip will enter the ice first, prior to the trailing edge. As demonstration, referring to Table 2-3 and Figure 2-11, when adjusting the location of the load for load case five from 0.6R towards the tip at 0.8R the propeller does not satisfy the stress constraints as visualized below in Figure 4-13 and should be rejected as ice-class propeller. Damage cases by DNV (Norhamo et al., 2009) show that the location of the maximum stress on the suction side corresponds to the location where high skew ice-class propellers buckle in practice.

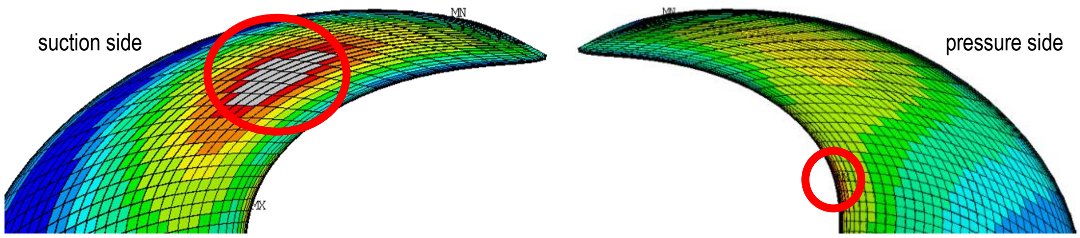

Figure 4-13: Stress levels for adjusted load case five. Maximum stress occurs in the tip region indicating that the propeller blade is prone to bend tips due to ice interaction. To the left the suction side is given and at the right the pressure side is visualized. The gray area and the red circles indicate exceedance of the maximum allowable stress. The color scale and units are similar to Figure 4-12.

Numerical Uncertainty

It should be noted that for the high skew propellers similar computation settings were used in the optimization as deduced in the numerical uncertainty studies in chapter 3. However, as recommended by Boorsma (2005) high skew propellers should feature higher tip spacing and more elements in radial direction. A similar study should be carried out for the best propeller within this optimization case to verify that these settings can be used with similar numerical uncertainty as found for the reference propeller. After performing this analysis it appears that numerical uncertainty is about twice as large, both for hydrodynamic and strength analysis. Attention towards numerical uncertainty within the optimization is required for further work.

Cavitation Behavior

Without repeating the more extensive design check of section 4.1.3 for optimization case T-III, the cavitation behavior of the optimized propeller of this optimization case is given in Figure 4-14. Cavitation detaches first at $-3°$ at the point of minimum pressure. Due to the thick blade profiles in the tip section the minimum pressure occurs at the point of maximum thickness from which the cavitation detaches.

Also the pressure profiles of the blade sections at different radial positions are presented at the right of Figure 4-14. Note that the pressure profiles are flat and comparable to those observed in optimization case T-III.

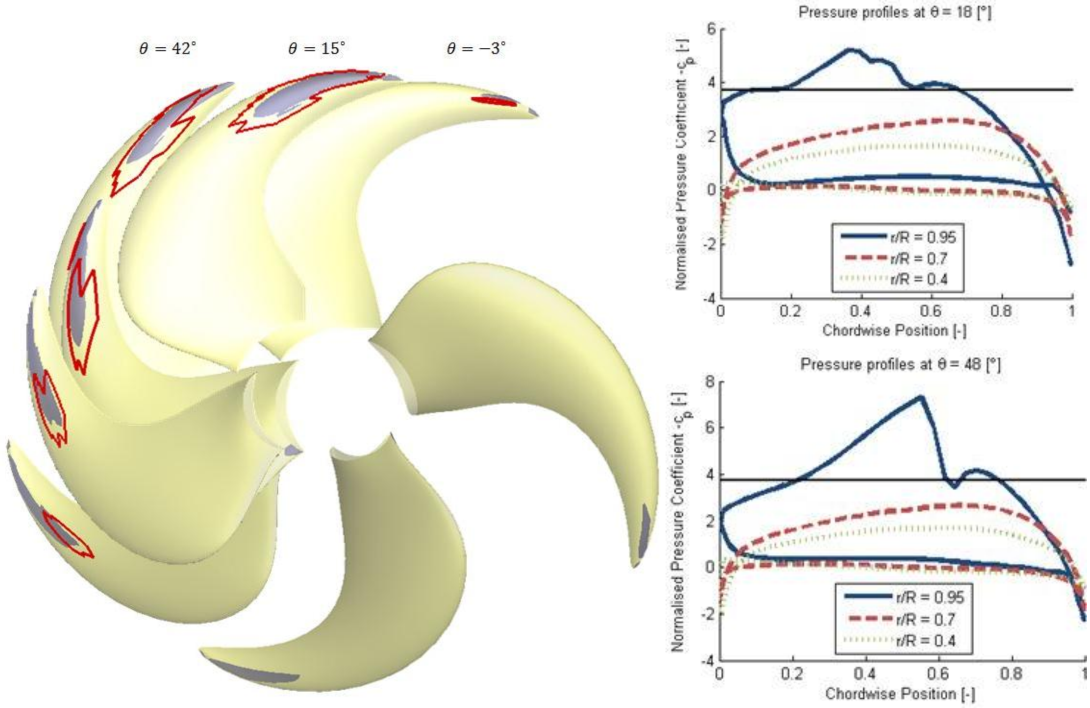

Figure 4-14: Cavitation behaviour of the optimized propeller. The cavitation extent (red line) and pressure below the cavitation inception pressure (shaded area) are sketched. To the right typical pressure profiles are shown.

Concluding Remarks

High skew ice-class propellers are generated by the optimization algorithm. The optimization algorithm automatically balances the blades due to the stress constraints from load case one and three at the hub. It can, however, be argued whether the ice class rules prescribe the correct load case for a backing operation. It is shown that, when adjusting the load case, the propeller does not satisfy the ice-class stress constraints.

Taking the mass objective into account does not necessarily lead to higher efficient propellers. Either due to the mass objective or the presence of skew[33], very thick blade profiles as observed in T-III are not present in the current test case. On the other hand, it can be seen that thick blade profiles are required in the tip to balance the strength derogation due to skew.

Compared to the reference propeller, an efficiency improvement of 1.43% is obtained, possibly due to the mass objective and additional design freedom in the radial camber distribution. Thrust variation can be reduced as much as 90%, mostly due to the skew distribution when comparing the results from test case T-III without skew.

[33] Having more influence on thrust variation than thicker blade profiles

4.2 Full Optimization

This section presents the results of the optimization computations with the full set of design variables. With the obtained results it can be shown that it is possible to reduce the ice-induced loading as function of propeller geometry. In this case it is also observed that ice-class propellers may feature significant skew as already seen in optimization test case T-IV.

Five objectives without any weight factors are chosen which yields that the algorithm tries to predict the trade-off for ten different objective combinations. Although ice-class stress constraints are satisfied, neither proper convergence towards high efficiency, low mass, low thrust variation nor low ice-induced loading can be observed as seen in the overview of Figure 4-15. The encircled propellers of the last generation are scattered, with only few high efficiency propellers. Nonetheless, the trade-offs between efficiency and thrust variation are already visible with the current population size. In general, the plots in Figure 4-15 that are supplied with an arrow show a clear optimization direction.

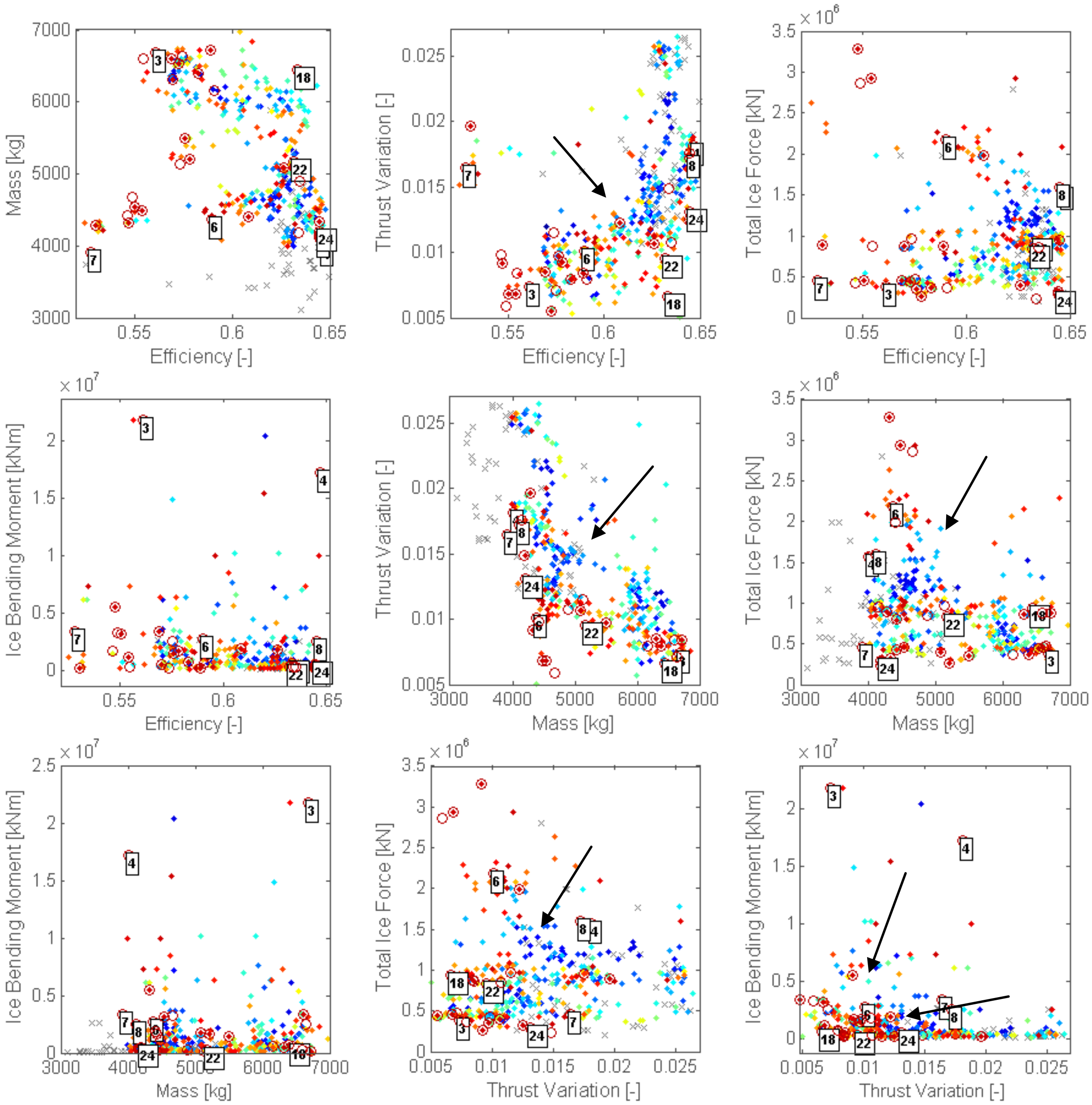

Figure 4-15: Overview of the optimization result when taking all objectives into account. The colors denote the generation number from blue to red while the last generation is encircled. Nine out of ten possible combinations are visualized. Propeller numbers are plotted to compare the position in the different trade-off plots.

Convergence

The convergence properties of the algorithm are visualized in Figure 4-16 by means of box plots. The arrows indicate the desired convergence direction. Note, however, that the extremes within the population follow this direction, but the main part of the population averages between all objectives. For thrust variation and mass this behavior is acceptable, even desirable, however, efficiency should be weighted in further work such that only high efficiency propellers will be allowed within the optimization. The current implementation considers each objective as equally important.

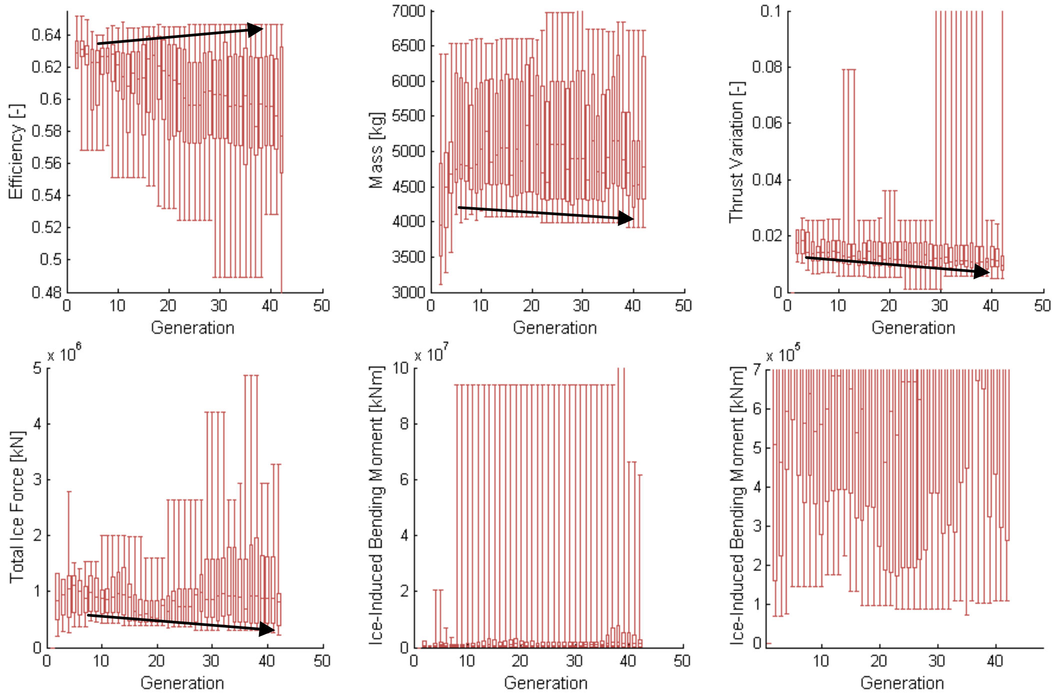

Figure 4-16: Visualization of convergence for the final optimization by means of box plots. The arrows give the desired convergence direction. The box plots give the extremes, first and third quartiles and the median of each generation. The bottom right plot gives a close up of the convergence of the ice-induced bending moment with similar scale on the y-axis as in the comparison with the ice class rules for the reference propeller in Figure 3-15.

Hypothetically, the observed convergence behavior might either be due to the small population size of only 32 propellers in relation to the 39 design variables and five objectives or the absence of a physical trade-off between each combination of objectives since this what the optimization algorithm is designed for.

The optimization was terminated after only 42 generations to retain computational power for other tasks. Possibly, when taking a larger population size in addition to proper weighting of the objectives, each trade-off can be predicted with a sufficient number of propellers while high efficiency would be obtained.

Overview of Propeller Geometries

The marked propellers are sketched for their general outline and blade profile at 0.7R in Figure 3-11. Both extreme designs which perform best for one trade-off and more moderate designs are presented. All propellers do satisfy the ice-class material stress constraints. Although the convergence is not yet reached, high skew propellers are already preferred.

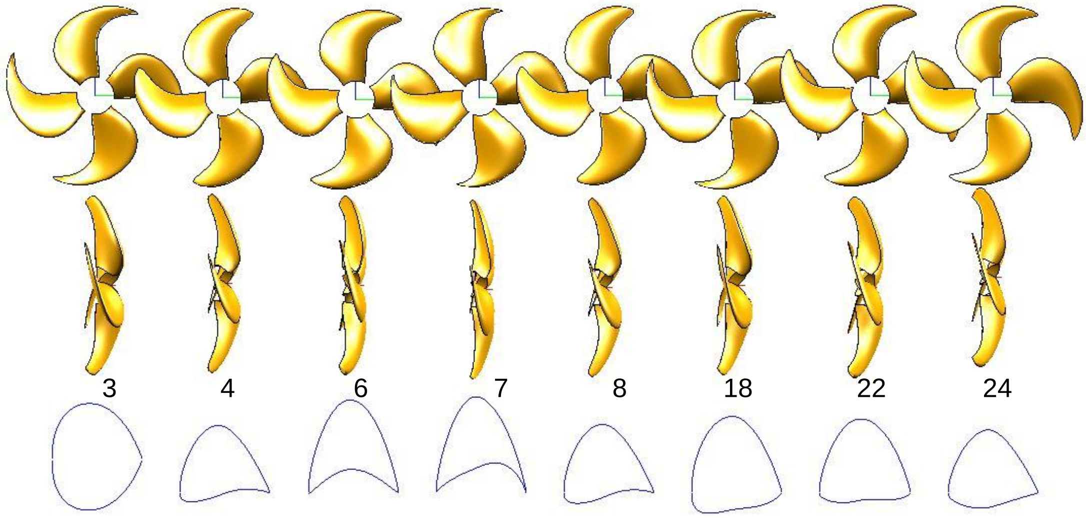

Figure 4-17: Sketches of general outline and blade profiles for optimized propellers.

If a best propeller has to be chosen for further design, propeller 24 should be considered. It features high efficiency, while mass and thrust variation are acceptable. Moreover, its ice-induced force and bending moment are significantly lower compared to the higher efficiency propellers four and eight. Due to its lower radial camber, the propeller features a slightly lower mean pitch which results in lower ice-induced loading. The distributions for propeller three, four, seven and 24 are visualized below in Figure 4-18.

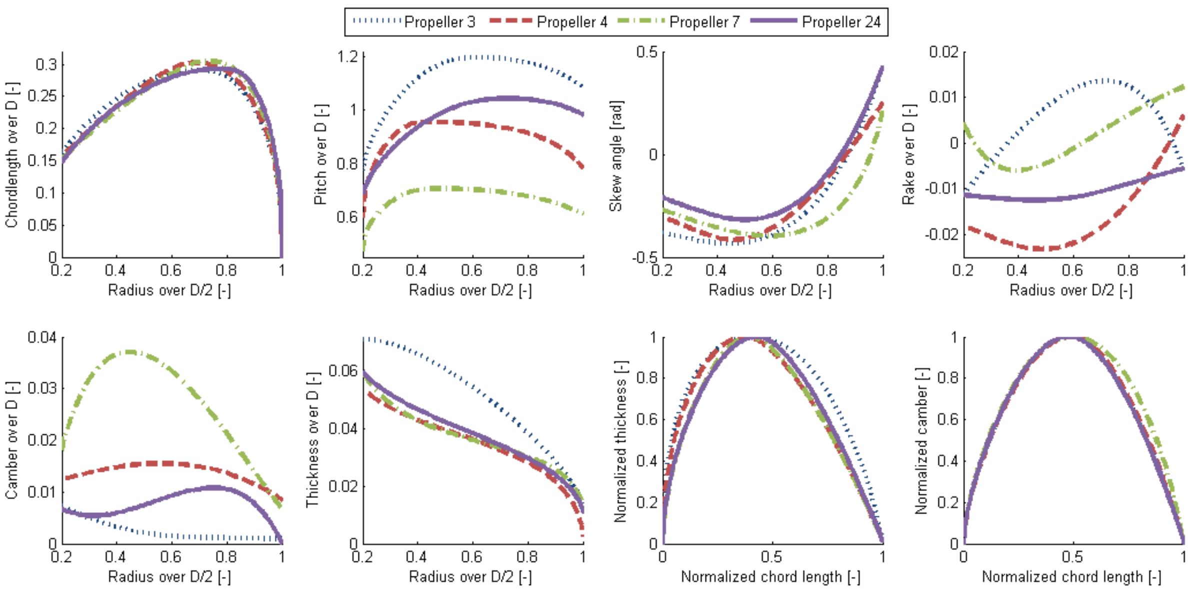

Figure 4-18: Overview of the propeller distributions for propeller three, four, seven and 24. These numbers correspond with Figure 4-15 and Figure 4-17.

Ranking

From the convergence properties and the geometrical overview of the propellers within the final generation it becomes clear that both extreme as moderate propellers are present within the optimization. The following examples show that propellers may stay within the population despite poor performance for multiple objectives:

- Propeller three, for instance, stays within the optimization due to its good performance in terms of the total ice force and thrust variation. Due to is large thickness and blunt leading edge, both the ice force and thrust variation are low. In terms of the other objectives, this propeller should be rejected. Poor lift generation properties due to low camber are the reason for high mean pitch which induces a large ice-induced bending moment.
- Also propeller four, with high efficiency and low mass stays within the optimization, despite its high ice induced bending moment. Propeller eight, equal on blade profile,

chord, pitch and skew features similar ice force. However, its bending moment is significantly lower due to lower thickness and higher camber. Apparently, the different direction of the force due to camber leads to a larger moment arm.

- Propeller seven is maintained too. It features low mass and low ice bending moment although its hydrodynamic performance is bad in terms of efficiency and thrust variation.

This shows both the strength and the weakness of the optimization algorithm. Its strength is to take best performing propellers for any combination of objectives into account, regardless of other combinations. In the optimization, their properties could merge into the best possible propeller. Its weakness is that no convergence towards optimum trade-off propeller is obtained when only searching for the extremes.

Concluding Remarks on Ice Loading

As observed from Figure 4-15, it is possible to reduce the ice induced loading according to Soininen idealized pressure distributions by means of geometry variation. However, no clear trade-off curves can be observed for either efficiency, mass or thrust variation. The following can be observed:

- Concerning propeller geometry, it is hypothesized that ice-induced loading is most sensitive to the camber and pitch distributions. Both individually and mutually due to the coupling by means of mean pitch iteration towards the design point.
- Furthermore, it is hypothesized that the skew distribution does also have significant influence on the ice-induced bending moment. The bottom right figure within Figure 4-16 shows that the average bending moment over J = 0.2 to 0.7 cannot be reduced more than presented in Figure 3-15 for the reference propeller. Or in other words, high skew propeller seem to feature higher ice-induced bending moments. In addition to the observations for T-IV in section 4.1.4, it indicates that further study in the applicability of the ice-class rules for high skew propellers should be performed.

A short sensitivity study by varying one variable at a time already produces encouraging results towards the confirmation of the above hypotheses. For future work, it is recommended to perform an in-depth sensitivity study to find the most sensitive design parameters.

5 CONCLUSIONS AND RECOMMENDATIONS

The main question was formulated as: *"How can propeller efficiency of ice-class cargo ships in operational conditions be improved by means of an automated propeller design optimization routine taking design constraints into account?"* It was hypothesized that an optimization procedure would give valuable design insight in the trade-off between efficiency, ice performance, ice strengthening and cavitation nuisance. Concerning this hypothesis, it can be remarked that a computational optimization framework is further developed and expanded. It appears that this framework is capable to find the trade-off curves between efficiency, thrust variation, mass and ice-induced loads for ice-class propellers.

Development of the Computational Optimization Framework

In this Master's thesis the Non-Dominated Sorting Genetic Algorithm II (NSGAII) is coupled to MARIN's in-house propeller geometry generator, hydrodynamic boundary element analysis method PROCAL and a finite element analysis to evaluate the propeller blade strength. Both the radial and chordwise propeller distributions are parameterized by means of Bézier curves into optimization design variables. Additionally, using Soininen's (1998) ice pressure distribution, the ice-induced loads during steady ice milling can be predicted. With these expansions, the computational framework is developed such that it should automatically satisfy the ice-class stress constraints while converging to the best possible objective values.

Main Conclusions

A case study has lead to the following main conclusions:

1. Ice-class material stress constraints can be automatically satisfied using the Non-Dominated Sorting Genetic Algorithm as optimization algorithm. The stresses due to the five load cases of the Finish Swedish Ice Class Rules should be evaluated using linear shell elements in a finite element method. Hence, the proposed computational framework seems suitable for ice-class propeller design.
2. The computational framework appears to be capable to optimize for hydrodynamic behavior and efficiency while satisfying the ice-class rules. Also high skew propellers seem to be allowed in the current version of the ice-class rules despite damage cases in practice. However, a small modification to the fifth load case results in a violation of the ice-class material stress constraints.
3. Chordwise thickness and camber distributions with four and three design variables respectively already provide encouraging optimization results. It appears that a thrust variation objective steers the optimization towards flat chordwise pressure profiles throughout the wake field. Cavitation computations are not yet included in the optimization, nonetheless, the optimized propellers show only little cavitation in the tip region.
4. Using Soininen's (1998) idealized pressure distribution for propeller ice milling, it appears that ice-induced loading can be reduced over a range of advance ratios, mainly as function of the blade profile, pitch and camber distribution although further research is deemed necessary on the geometric dependencies.

In conclusion, for this case study the optimization seems to provide a well-balanced starting point towards the design of high efficiency ice-class propellers. As such, the computational framework can be applied in practice.

Recommendations

Due to the assessment of the computational framework and its result, the following recommendations are proposed:

- **Applicability**. Within this Master's thesis constant diameter, rotational speed and blade area ratio were chosen for comparison reasons. It is possible to use the computational framework to study large diameter propellers in combination with ice-class. Furthermore, the structural analysis method based on linear shell elements can also be applied for hydrodynamic pressures using matching meshes such that non-ice class propellers can be optimized too.

- **Optimization**. For future work, it is recommended to optimize with a larger population size such that multiple-objective optimization becomes feasible. Additionally, it is recommended to include a weighting of the objectives within the ranking process of the genetic algorithm. The current computational framework considers each objective equally important, while efficiency will be the governing criterion in most cases. Lastly, although the current NSGAII optimization algorithm is capable to satisfy the ice-class rules, it is expected that the optimization can be improved using an algorithm which actively takes the constraint violations into account as discussed in the work of Vesting (2014). Currently, almost half of the propeller population is rejected for further consideration, while taking them into account could lead to faster convergence and shorter computational times.
- **Design Constraints.** The current computational framework assumes that the ice-class stress constraints are the only design constraints which have to be taken into account. Following the ice-class rules, it is assumed that hydrodynamic loads are included in the load cases. Possibly, including other class-rules, practical manufacturing constraints and hydrodynamic limiting load cases such as the crash-stop load case will lead to more realistic results. Additionally, taking cavitation constraints into account the optimization could generate propellers which require less human intervention for the final design stage.
- **Computational Methods.** Although best practice guidelines for moderately skewed propellers were given for both hydrodynamic and strength computations, it is recommended to verify and validate the computational tools further for high skew propellers. A decent numerical uncertainty study for the optimized propellers is not performed, but should be combined with validation studies for the final optimization results.
- **Ice Class Rules.** Since high skew propellers can be designed to satisfy the ice-class stress constraints, further study in the applicability and validity of the ice-class rules for high skew propellers should be performed. Either the adjustment of the location of the load or its magnitude should be reconsidered.
- **Sensitivity Study**. While this Master's thesis focuses on the optimization of ice-class propellers, another, maybe equally important approach would be a sensitivity study. When not only optimizing for efficiency, but also for thrust variation, mass, cavitation and ice-induced loading there becomes a need for knowledge on the most sensitive design parameters for each objective. Proper attention should be given to the cross-couplings between mutual design variables by several physical mechanism such as the mean pitch iteration.

REFERENCES

ANSYS Documentation. *Mechanical APDL Theory Reference.* Version 15.0.0. SAS IP, Inc. 2013.

Antes, H. (2010). *A Short Course on Boundary Element Methods.* Lecture notes. Institut für Angewandte Mechanik. Technische Universität Braunschweig. 30 November 2010.

ASME (2009). *Standard for Verification and Validation in Computational Fluid Dynamics and Heat Transfer.* ASME V&V 20-2009. 30 November 2009..

Auld, D.J. & Srinivas, K. (2015). *Aerodynamics for Students.* Web textbook. Available on: https://sites.google.com/site/aerodynamics4students/. Accessed 4 June 2015.

Boorsma, A. (2005). *PROCAL Generic Guidelines.* Cooperative research ship (CRS) report. Confidential. Lloyd's Register report CSG/TI/672412/6517. November 2005.

Bosschers, J., Vaz, G.N.V.B., Starke, A.R. & Wijngaarden, E. van. (2008). *Computational Analsyis of Propeller Sheet Cavitation and Propeller-ship interaction.* RINA Conference MARINE CFD2008. Southhampton.

Bosschers, J. (2009). *PROCAL v2.0 Theory Manual.* Cooperative research ship (CRS) report. Confidential. Marin report 20834-7-RD. July 2009.

Bosschers, J. & Peddle, A.G. (2014). *User's guide PROCAL baseline code version 2.218. Final report.* Cooperative research ship (CRS) report. Confidential. Marin report 26295-2C-RD. July 2014.

Carlton, J.S. (2007). *Marine Propellers and Propulsion.* Oxford: Butterworth-Heinemann. Second Edition.

Di Felice, F. (2001). *STREAMLINE. D21.1 – Results of model tests on reference configurations.* STREAMLINE-INS-DEL-D21.1-V02. INSEAN report. August 2011.

Deb, K. & Agrawal, R.B. (1995). *Simulated Binary Crossover for Continuous Search Space.* Complex Systems. Vol. 9, 1995, pp. 115-148.

Deb, K., Pratap, A., Agarwal, S. & Mayarivan, T. (2002). *A fast and Elitist Multiobjective Genetic Algorithm: NSGA-II.* IEEE Transactions on Evolutionary Computation. Vol. 6, No. 2, 2002, pp. 182 – 197.

Eça, L. & Hoekstra, M. (2014). *A procedure for the estimation of the numerical uncertainty of CFD calculations based on grid refinement studies.* Journal of Computational Physics. Elsevier. Vol. 262, 2014, pp. 104-130.

Eggers, J (2012). *Fluid Dynamics 3.* Lecture Notes. University of Bristol. School of Mathematics. Available on: http://www.maths.bris.ac.uk/~majge/fluids3 . Accessed 5 June 2015.

Fine, N.E. (1992). *Nonlinear analysis of cavitating propellers in nonuniform flow.* PhD dissertation. Department of Ocean Engineering. MIT.

Foeth, E.J. (2014). Propeller optimizations by means of the NSGA-II algorithm. Marin R&D report 70037-2-RD. December 2014.

Foeth, E.J. (2015). *Systematic propeller optimization using an unsteady Boundary Element Method.* Fourth International Symposium on Marine Propulsors (SMP'15). Austin, Texas, USA.

Holzapfel, G.A. (2000). *Nonlinear Solid Mechanics. A Continuum Approach for Engineering.* Reprint of April 2010. Chichester: Jon Wiley & Sons Ltd.

Huisman, T.J. (2015). *Optimization of ice-class propellers. Definition study.* Delft University of Technology and MARIN.

Katz, J. & Plotkin, A. (2001). *Low-Speed Aerodynamics.* Second Edition. 10th printing 2010. Cambridge: Cambridge University Press.

Kerwin, J., Kinnas, S., Lee, J. & Shih, W. (1987). *A Surface Panel Method for the Hydrodynamic Analysis of Ducted Propellers.* SNAME transactions. Vol. 95, 1987, pp. 93-122.

Kerwin, J.E. & Hadler, J.B.. Ed: Paulling, J.R. (2010). *The Principles of Naval Architecture Series. Propulsion.* New Jersey: The Society of Naval Architects and Marine Engineers.

Koning Gans, H.J. de (2012). *Introduction of Numerical Methods in Ship Hydromechanics.* Course notes MT523. Delft University of Technology. 19 November 2012.

Koskinen, P., Jussila, M. & Soininen, H. (1996). *Propeller ice load models.* Technical Research Centre of Finland (VTT). Research Notes, no. 1739.

Morino, L. (1993). *Boundary Integral Equations in Aerodynamics.* Applied Mechanics Review. Vol. 46, No. 8, 1993, pp. 445-466.

Nuland, H.W. (2014). *Automated multi-objective optimization of ship propellers, propeller design using a boundary element method searching the trade-off between efficiency and cavitation.* Master's Thesis. Delft University of Technology.

Norhamo, L., Bakken, G. M., Deinboll, O. & Iseskär, J.J. (2009). *Challenges related to propulsor – ice interaction in arctic waters.* First International Symposium on Marine Propulsors. SMP'09 , Trondheim.

Oosterveld, M.W.C. & Oossanen, P. van (1975). *Further computer-analyzed data of the Wageningen B-screw series*. International Shipbuilding Progress, Vol. 22, No. 251, July 1975.

Papalambros, P.Y. & Wilde, D.J. (2000). *Principles of optimal design. Modelling and Computation.* Cambridge: Cambridge University Press. Second Edition.

Peddle, A.G. (2013). *Development of a numerical model for propeller-ice interaction with inclusion in PROCAL environment.* Cooperative research ship (CRS) PRO-POLAR report. Confidential. Marin report 24417-2-POW. August 2013.

Ploeg, A. van der & Foeth, E.J. (2013). *Optimization of a chemical tanker and propeller with CFD.* Proceedings of the Fifth International Conference on Computational Methods in Marine Engineering. MARINE 2013.

Pouw, C.P. (2007). *Development of a Multiobjective Design Optimization Procedure for Marine Propellers.* Master's thesis. Delft University of Technology. 19 December 2007.

Salunke, N.P., Juned Ahamad, R.A. & Channiwala, S.A. (2014). *Airfoil Parametrization Techniques: A Review.* American Journal of Mechanical Engineering, Vol. 2, No. 4, 2014, pp. 99 – 102.

Sayas, F.J. (2008). *A gentle introduction to the Finite Element Method.* Course notes. University of Zaragoza.

Sederberg, T.W. (2014). *Computer Aided Geometric Design.* Course notes Brigham Young University. 9 October 2014.

Soininen, H. (1998). *A propeller-ice contact model.* PhD dissertation. 15 May 1998. Espoo: VTT publications.

Srinivas, N. & Deb, K. (1994). *Multiobjective Optimization Using Nondominated Sorting in Genetic Algorithms.* Journal of Evolutionary Computation. Vol. 2, No. 3, pp. 221-248.

Tennekes, H. & Lumley, J.L. (1972). *A first course in turbulence.* Third printing December 1974. Cambrige: The MIT Press.

Trafi (2010). *Maritime safety regulation - Ice class regulations and the application thereof.* Issued 23 November 2010 by the Finnish Transport Safety Agency. TRAFI/31298/03.04.01.00/2010.

Valtonen, V. (2015). *Finite element analysis as a tool to optimize propellers of ice going vessels.* Aker Arctic. Presentation. March, 2015. Available on: http://akerarctic.fi/sites/default/files/page/fields/field_attachments/10_valtonen.pdf. Accessed 29 September 2015.

Vaz, G.N.V.B. (2005). *Modelling of Sheet Cavitation on Hydrofoils and Marine Propellers using Boundary Element Methods.* PhD dissertation. Wageningen: MARIN.

Vaz, G.N.V.B. & Bosschers, J. (2006). *Modelling three dimensional sheet cavitation on marine propellers using a boundary element method.* Sixth International Symposium on Cavitation (CAV2006). Wageningen, September 2006.

Veitch, B. (1995). *Predictions of Ice Contact Forces on a Marine Screw Propeller During the Propeller-Ice Cutting Process.* PhD dissertation. Acta Polytechnica Scandinavica, Mechanical Engineering Series No. 118. Helsinki: Finnish Academy of Technology.

Vesting, F. & Bensow, R.E. (2014). *On surrogate methods in propeller optimisation.* Journal of Ocean Engineering, 15 September 2014. Vol. 88, pp 214-227.

White, F.M. (2011). *Fluid Mechanics.* Seventh Edition in SI Units. New York: McGraw-Hill.

Appendix A DESIGN PARAMETER BOUNDS

Geometry parameterization bounds for the Streamline case study were found iteratively as presented in Table A-1.

Table A-1: Overview of design parameters with their bounds and specific properties. The upper and lower values give the upper and lower bounds respectively. If only one number is provided, the parameter is fixed throughout the optimization.

Radial	$c_{hub}(y)$	$h_{hub}(x)$	$h_{hub}(y)$	$c_{tip}(x)$	$h_{tip}(x)$	$h_{tip}(y)$
Rake (over D)	-0.02 0.02	x_h+ 0.1 0.6	-0.05 0.1	-0.02 0.02	0.6 0.9	-0.05 0.05
Camber (over D)	0 0.03	x_h +0.2 0.5	0 0.06	0 0.01	0.5 0.8	0 0.03
Thickness (over D)	0.04 0.08	x_h 0.5	0.02 0.08	0.003 0.007	0.5 1	0.003 0.02
Skew (rad)	-0.4 -0.1	x_h+ 0.2 0.5	-0.8 0.4	0 0.45	0.5 0.9	-0.8 0
Radial	h_{hub}	c_{MAX}	h_{tip}	r_{hub}	r_{tip}	
Chord	0.2 0.6	0.35 0.8	1	0.2 0.6	1	
Pitch	0.2 0.6	0.4 0.8	0.5 0.9	0.3 0.7	0 0.5	
Chord-wise	$c_{LE}(y)$	$c_{LE}(x)$	$h_{max}(x)$	$c_{TE}(x)$		
Thickness [-]	0.3 0.8	0.15 0.4	0.2 0.6	0.1 0.4		
Camber [-]	0.2	0.4 0.6	0.4 0.6	0.6 0.8		

Wageningen, October 2015
MARITIME RESEARCH INSTITUTE NETHERLANDS